National Technical University
School of Applied Mathematical And Physical Sciences

PHYSICS DEPARTMENT
LABORATORY OF EXPERIMENTAL HIGH ENERGY PHYSICS

THE SEARCH FOR ANOMALOUS TRILINEAR GAUGE COUPLINGS IN THE $Z^0\gamma$ CHANNEL AT THE CMS/LHC EXPERIMENT

DOCTORAL THESIS

by

Eleni G. Petrakou

Advisor: Theodoros Alexopoulos
Professor

Athens, September 2011

ΕΘΝΙΚΟ ΜΕΤΣΟΒΙΟ ΠΟΛΥΤΕΧΝΕΙΟ
ΣΧΟΛΗ ΕΦΑΡΜΟΣΜΕΝΩΝ ΜΑΘΗΜΑΤΙΚΩΝ ΚΑΙ ΦΥΣΙΚΩΝ ΕΠΙΣΤΗΜΩΝ
ΤΟΜΕΑΣ ΦΥΣΙΚΗΣ
ΕΡΓΑΣΤΗΡΙΟ ΠΕΙΡΑΜΑΤΙΚΗΣ ΦΥΣΙΚΗΣ ΥΨΗΛΩΝ ΕΝΕΡΓΕΙΩΝ

ΑΝΑΖΗΤΗΣΗ ΓΙΑ ΤΙΣ ΑΝΩΜΑΛΕΣ ΤΡΙΓΡΑΜΜΙΚΕΣ ΣΥΖΕΥΞΕΙΣ ΒΑΘΜΙΔΑΣ ΣΤΟ ΚΑΝΑΛΙ $Z^0\gamma$ ΣΤΟ ΠΕΙΡΑΜΑ CMS/LHC

ΔΙΔΑΚΤΟΡΙΚΗ ΔΙΑΤΡΙΒΗ

της

Ελένης Γ. Πετράκου

Επιβλέπων: Θεόδωρος Αλεξόπουλος
Καθηγητής

Εγκρίθηκε από την τριμελή εξεταστική επιτροπή την 26η Σεπτεμβρίου 2011.

Θεόδωρος Αλεξόπουλος Καθηγητής	Γεώργιος Τσιπολίτης Αναπληρωτής Καθηγητής	Αριστοτέλης Κυριάκης Ερευνητής Γ′

Αθήνα, Σεπτέμβριος 2011.

Ελένη Γ. Πετράκου

Perieq’omena

Summary

This study deals with the search for anomalous trilinear couplings between gauge bosons at the elementary particles experiment CMS, in the final state consisting of a Z boson and a photon. Simulated datasets were used for the development of the methods, which was followed by the analysis of data from proton collisions at the LHC accelerator, and the specification of allowed values for the couplings.

A brief presentation of the experiment is followed by discussion about the characteristics of the signal from the new couplings, which occurs from a vertex involving two Z bosons and one photon. The characteristics of the backgrounds are discussed as well; the backgrounds consist of the same final state as the signal, coming from either Standard Model processes or misidentification. After this, the simulation process is presented along with the event generator developed for the specific analysis. The chain of the selection criteria for the physics objects under detection is eventually discussed, namely the selection of photons and electrons and muons, as the latter two occur from the Z boson's decay.

In order to deal with the background events which survive the selection, a technique was developed which permits the estimation of their number by using the measurement in the $Z\gamma$ channel and a dataset triggered by hadronic jets. The technique is discussed, and then the analysis results are presented as obtained with the first $36.1\,\mathrm{pb}^{-1}$ of proton collisions.

As the number of events is too low for a direct observation of any new couplings, a likelihood analysis is performed on the distribution of the photon transverse energy. Prediction functions are obtained by using the simulated datasets with anomalous couplings, and their compatibility with the measurement is examined. Finally, new limits are set on the possible values of the couplings through maximization of the likelihood.

The observation is compatible with the Standard Model. The limits on one of the two couplings are tighter than those from previous experiments, while more data are required for constraining the second one.

At the end of the academic year, the students asked me to give a talk about my experiences of teaching in Brazil. (.....)

Finally, I said that I couldn't see how anyone could be educated by this self-propagating system (...). "However," I said, "I must be wrong. There were two students in my class who did very well, and one of the physicists I know was educated entirely in Brazil. Thus, it must be possible for some people to work their way through the system, bad as it is." (...)

Then something happened which was totally unexpected for me. One of the students got up and said, "I'm one of the two students whom Mr. Feynman referred to at the end of his talk. I was not educated in Brazil; I was educated in Germany, and I've just come to Brazil this year."

The other student who had done well in class had a similar thing to say. And the professor I had mentioned got up and said, "I was educated here in Brazil during the war, when, fortunately, all of the professors had left the university, so I learned everything by reading alone. Therefore I was not really educated under the Brazilian system."

– *R. Feynman, "Surely you're joking Mr.Feynman"*

Preface

The unprecedented success of the Standard Model - the theoretical formulation of our knowledge about the elementary constituents of the world - has given rise to intensive attempts at finding a crack in its structure. One of the places scrutinized for such a hint by Nature lies within the very symmetries dictating the Model, in the form of relations between the mediators of forces: The presence of new couplings involving gauge fields would signify a deviation independent of any specific theoretical presumption, and was among the objects of the searches performed in the Compact Muon Solenoid experiment with the first data available from proton-proton collisions in the Large Hadron Collider at CERN.

The present study deals with this search for “anomalous” gauge couplings in events with the final state comprising of a Z^0 boson and a photon, and was performed on the data collected by the CMS experiment during 2010.

Chapter 1 provides an introduction to the Standard Model of elementary particles, and to the role of trilinear gauge couplings, along with phenomenological elements about the calculation of the possible contribution of new couplings.
Chapter 2 deals with the description of the LHC machine, and the CMS experiment and its subsystems. In conjunction with this, three studies concerning the detection of particles in the electromagnetic calorimeter and its preshower detector are discussed in Chapter 3.
The study for anomalous couplings is expanded on in Chapter 4. After a discussion of the characteristics of the expected new signal and the main background processes, and the tools used for their simulation, the experimental techniques employed for the identification of the involved particles and the elimination of background are examined. Subsequently, their application on the data from LHC collisions is presented. Finally, the analysis is concluded with the statistical treatment of the experimental measurement, and the obtained new limits on the presence of anomalous couplings.

Κεφάλαιο 1

Theoretical introduction

1.1 The Standard Model

1.1.1 Particle content

Particle Physics studies the elementary particles that constitute matter and describes the interactions between them. According to current knowledge we can distinguish two types of elementary particles which constitute matter: quarks and leptons, both with spin $1/2\hbar$ and arranged in three generations. The fundamental interactions discovered and studied in detail so far are four: the electromagnetic, the weak, the strong and the gravitational. However, the main concept of the quantum field theory is the unified description of both matter and interactions in terms of quantum fields, the former having semi-integer spin (fermions), the latter having integer spin (bosons).

Within the -extremely successful experimentally- description of the interactions of the fundamental components of matter known as Standard Model[1], the existence of the gauge bosons and the form of their interactions are dictated by local gauge invariance. In fact, gauge bosons are a manifestation of the Standard Model's symmetry group,

$$SU(3)_C \otimes SU(2)_L \otimes U(1)_Y$$

where :

- $SU(3)_C$ is the non-abelian gauge symmetry group which describes the strong interactions. Such a structure involves eight independent matrices, which are the generators of the group, reflecting the fact that the strong interaction is carried by eight vector bosons, the gluons. The gluons are massless, electrically neutral and carry the charge of strong interactions, known as "colour". The strong interactions are well-described by the theory of quantum chromodynamics (QCD).
- $SU(2)_L \otimes U(1)_Y$ is the weak isospin symmetry group which describes the

electromagnetic and weak interactions together (electroweak interaction)[2]. Three vector bosons, $W^{\pm}$, Z^0, are the mediators of the weak interactions, while the photon is exchanged in electromagnetic interactions. The weak bosons are massive particles, and can interact among themselves (more details are found in §1.2). $W^{\pm}$ have electrical charges of $Q = \pm 1$ respectively, while Z^0 is electrically neutral (charges are given in units of the elementary charge, e). The photon is massless, chargeless and does not interact with itself.

The main characteristics of strong, weak and electromagnetic interactions and their mediators are summarized in Table 1.1.

The fundamental constituents of matter, lacking known internal structure to date, are classified under two groups: quarks and leptons. Quarks are triplets under the $SU(3)_C$ group and hence undergo strong interactions; leptons are singlets under $SU(3)_C$. The left-handed states of all fermions are $SU(2)_L$ doublets, while their right-handed partners transform as $SU(2)_L$ singlets; placing right-handed and left-handed fermions into different multiplets of the $SU(2)_L$ group describes the parity violation.

The Standard Model includes three generations of fermions, which are identical except for the masses. Ordinary matter is composed of particles from the first generation. The other generations only appear briefly in high-energy processes (cosmic rays, accelerators).

The leptons are the electron (e^-), the muon (μ^-) and the tau (τ^-), each of which has electric charge $Q = -1$, and their corresponding neutrinos, ν_e, ν_μ, ν_τ, with $Q = 0$. The quarks are of six different flavours: u, d, c, s, t and b, and all have fractional charge $Q = \frac{2}{3}$, $-\frac{1}{3}$, $\frac{2}{3}$, $-\frac{1}{3}$, $\frac{2}{3}$ and $-\frac{1}{3}$ respectively. In nature quarks are found confined within the hadrons, a wider class of stable particles. The particle content of each generation is:

$$1^{st}\text{ generation: } \begin{pmatrix} \nu_e \\ e^- \end{pmatrix}_L,\ e^-_R,\ \begin{pmatrix} u \\ d \end{pmatrix}_L,\ u_R,\ d_R$$

$$2^{nd}\text{ generation: } \begin{pmatrix} \nu_\mu \\ \mu^- \end{pmatrix}_L,\ \mu^-_R,\ \begin{pmatrix} c \\ s \end{pmatrix}_L,\ c_R,\ s_R$$

$$3^{rd}\text{ generation: } \begin{pmatrix} \nu_\tau \\ \tau^- \end{pmatrix}_L,\ \tau^-_R,\ \begin{pmatrix} t \\ b \end{pmatrix}_L,\ t_R,\ b_R$$

along with the corresponding antiparticles. The left-handed (L) and right-handed (R) fields are defined by means of the chirality operator γ_5, *e.g.*:

$$e^-_L = \frac{1}{2}(1-\gamma_5)\, e^-; \quad e^-_R = \frac{1}{2}(1+\gamma_5)\, e^-$$

Although the original formulation of the Standard Model included massless neutrinos, there are now experimental indications of them being massive.

Interaction	Electromagnetic	Weak	Strong
Gauge bosons	γ	$W^{\pm}$, Z^0	gluons
Mass (GeV/c^2)	0	80.4, 91.2	0
Coupling strength	$\alpha \simeq \frac{1}{137}$	$G_F = 1.167 \times 10^{-5}\,\mathrm{GeV}^{-2}$	$\alpha_s \simeq 0.1$
Range (cm)	∞	10^{-16}	10^{-13}

P'inakas 1.1: *The characteristics of the three fundamental interactions described by the Standard Model, and their mediator fields.*

Quarks additionally carry the colour charge, q_α, $\alpha = 1, 2, 3$. There is mixing between the three generations of quarks, which is parametrised by the Cabibbo-Kobayashi-Maskawa (CKM) matrix. The origin of this mixing is still unexplained.

1.1.2 The electroweak theory

As discussed above, the bosons which serve as interaction mediators result from the gauge symmetry of $SU(3)_C \otimes SU(2)_L \otimes U(1)_Y$. Local gauge invariance makes the theory re-normalisable but also requires the gauge bosons to be massless. However, the fact that the weak gauge bosons are massive indicates that $SU(2)_L \otimes U(1)_Y$ is not a symmetry of the vacuum. In contrast, the masslessness of the photon reflects that electromagnetism, $U(1)_{em}$, is a good symmetry of the vacuum.

Thus, the Standard Model postulates the so-called Higgs mechanism[3], which spontaneously breaks the electroweak symmetry $SU(2)_L \otimes U(1)_Y$ to the electromagnetic symmetry $U(1)_{em}$ by introducing a complex scalar field: The Higgs field, $\Phi = \begin{pmatrix} \phi^+ \\ \phi^0 \end{pmatrix}$, is a doublet under $SU(2)_L$, with $U(1)_Y$ charge $y_\Phi = +1/2$. The Lagrangian of this field must be invariant under $SU(2)_L \otimes U(1)_Y$ local gauge transformations, and takes the form:

$$L_{Higgs} = (D_\mu \Phi)^\dagger (D^\mu \Phi) - V(\Phi) \tag{1.1}$$

where, in the most general case, the potential is:

$$V(\Phi) = -\mu^2 \Phi^\dagger \Phi + \frac{1}{2}\lambda(\Phi^\dagger \Phi)^2,$$

with $\lambda > 0$ and $\mu^2 > 0$ in order to have non-trivial minima, and the gauge covariant derivative is defined as:

$$D_\mu \Phi \equiv (\partial_\mu + ig\frac{\tau^i}{2} W^i_\mu + \frac{ig'}{2} B_\mu)\Phi \tag{1.2}$$

where τ^i are the Pauli matrices, and $g(g')$ are the $SU(2)_L$ ($U(1)_Y$) gauge coupling constants. W^i_μ, $i = 1, 2, 3$ are the $SU(2)_L$ gauge fields, and B_μ is the $U(1)_Y$ field associated with the weak hyper-charge $Y = Q - T_3$, where Q and T_3 are the electric charge operator and the third component of weak isospin, respectively. It should be noted that although the full form of the covariant derivative is presented here, its introduction is justified in the discussion that follows.

The minima of the potential $V(\Phi)$ lie on a circle of radius $\sqrt{\frac{\mu^2}{\lambda}}$, therefore the calculation of the Lagrangian for spontaneous symmetry breaking will involve perturbative expansion around this value. More specifically, if, out of the four degrees of freedom included in the Φ doublet, only one of the components of the neutral field is assumed to acquire non-zero vacuum energy value, *i.e.*

$$\phi_{1,2}^{+}, \phi_2^0 = 0, \quad \phi_1^0 = \sqrt{\frac{\mu^2}{\lambda}},$$

then four new fields are used to describe the fluctuations:

$$\eta \equiv \phi_1 - \sqrt{\frac{\mu^2}{\lambda}}, \quad \xi^i \equiv \phi_2^i, \ \ \xi = 1, 2, 3.$$

After the breaking of the symmetry and the perturbative expansion, a mass term emerges in the Lagrangian for the scalar field η, along with the massless ξ fields which clearly pose a problem to the model[4].

However, one additional element is the enforcement of invariance under local gauge transformation. This is done by introducing the following form, using a phase θ,

$$\Phi \longrightarrow e^{i\theta^i(x)}\,\Phi \tag{1.3}$$

along with the replacement of the derivatives in the Lagrangian with the covariant derivatives, defined in Equation (1.2). If Equation (1.3) is written in terms of its real and imaginary parts,

$$\Phi \longrightarrow (cos\theta^i + i\, sin\theta^i)(\Phi_1 + i\Phi_2^i),$$

then it can be seen that imposing a suitable choice of gauge for the phases,

$$\theta^i = -tan^{-1}\frac{\Phi_2^i}{\Phi_1},$$

is enough to eliminate Φ_2^i to zero.

The full form of the Lagrangian, after the spontaneous symmetry breaking and the enforcement of local gauge invariance, contains mass terms for the gauge fields entering the covariant derivative. It can be noted that these terms arose from interactions with the scalar fields and the subsequent acquisition of vacuum energy value (by ϕ_1^0). The disappearance of the massless fields ξ^i and the acquisition of mass from vector bosons occurred in the same move, by an - invariant - selection

of gauge. According to the common interpretation, the degrees of freedom corresponding to ξ^i were absorbed by the vector bosons in order for them to acquire longitudinal polarization and mass.
In brief, the electroweak bosons turn out to be constructed from combinations of the W^i_μ, B_μ fields,

$$Z_\mu = \cos\theta_w W^3_\mu - \sin\theta_w B_\mu, \qquad W^+_\mu = \frac{1}{\sqrt{2}}(W^1_\mu - iW^2_\mu$$

$$A_\mu = \sin\theta_w W^3_\mu + \cos\theta_w B_\mu, \qquad W^-_\mu = \frac{1}{\sqrt{2}}(W^1_\mu + iW^2_\mu$$

where the mixing phase θ_w is the so-called "Weinberg angle". At the same time, the minimum value of the Higgs field is invariant under $U(1)_{em}$ transformations, which means that this symmetry is unbroken and the photon stays massless.

The degree of freedom which survives from the original scalar doublet after the symmetry breaking corresponds to a new scalar particle, the Higgs boson, which must be massive and electrically neutral. However, its mass, which is acquired through self-coupling in the potential $V(\Phi)$, is arbitrary in the theory and the Higgs boson has not been observed in experiments so far.
The Higgs boson mass at tree-level is:

$$m_H^2 = 2\lambda \upsilon^2$$

where $\upsilon \equiv \sqrt{\frac{\mu^2}{\lambda}}$ is the vacuum expectation value and is related to the boson masses and their gauge couplings to fermions (g, g') in the following way:

$$m_{W^\pm} = \frac{1}{2} g\upsilon, \;\; m_Z = \frac{1}{2}\upsilon\sqrt{g^2 + g'^2}$$

The strength of the self-interaction of the Higgs boson, λ, can in turn be expressed in terms of the Higgs and gauge boson masses and the gauge coupling as:

$$\lambda = \frac{1}{8} g^2 \frac{m_H^2}{m_{W^\pm}^2}$$

and is completely arbitrary within the Standard Model, therefore the Higgs boson mass is unknown.

The mechanism of symmetry breaking is also used to provide mass to the fermions, making them couple to the Higgs boson with different strength (Yukawa couplings) according to their mass. The value of each coupling constant, G_f, is directly related to the corresponding fermion mass, m_f:

$$m_f = G_f \frac{\upsilon}{\sqrt{2}}$$

The values of the Yukawa couplings are arbitrary as well within the Standard Model, and they are determined from the experimental measurements of the fermion masses.

The full lagrangian of the electroweak theory has the form:

$$\mathcal{L}_{SU(2)\times U(1)} = \mathcal{L}_{gauge} + \mathcal{L}_{\Phi} + \mathcal{L}_{f} + \mathcal{L}_{Yukawa}$$

- The gauge part is:

  $$\mathcal{L}_{gauge} = \frac{1}{4} W^i_{\mu\nu} W^{\mu\nu i} - \frac{1}{4} B_{\mu\nu} B^{\mu\nu}$$

  with field strength tensors

  $$B_{\mu\nu} = \partial_\mu B_\nu - \partial_\nu B_\mu,$$

  $$W^i_{\mu\nu} = \partial_\mu W^i_\nu - \partial_\nu W^i_\mu - g^{(\prime)} \epsilon_{ijk} W^j_\mu W^k_\nu,$$

  where ϵ_{ijk} is the totally antisymmetric tensor, and W^i_μ, $i = 1, 2, 3$ and B_μ are the $SU(2)_L$ and $U(1)_Y$ gauge fields.

- $\mathcal{L}_{\Phi}$ is the scalar, or Higgs, part of the lagrangian, which was examined above (Equation (1.1)).

- $\mathcal{L}_f$ and $\mathcal{L}_{Yukawa}$ describe, respectively, the couplings of the free leptons and the Yukawa couplings, acting between the Higgs doublet and the various flavours of quarks and leptons. These couplings make possible the quark and lepton mass terms generation in the Standard Model.

In total, the simplest version of the Standard Model contains 19 free parameters: 5 couplings (g_s, g, g', μ^2, λ), 9 masses (6 for the quarks and 3 for the leptons, with the assumption that neutrinos are massless), the 4 independent phases in the CKM matrix which describes the quark flavour mixing, and 1 phase which accounts for QCD interaction among gluons which can violate the CP symmetry.

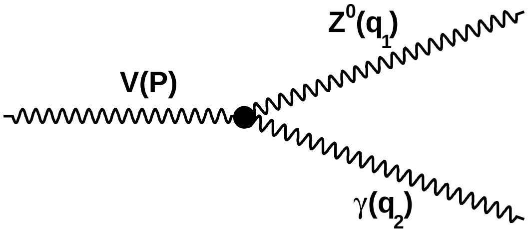

Sq'hma 1.1: *Effective vertex involving photons and* Z^0 *bosons* ($V = Z^0, \gamma$ *virtual).*

1.2 Trilinear gauge couplings

1.2.1 Trilinear gauge couplings in the Standard Model

As stated in §1.1.2, the gauge boson part of the electroweak Lagrangian is

$$\mathcal{L}_{gauge} = \frac{1}{4} W^i_{\mu\nu} W^{\mu\nu i} - \frac{1}{4} B_{\mu\nu} B^{\mu\nu}$$

where $W^i_{\mu\nu}$ and $B_{\mu\nu}$ are the field strength tensors of the $SU(2)_L$ and $U(1)_Y$ gauge fields, W^i_μ, $i = 1$, 2, 3, and B_μ respectively.
After the symmetry breaking, the electroweak bosons are built from combinations of the W^i_μ, B_μ fields,

$$Z_\mu = cos\theta_w W^3_\mu - sin\theta_w B_\mu, \qquad W^+_\mu = W^1_\mu$$

$$A_\mu = sin\theta_w W^3_\mu + cos\theta_w B_\mu, \qquad W^-_\mu = W^2_\mu$$

resulting in trilinear interactions which can only involve both charged and neutral gauge bosons.
The absence of trilinear vertices with all neutral gauge bosons reflects the fact that (i) no self-interactions can enter the $B_{\mu\nu}$ term since the $U(1)_Y$ group is abelian, (ii) the B_μ field cannot enter the $W_{\mu\nu}$ term, since the two respective groups are factorized by construction, and consequently the relevant structure constant is zero.

1.2.2 Effective treatment of trilinear gauge couplings

Within the Standard Model, the relation between the symmetry structure and the allowed trilinear gauge vertices is absolute. However, there is no known law which *in principle* prohibits additional trilinear vertices, and their existence could

be a legitimate deviation from the Standard Model predictions. The method for treating this possibility is to use a parametrisation independent of any particular theoretical model, by means of an effective Lagrangian[5].
In the following, only the trilinear interactions involving exclusively neutral gauge bosons will be examined.

The effective Lagrangian is built by including all possible interaction terms with three vector bosons, and imposing only the most general restrictions[5]: Lorentz invariance of the on-shell photon, electromagnetic gauge invariance, and assumption of negligible fermion masses. Eventually, the function of the vertex involving photons and Z^0 bosons, $Z^0\gamma V$ ($V = Z^0, \gamma$ virtual), shown in Figure 1.1 can be parametrised using four free parameters in each of the two cases, named $h^V_{1,2,3,4}$ ($V = Z^0$, γ):

for momenta $Z^0(q_1)\gamma(q_2)V(P)$,

$$\Gamma^{\alpha\beta\mu}_{Z\gamma V}(q_1, q_2, P) = \mathcal{A}^V \cdot \Big[h_1^V (q_2^\mu g^{\alpha\beta} - q_2^\alpha g^{\mu\beta}) + \frac{h_2^V}{m_Z^2} P^\alpha [(P \cdot q_2) g^{\mu\beta} - q_2^\mu P^\beta] \tag{1.4}$$

$$+ h_3^V \epsilon^{\mu\alpha\beta\rho} q_{2\rho} + \frac{h_4^V}{m_z^2} P^\alpha \epsilon^{\mu\beta\rho\sigma} P_\rho q_{2\sigma} \Big], \tag{1.5}$$

where $\epsilon^{\mu\alpha\beta\rho}$ is the totally antisymmetric tensor, m_Z is the Z^0 boson mass, and the overall factor $\mathcal{A}^V$ becomes

$$\mathcal{A}^Z = \frac{P^2 - q_1^2}{m_Z^2} \text{ for } V = Z^0, \text{ and } \mathcal{A}^\gamma = \frac{P^2}{m_Z^2} \text{ for } V = \gamma.$$

The eight couplings h_i^V are dimensionless functions of the squared momenta. The couplings $h_{1,3}^V$ consist of operators of dimension 6, while $h_{2,4}^V$ receive contributions from operators of dimension ≥ 8 [5]. The couplings h_1^V and h_2^V are CP-violating, while h_3^V and h_4^V are CP-conserving. The couplings have no physical meaning *per se*, but they are related to the electric and magnetic dipole and quadrupole moments of the $V - Z^0$ transition, as a result of the involved invariance principles on the Lagrangian[6]:

$$d_Z = -\frac{e}{m_Z} \frac{1}{\sqrt{2}} \frac{k^2}{m_Z^2} (h_3^V - h_4^V) \qquad \text{Electric dipole transition moment}$$

$$Q_Z^e = \frac{e}{m_z^2} \sqrt{10} \, (2h_1^V) \qquad \text{Electric quadrupole transition moment}$$

$$\mu_Z = -\frac{e}{m_Z} \frac{1}{\sqrt{2}} \frac{k^2}{m_Z^2} (h_1^V - h_2^V) \qquad \text{Magnetic dipole transition moment}$$

$$Q_Z^\mu = \frac{e}{m_z^2} \sqrt{10} \, (2h_3^V) \qquad \text{Magnetic quadrupole transition moment.}$$

Within the Standard Model all couplings h_i^V vanish at leading order, but at one-loop level the CP-conserving $h_{3,4}^V$ are non-zero, due to triangular diagrams with internal fermion loops. These one-loop contributions are calculated to be negligible[7].
It should be stressed that, in the vertex function (Equation (1.4)), the denominator of the overall factor and of the terms proportional to $h_{2,4}^V$ should formally contain the characteristic energy scale at which the new interactions are expected to occur. The choice of the Z^0 boson mass, m_Z, is arbitrary and does not cause any loss of generality; for a different mass scale, M, all subsequent results can be obtained by scaling $h_{1,3}^V$ ($h_{2,4}^V$) by a factor M^2/m_Z^2 (M^4/m_Z^4).
Finally, possible sources of the new couplings could include the existence of excited Z^* bosons which would decay into a Z^0 and a photon, or internal structure of the Z^0, *e.g.* a fermion-antifermion bound state. As an example, in the second case the characteristic scale of new physics, Λ, could be related to the size Λ^{-1} of such bound states.

1.2.3 Parameterisation of the trilinear gauge couplings

A crucial consideration when studying the anomalous trilinear gauge couplings ("aTGCs") is partial-wave unitarity. Since the h_i^V couplings depend on the particle momenta, the preservation of unitarity at high centre-of-mass energies must be ensured, and appropriate dependence on the energy has to be included in their description. A way to achieve this is by using form factors for the couplings, making sure they fall off rapidly for large momenta and asymptotically vanish at high energies, essentially restricting the couplings to their Standard Model values. The common choice for the form factors has been the dipole form factors[8]:

$$h_i^V(p^Z, p^\gamma, \hat{s}) = \frac{h_{i0}^V}{\left(1 + \frac{\hat{s}}{\Lambda^2}\right)^n}, \tag{1.6}$$

where Λ is the cutoff scale, *i.e.* the energy at which the novel interactions may start to appear. The subscript 0 denotes the low energy approximation of the couplings. Unitarity bounds of the involved quantities were first derived for the helicity amplitudes, and then "translated" to the couplings[9]. The assumption that only one aTGC is non-zero at a time leads to the following bounds when $\Lambda >> m_Z$:

$$|h_{10}^Z|, |h_{30}^Z| < \frac{(\frac{2}{3}n)^n}{(\frac{2}{3}n - 1)^{n-3/2}} \frac{0.126\, TeV^3}{\Lambda^3},$$

$$|h_{20}^Z|, |h_{40}^Z| < \frac{(\frac{2}{5}n)^n}{(\frac{2}{5}n - 1)^{n-5/2}} \frac{2.1 \times 10^{-3}\, TeV^5}{\Lambda^5},$$

$$|h_{10}^\gamma|, |h_{30}^\gamma| < \frac{(\frac{2}{3}n)^n}{(\frac{2}{3}n - 1)^{n-3/2}} \frac{0.151\, TeV^3}{\Lambda^3},$$

$$|h_{20}^{\gamma}|, |h_{40}^{\gamma}| < \frac{(\frac{2}{5}n)^n}{(\frac{2}{5}n-1)^{n-5/2}} \frac{2.5 \times 10^{-3}\, TeV^5}{\Lambda^5}.$$

The exponent n is arbitrary and model-dependent, and has to be provided along with Λ. However, it must be $n > 3/2$ for $h_{1,3}^V$ and $n > 5/2$ for $h_{2,4}^V$ to preserve the unitarity. In the case that more than one of the couplings are non-zero, the bounds may be weaker due to cancellations.

However, the reasons behind the use of this or any other parametrisation of the couplings are purely calculational, in the sense that unitarity will not be violated in the actual experimental measurement. One qualitative way to understand the issue is the following[10][11]: Unitarity can only be violated for an energy $\sqrt{s'}$ around or larger than Λ. But if there is some excess at $\sqrt{s'}$ which could be attributed to new physics, setting a conservative limit is not desirable. On the other hand, if no excess is observed, then there is no violation of unitarity.[1] In addition, the assumption about the specific form of the parametrisation is not founded, and actually results in a loss of the predictions' generality.

Another issue which may arise is bias due to the choice of the Λ value[11][12]. Smaller values of Λ result in the form factor suppressing the number of events with high p_T, therefore in less enhanced cross-sections. In the case that aTGCs exist, this means that a choice of, *e.g.,* smaller Λ than the one in nature will lead to an overestimation of the couplings. If aTGCs do not exist, then the use of smaller Λs will result in a loss in sensitivity during limit setting. (To a lesser degree, these bounds also depend on the power n in the form factor.)

In an electron collider there would not be any need for this technique, since the energy of each event would be precisely known. For hadron colliders though, the ideal alternative to using form factors would be to perform the search as a function of $\hat{s}$, without any assumption on the couplings' behaviour; this method would avoid

---

[1] A more quantitative argument involves the factorization of the effective Lagrangian into terms dependent on Λ: If there is physics beyond the Standard Model, then the Lagrangian at low energies can be expressed as a sum of Lagrangians[6],

$$\mathcal{L}(\sqrt{s} << \Lambda) = \mathcal{L}_{SM} + \sum_{n=5}^{\infty} \sum_{j} \frac{f_{nj}}{\Lambda^{n-4}} O_{nj}$$

(where f are couplings and O operators,)
meaning that corrections to the Standard Model are suppressed by powers of $\frac{\sqrt{s}}{\Lambda}$.
In this light, if signal excess is observed at $\sqrt{s} << \Lambda$, then no higher order terms need to be considered, and the coupling does not depend on $\sqrt{s}$.
If, on the other hand, signal excess is observed at $\sqrt{s} > \Lambda$, then the higher order terms have a big impact. However, nothing is known about these terms' behaviour, and the assumption that they all have a dependence on a factor $F(\frac{s}{\Lambda^2})$, which in addition follows a very specific form, is a long shot.

any bias that the choice of form factors and of the Λ value has on the maximal discovery potential[11]. With the collection of enough LHC data, a meaningful analysis as a function of $\hat{s}$ would become possible.

Finally, although another reason for using the dipole form factors would be the direct comparison of the limits with previous experiments, in this case it would have been meaningless: So far the maximum energy scale of possible new physics was set to 2 TeV by previous experiments, a value which is surpassed in LHC.

Taking all the above into consideration, the choice of not using form factor parametrisation was made for the present analysis. In practice, this translates to setting the exponents n to zero, for all h_i^V, in the event generator software (§4.2, §4.6.1).

1.3 Calculation of the $Z^0\gamma$ production

The matrix element calculation of the $Z^0\gamma$ production has been performed using the helicity amplitudes summation method[12][13]. The cross-sections and dynamical distributions have also been evaluated; the calculations employed a combination of analytic and "Monte Carlo" integration techniques.
The algorithm for the "matrix element generation" has been incorporated in a software package by U.Baur, *et al,* and was eventually employed for the production of the simulated datasets used in the present analysis. A detailed discussion of the relevant software is found in §4.2. Here, the terms contributing to the calculations and their phenomenological treatment are presented in brief.

The terms contributing to the $Z^0\gamma$ production up to the next-to-leading-logarithm (NLL) order have been included in the calculations, both for the Standard Model (§1.1) and for new trilinear vertices (§1.2.2). This refers to $2 \to 2$ and $2 \to 3$ body processes of leading order (LO), bremsstrahlung emission at leading-logarithm order (LL), gluon emission, and the next-to-leading order (NLO) terms of one-loop gluon corrections[14].

1.3.1 Two-body contributions

The Feynman diagrams contributing to the subprocess $q_1\bar{q}_2 \to V\gamma$, ($V = Z^0, \gamma$), are shown in Figure 1.2 (LO, with the photon emitted off one of the interacting quarks in the case of Standard Model, and from the new interaction vertex in the case of aTGCs), and Figure 1.3 (NLO, virtual correction from one-loop gluon processes).
The two-body part of the production cross-section has the following general form, consisting of three terms:

$$\sigma_{(2b)}^{NLL} = \sum_{q_1,q_2} \int \mathrm{d}\upsilon \mathrm{d}x_1 \mathrm{d}x_2 \times \left[G_{q_1/p}(x_1, M^2) G_{\bar{q}_2/p}(x_2, M^2) \frac{\mathrm{d}\hat{\sigma}^{NLL}}{\mathrm{d}\upsilon} + (x_1 \leftrightarrow x_2) \right] + \sigma_{brem}^{NLL} + \sigma^{HC}$$

In more detail:

- The sum in the first term runs over all contributing quark flavours, q_1, q_2, while the integration is performed over all the relevant phase-space; υ is a dimensionless variable used instead of the centre-of-mass scattering angle θ^*, $\upsilon \equiv \frac{1}{2}(1 + \cos\theta^*)$. The cross-section at parton level, $\mathrm{d}\hat{\sigma}^{NLL}$, is convoluted with the parton density functions $G_{q/p}$. (A caret will denote cross-sections at parton level.) It consists of the following parts:

$$\frac{\mathrm{d}\hat{\sigma}^{NLL}}{\mathrm{d}\upsilon} = \frac{\mathrm{d}\hat{\sigma}^{LO}}{\mathrm{d}\upsilon} + \frac{\mathrm{d}\hat{\sigma}^{virt.}}{\mathrm{d}\upsilon} + \frac{\mathrm{d}\hat{\sigma}^{soft}}{\mathrm{d}\upsilon} - \frac{\mathrm{d}\hat{\sigma}^{SC}}{\mathrm{d}\upsilon}, \qquad (1.7)$$

where $\mathrm{d}\hat{\sigma}^{LO}$ is the contribution from the LO diagrams (Figure 1.2) and $\mathrm{d}\hat{\sigma}^{virt.}$ is from the gluon one-loop corrections (Figure 1.3). The last two

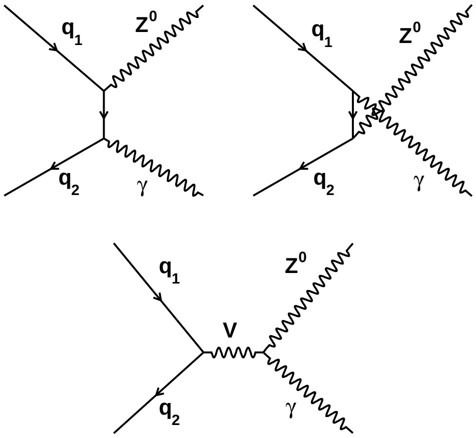

Sq'hma 1.2: *Leading order diagrams for the* Z^0, γ *production. The two diagrams in the first row are the only ones permitted within the Standard Model. The diagram in the second row, with* $V = Z^0$ *or* γ*, can occur if anomalous trilinear vertices exist.*

terms originate from corrections for singularities in the soft region of phase-space; the contribution of $\mathrm{d}\hat{\sigma}^{soft}$ is discussed in §1.3.3, while $\mathrm{d}\hat{\sigma}^{SC}$ is a correction term fixing the integration limits in the collinear region.

- The term σ^{NLL}_{brem} deals with photon bremsstrahlung up to NLL order. At NLL order, there are collinear singularities associated with final-state bremsstrahlung which are appropriately absorbed into the fragmentation function; the term σ^{NLL}_{brem} is the "remnant" after this process.

- σ^{HC} is the term dealing with singularities in the collinear region of phase-space (§1.3.3), which are absorbed into the initial-state parton density functions.

1.3.2 Three-body contributions

The three-body contributions to the calculation of the $Z^0\gamma$ production for the subprocesses $q_1 g \to V\gamma q_2$ and $\bar{q}_2 g \to V\gamma\bar{q}_1$ originate from the diagrams in Figure 1.4, which are of leading-logarithm (LL) order, with a photon emitted off the final-state quark. For the subprocess $q_1\bar{q}_2 \to V\gamma g$ the contributions come from the diagrams in Figure 1.5 which involve soft gluon emission.
The relevant cross-sections at parton-level are convoluted with the parton density functions. They are then integrated numerically over the three-body phase-space, except for subprocesses which are found to fall in the soft or collinear regions of

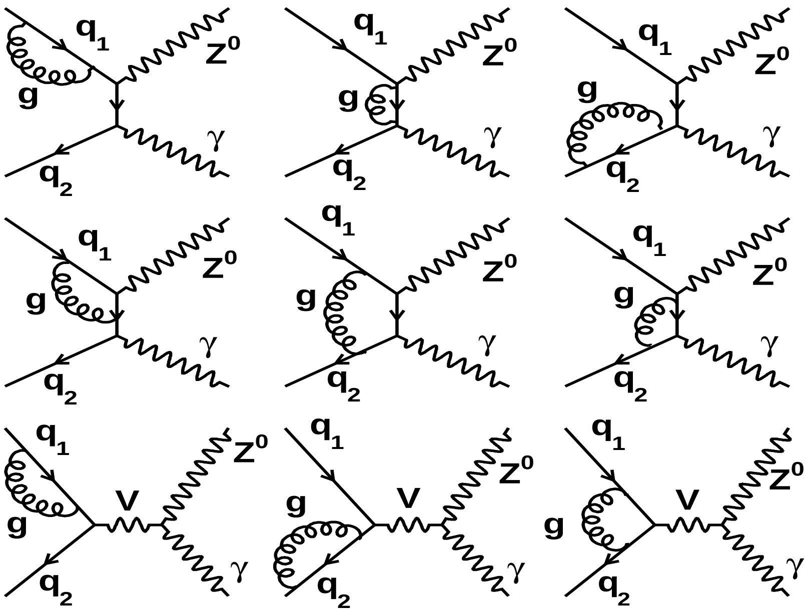

Sq'hma 1.3: *Next-to-leading order diagrams for the* Z^0, γ *production with one-loop gluon corrections. The diagrams in the first and second row are permitted within the Standard Model, along with the corresponding u-channel diagrams. The diagrams in the third row, with* $V = Z^0$ *or* γ*, can occur if anomalous trilinear vertices exist.*

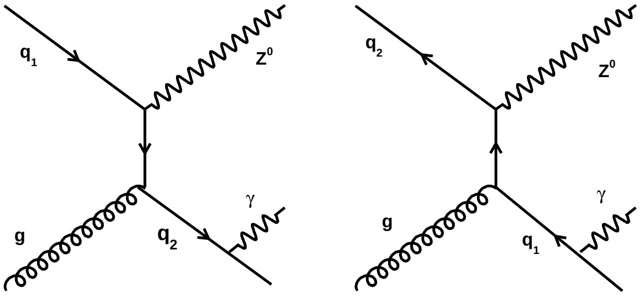

Sq'hma 1.4: *Leading-logarithm order diagrams for the* Z^0, γ *production; these are processes permitted within the Standard Model.*

the phase-space (§1.3.3). Finally, a sum is performed over all partons contributing to the initial and final state of the three subprocesses.

1.3.3 Phase-space singularities

As mentioned in §1.3.1, corrections for collinear and soft singularities in the three-body phase-space have to be taken into account in the calculation of the $Z^0\gamma$ processes. The idea behind the method for dealing with the singularities is to partition the phase space into soft, collinear, and finite regions, by introducing (and tuning) cutoff parameters; and then by comparing the values of the kinematic invariants s, t (for collinear regions) or the gluon energy (for soft regions) with the values of the cutoff parameters.
The integration over the singular regions results in finite two-body contributions, which appear in the cross-sections in §1.3.1, plus singular pieces. Subsequently, dimensional regularization exposes the poles. In the case of the collinear singularities, the poles are factorised and absorbed into the parton distribution functions or the photon fragmentation functions; in the case of the soft singularities, they cancel with the virtual infrared ones (terms $\frac{\mathrm{d}\hat{\sigma}^{virt.}}{\mathrm{d}v}$ and $\frac{\mathrm{d}\hat{\sigma}^{soft}}{\mathrm{d}v}$ in Equation (1.7)). Both kinds of remaining finite contributions depend on the choice of values for the cutoff parameters, but when they are added any dependence on the cutoff parameters is cancelled.

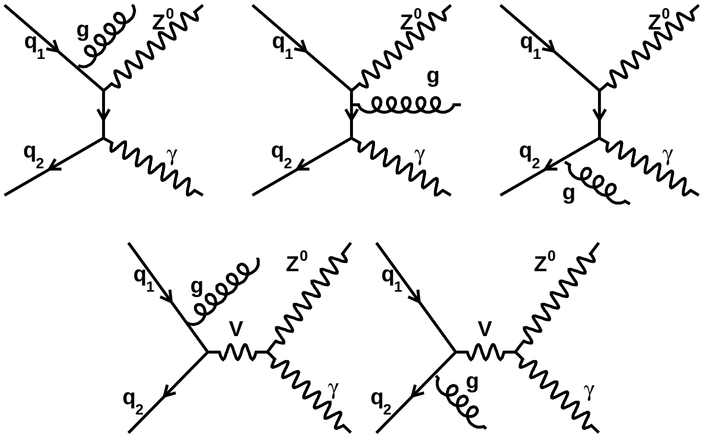

Sq’hma 1.5: *Soft gluon emission processes accompanying the* Z^0, γ *production. The diagrams in the first row are permitted within the Standard Model, along with the corresponding* u*-channel diagrams. The diagrams in the second row, with* $V = Z^0$ *or* γ*, can occur if anomalous trilinear vertices exist.*

Κεφάλαιο 2

The Compact Muon Solenoid experiment

This Chapter describes the Large Hadron Collider (LHC) and the Compact Muon Solenoid (CMS) experiment at CERN and its subsystems, with some emphasis on the electromagnetic calorimeter as the analyses presented in Chapter 3 deal with it more extensively.
LHC is described in §2.1. In §2.2, the CMS experiment is overviewed and each detector is covered in some detail. §2.3 deals with the description of the electromagnetic calorimeter and its design, as motivated by the physics requirements. The reconstruction of muons is also briefly discussed in §2.2.7.

2.1 The LHC machine

The Large Hadron Collider[15] is a proton-proton collider installed in the 26.6 km circumference tunnel formerly used by the LEP electron-positron collider at CERN, at a depth ranging from 50 to 175 m underground. The design collision energy, projected to be reached after 2012, is $\sqrt{s} = 14\,\mathrm{TeV}$ and the design luminosity is $L = 10^{34}\,\mathrm{cm}^{-2}\,\mathrm{s}^{-1}$. The luminosity is the number of collisions per unit-time and cross-sectional area of the beams, and depends only on the collider parameters; the LHC design specifications will provide ~ 1 billion proton-proton interactions per second. For a beam with Gaussian kinematic distribution, the luminosity is given by:

$$L = \frac{f\, n_b\, N_p^2\, \gamma}{4\,\pi\, \epsilon_n\, \beta^*}\, F,$$

where f is the revolution frequency, n_b is the number of bunches in the beam, with N_p protons in each bunch, γ is the relativistic (Lorentz) factor, ϵ_n is the

Energy per nucleon	7 TeV
Dipole field at 7 TeV	8.33 T
Luminosity (L)	$10^{34}\,\mathrm{cm}^{-2}\mathrm{s}^{-1}$
Bunch separation	25 ns
Number of bunches (n_b)	2808
Protons per bunch (N_p)	1.15×10^{11}
Betatron value (β^*)	0.55 m
Beam radius RMS (σ)	$16.7\,\mu$m
Luminosity lifetime	15 hr
Collisions per crossing	~ 20

P'inakas 2.1: *Design values of the LHC machine parameters for proton-proton collisions.*

normalized transverse emittance of the beam[1], β^* is the betatron function[1], and F is the geometric reduction factor, due to the crossing angle of the beams. The values of the LHC machine parameters can be found in Table 2.1.

Usually, the integrated luminosity $\mathcal{L} = \int L\mathrm{d}t$ is used to express the amount of available collision data.

The LHC is composed of a set of two synchrotron rings along which two independent proton beams circulate in opposite directions, and uses the whole pre-accelerator complex that already existed at CERN as an injector. The beams intersect at four points around which experiments are placed: Two of these are high luminosity regions and house the "general purpose" ATLAS[16] and CMS[17] detectors, located in opposite positions along the ring. The other two detectors, placed at the beam insertion points from the Super Proton Synchrotron (SPS), are devoted to specific research topics: LHC-b[18] is optimized to study b-quark physics and CP-symmetry violation in particular, and ALICE[19] is used for the study of heavy ion collisions.

In autumn 2009, the first collisions at the LHC were delivered at centre-of-mass energies of 900 GeV and 2.136 TeV. Since March 2010, the LHC has been operating at 7 TeV. The operation during 2010 proceeded smoothly, with a gradual increase of the instantaneous luminosity up to $L = 2 \times 10^{32}\,\mathrm{cm}^{-2}\,\mathrm{s}^{-1}$ in October 2010. LHC operated with proton beams until the beginning of November 2010, when the heavy ion fill started. The proton-proton integrated luminosity delivered by LHC in 2010 was almost equal to $50\,\mathrm{pb}^{-1}$.

---

[1] The emittance ϵ_n is defined as the product of the RMS of the beam particles' position distribution, σ, with the RMS of their momenta distribution, σ'. The betatron function, β^*, is defined as the ratio σ/σ' at the interaction point. While ϵ_n is constant for all the beam lifetime, β^* can be reduced by focusing the beams using magnetic optics at the interaction points.

2.2 The CMS subsystems

The Compact Muon Solenoid (CMS) is a "general purpose" particle detector, using collisions from the Large Hadron Collider (LHC). Its design began in the early 90's, followed by the developmental phase and the construction of its subsystems. Its assembly and commissioning spanned the last decade up to the start of LHC operations in November 2009.

In order to meet its physics goals, the detector requirements for CMS were summarised as follows[17]:

- Good muon identification and momentum resolution over a wide range of momenta in the region $|\eta| < 2.5$, good dimuon mass resolution ($\sim 1\%$ at $100\,\mathrm{GeV/c^2}$), and the ability to determine unambiguously the charge of muons with $p < 1\,\mathrm{TeV/c}$.

- Good charged particle momentum resolution and reconstruction efficiency in the inner tracker. Efficient triggering and offline tagging of τ and b-jets, requiring pixel detectors close to the interaction region.

- Good electromagnetic energy resolution, good diphoton and dielectron mass resolution ($\sim 1\%$ at $100\,\mathrm{GeV/c^2}$), wide geometric coverage ($|\eta| < 2.5$), measurement of the direction of photons and/or correct localization of the primary interaction vertex, rejection and efficient photon and lepton isolation at high luminosities.

- Good missing E_T and dijet mass resolution, requiring hadron calorimeters with a large hermetic geometric coverage ($|\eta| < 5$) and with fine lateral segmentation ($\Delta\eta \times \Delta\phi < 0.1 \times 0.1$).

As seen in Figure 2.1, the CMS includes a silicon-based inner tracker and a crystal electromagnetic calorimeter preceded by a preshower detector at its endcaps, all surrounded by a hadronic calorimeter. These systems are placed inside a superconductor solenoid which produces a nominal magnetic field of 4 T to curve the charged particle paths. Outside the magnet there are muon chambers embedded in the magnet yoke which returns the magnetic flux into the detector. In the forward regions of CMS there are two identical hadron calorimeters, covering part of the space left uncovered by the rest of the calorimetry. Each subsystem is discussed in some detail in the following sections.

The CMS has a cylindrical shape, with the beam pipe set along the central axis of the cylinder and the collision of the two beams taking place at the centre of the cylinder. The coordinate system is right-handed, with the origin centred at the nominal collision point, the y-axis pointing vertically upward, the x-axis pointing radially inward towards the centre of the LHC and the z-axis pointing along the beam direction. The azimuthal angle, ϕ, is measured from the x-axis in the $x - y$ plane, and the polar angle, θ, is measured from the z-axis. The pseudorapidity is

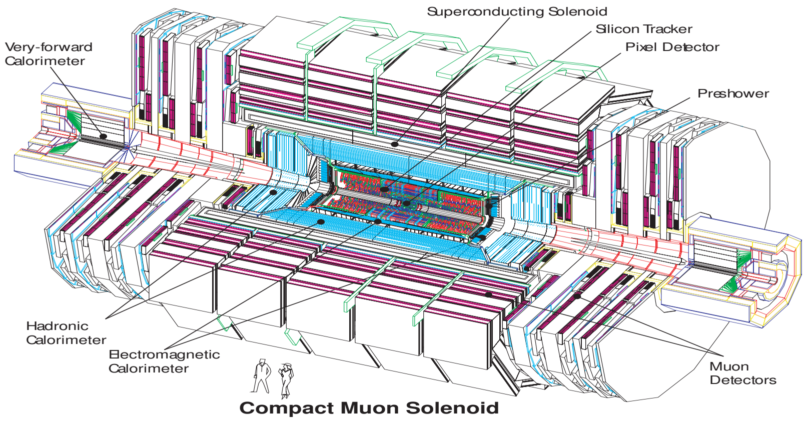

Sq'hma 2.1: *Layout of the CMS experiment and its subsystems.*

normally used instead of the θ angle and is defined as $\eta = -\ln\left(\tan\frac{\theta}{2}\right)$. Thus, the momentum and energy measured transverse to the beam direction, denoted by p_T and E_T, respectively, are computed from the x and y components.

2.2.1 Superconducting magnet

The bore of the superconducting magnet[21] of the CMS experiment has an inner diameter of 6 m and a length of 12.5 m, and encompasses the tracker and the calorimeters. The flux is returned through a 10,000 t yoke comprising five wheels and two endcaps, composed of three disks each. Cooled with liquid helium, it is designed to generate an axial and uniform magnetic field with nominal value of 4 T in the central region of the detector, causing the charged particle tracks to bend and separate, as well as stay confined. The stored energy at full current is 2.6 GJ, and for the NbTi cold mass of 220 t (*i.e.* the superconducting coil and its support) the ratio of stored energy over the cold mass is distinctively high (11.6 kJ/kg).
Due to its large size in combination with the value of the magnetic field, the CMS magnet does not operate at its nominal field so far but at 3.8 T, in order to protect against possible quenching.

2.2.2 Trigger system

In order to control the amount of stored data at CMS, the Trigger and Data Acquisition System[22] was developed to ensure that the prompt data is stored while other non-prompt events are rejected quickly without overloading the electronic circuits and devices.
The trigger chain is divided into the “Level-1” (“L1”) and the “High Level Trigger” (“HLT”). At the nominal LHC luminosity, one begins with a rate $\mathcal{O}(10^7)$ Hz

of collisions. The L1 trigger consists of custom-designed, largely programmable electronics, and reduces the rate to $\mathcal{O}(10^5)$ Hz. The HLT is a software system implemented in a filter farm of about one thousand commercial processors, and finally reduces the rate down to the order of 100 Hz, which matches the storage capability.

The L1 Trigger uses coarsely segmented data from the calorimeters and the muon system, while holding the high-resolution data in pipe-lined memories in the front-end electronics. The HLT has access to the complete read-out data and can therefore perform complex calculations similar to those made by the off-line analysis software, if this is required for events with special interest. It is also divided into internal "steps", named L-2, L-2.5 and L-3.

The selection process used in the trigger chain is described in some more detail for the case of muons in §2.2.7, and electrons in §3.1.

2.2.3 Inner tracking system

The inner tracking system[23] of the CMS (Figure 2.2) is designed for a precise and efficient measurement of the trajectories of charged particles emerging from the LHC collisions, and of the secondary vertices. Along with the electromagnetic calorimeter and the muon system the tracker has to identify electrons, muons, and tau leptons. In addition, tracking information is heavily used in the HLT system to reduce the recorded event rate.

The tracking system surrounds the interaction point and has a length of 5.8 m and a diameter of 2.5 m. The solenoid magnet provides a homogeneous magnetic field of 3.8 T over the full volume of the tracker.

At the LHC design luminosity, about 1000 particles from more than 20 overlapping proton-proton interactions for each bunch crossing, *i.e.* every 25 ns, are expected to traverse the tracker. In order to identify reliably the charged particles' trajectories and the respective bunch crossings, a detector with high granularity and fast response is essential. However, these requirements imply a high power density of the on-detector electronics, which in turn requires efficient cooling and results in an increase of the amount of material in the tracker, leading to undesirable interaction effects (multiple scattering, bremsstrahlung, photon conversion, nuclear interactions); the final decision was a compromise between these two aspects. Another issue, actually the main challenge in the design of the tracker, was developing components able to operate in the intense radiation environment for about ten years.

All these requirements lead to a tracker design entirely based on silicon sensor technology. In addition, given the hit rate density from collisions, in order to keep the occupancy $\leq 1\%$, pixel detectors have to be used at radii below 10 cm. At intermediate and higher radii however, micro-strip silicon detectors can be used. In the outer region ($55 - 110$ cm) the strip width is increased in order to limit the number of read-out channels (an increase in the length would result in an increase

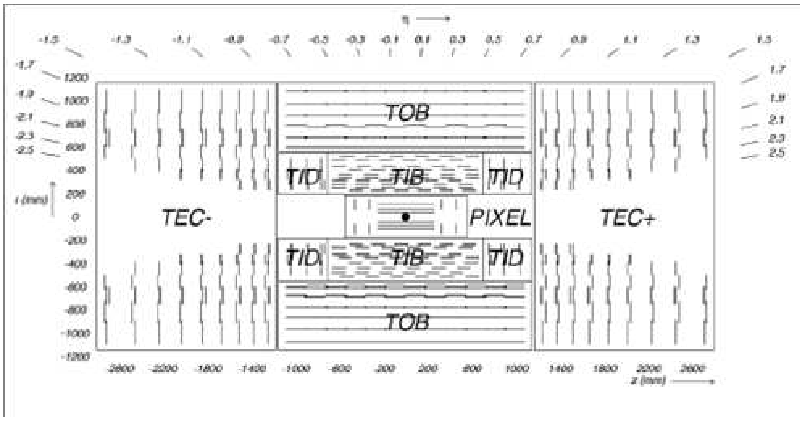

Sq'hma 2.2: *Schematic cross-section of the tracker detector.*

in the capacitance, and therefore electronics noise).
The pixel detector has three barrel layers at radii of 4.4, 7.3 and 10.2 cm, and the silicon strip tracker has ten barrel detection layers extending outwards to a radius of 1.1 m. Their endcap regions consist of two disks in the pixel detector and twelve disks in the strip tracker, on each side, extending the acceptance of the tracker up to a pseudorapidity of $|\eta| < 2.5$. With a total active silicon area of about $200\,\mathrm{m}^2$, the CMS tracker is the largest silicon tracker ever built.

The pixel detector

The pixel detector measures points in $(r-\phi, z)$, and the arrangement of its components ensures that there are at least three points for each charged particle trajectory. Its total area covers $\sim 1\,\mathrm{m}^2$ and contains 66 million pixels.
The detector covers the area of pseudorapidity $|\eta| < 2.5$. The pixels' area measures $100 \times 150\,\mu\mathrm{m}^2$, and they are arranged in three barrel layers ("BPix") and two disks at each endcap ("FPix"). The BPix layers are 53 cm long, placed at radii of 4.4, 7.3, 10.2 cm away from the beam axis, and contain a total of 48 million pixels. The Fpix disks have a radius of $6-15\,\mathrm{cm}$, are placed at $z = \pm 34.5$ and 46.5 cm, and contain 18 million pixels.
The position resolution obtained by the pixel detector is $15-20\,\mu\mathrm{m}$.

The silicon strip detector

The silicon strip detector comprises of three subsystems (Inner, Outer and Endcaps) and ensures the measurement of nine hits for each charged trajectory, with at least four of them being two-dimensional. It totals 9.3 million strips and covers an area of $198\,\mathrm{m}^2$.
The Inner detector provides measurements in $r-\phi$. It extends between 20 and

55 cm in radius and comprises of the Tracker Inner Barrel (TIB) and Disks (TID). Its strips have a thickness of 320 μm. The TIB includes four layers, where the strips are placed parallel to the beam and the pitch is larger in the two outer layers, while the TID includes three disks at each endcap, with the strips placed radially.

The Tracker Outer Barrel (TOB) surrounds the Inner detector, and its six barrel layers provide six measurements in $r - \phi$. It extends up to a radius of 116 cm, between $z = \pm 118$ cm, and uses strips with a thickness of 500 μm. The single point resolution of the silicon strips is $23 - 35\,\mu$m in TIB, and $35 - 53\,\mu$m in TOB.

The Tracker Endcaps (TEC+, TEC-) cover the range of $22.5 < r < 113.5$ cm and $124 < |z| < 282$ cm and provide up to nine measurements in $r - \phi$. Each Endcap comprises of nine disks, each of them holding up to seven rings of radial strips. Their thickness is 320 μm on the four innermost rings and 500 μm on the rest.

In addition to these systems, a second micro-strip system is attached to some of their modules. This system is attached to the first two layers and rings, respectively, of TIB, TID and TOB, as well as to rings 1, 2, and 5 of each TEC. These extra modules are mounted back-to-back, with a stereo angle of 100 mrad, in order to provide a measurement of z in the barrel and r on the disks. The achieved single point resolution of this system is 230 μm and 530 μm in TIB and TOB respectively.

2.2.4 Electromagnetic calorimeter

The electromagnetic calorimeter (ECAL)[24] is a hermetic homogeneous calorimeter built of lead tungstate ($PbWO_4$) crystals (Figure 2.3). The choice of its material and the geometric design have been optimized for the reconstruction of electromagnetic objects, with energies relevant for Higgs boson decays, at the intermediate region of Higgs boson mass values (§2.3.1). ECAL is divided into the barrel, covering the pseudorapidity region of $|\eta| < 1.48$, and the two endcaps, at $1.48 < |\eta| < 3$.

The endcap part of ECAL includes a preshower detector (Figure 2.4) consisting of three radiation lengths of lead radiator interleaved with two layers of active silicon strips, covering the region of $1.65 < |\eta| < 2.6$. The main objective of the preshower detector is the rejection of neutral pions imitating single photons through their decay into pairs of closely emitted photons.

More details about the relevant physics and the requirements behind the ECAL design, as well as about the properties of the $PbWO_4$ crystals, can be found in §2.3.

Barrel ECAL

The barrel ECAL (EB) forms a cylinder with an inner radius of 1.3 m. It consists of $61,200$ $PbWO_4$ crystals in the shape of a truncated pyramid, with a

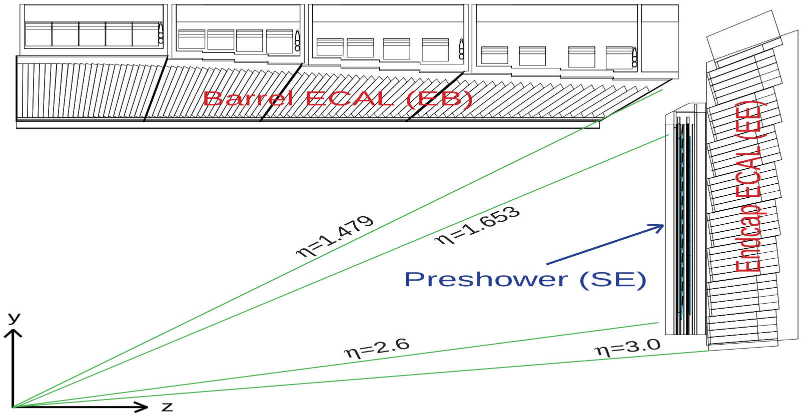

Sq'hma 2.3: *Layout of the electromagnetic calorimeter, showing the arrangement of barrel modules and supermodules, endcap supercrystals and dees, and the preshower detector.*

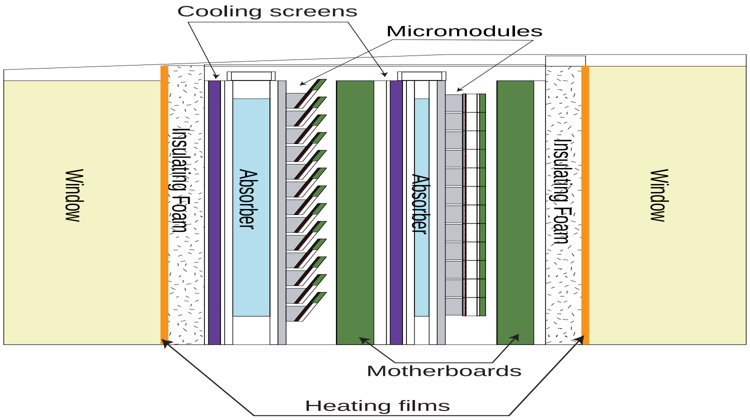

Sq'hma 2.4: *Structure of the preshower detector. The two planes of silicon strips ("micromodules") are oriented vertical to each other.*

front area of $22 \times 22\,\mathrm{mm}^2$ (corresponding to $\Delta\phi \times \Delta\eta = 0.017 \times 0.017$) and a depth of 23 cm, corresponding to $25.8\,X_0$ (radiation lengths). EB consists of 36 supermodules, 18 for each side of the cylinder. There are 17 different shapes of crystals, each shape having a slightly different orientation, while all of the crystals are off-pointing by 3^0 with respect to the nominal collision point, in order to avoid alignment of particle trajectories with the inter-crystal gaps. Each supermodule is segmented into four modules across η, to facilitate this arrangement. Furthermore, matrices of 5×5 crystals share the front-end electronics and form "trigger towers". With this topology, EB is effectively 360-fold in ϕ and (2×85)-fold in η.

Endcap ECAL

The two ECAL endcaps (EE) are 315.4 cm away from the interaction point, after an estimated shift of 1.6 cm inwards when the CMS magnetic field is switched on, and each endcap consists of 7,324 crystals. The crystals are identical truncated pyramids, with a front area of 28.6×28.6 mm and a length of 22 cm, corresponding to $24.7\,X_0$. Each endcap is divided into two halves ("Dees"), while groups of 5×5 crystals form mechanical "units" called supercrystals.

The preshower detector

The preshower detector (ES) is a sampling calorimeter with lead radiators, which initiate electromagnetic showers, and silicon strip sensors placed after each radiator plane, which measure the deposited energy and the transverse shower profiles. The total thickness of the preshower on each endcap is 20 cm. There are two lead plates, the first of which has a thickness of $2\,X_0$, the second of $1\,X_0$. The orientation of the strips in the two silicon planes is orthogonal, with the innermost plane measuring the x and the outermost the y coordinate.

Each of the two silicon planes at each endcap is divided into two Dees; these consist of "ladders", which house several micromodules and their common motherboard. Each micromodule holds one silicon sensor as well as its front-end electronics. The silicon sensors measure $63 \times 63\,\mathrm{mm}^2$, with an active area of $61 \times 61\,\mathrm{mm}^2$ divided into 32 strips at $1.9\,mm$ pitch and nominal thickness of $320\,\mu$m, and they can achieve a spatial resolution of $\sim 300\,\mu$m. The total number of silicon strips is $\sim 137,000$.

2.2.5 Hadron calorimeter

The ECAL is completely surrounded by a sampling hadron calorimeter (HCAL)[25] with coverage up to $|\eta| < 3.0$ and radius $1.77 < r < 2.95$ m (Figure 2.5). The goal of the HCAL is the measurement of the direction and energy of hadron jets, while high hermeticity is essential to the calculation of missing transverse energy (expected from neutrinos or exotic particles). The central HCAL (HB, HE for the barrel and endcaps regions respectively) is a brass/scintillator calorimeter fully immersed

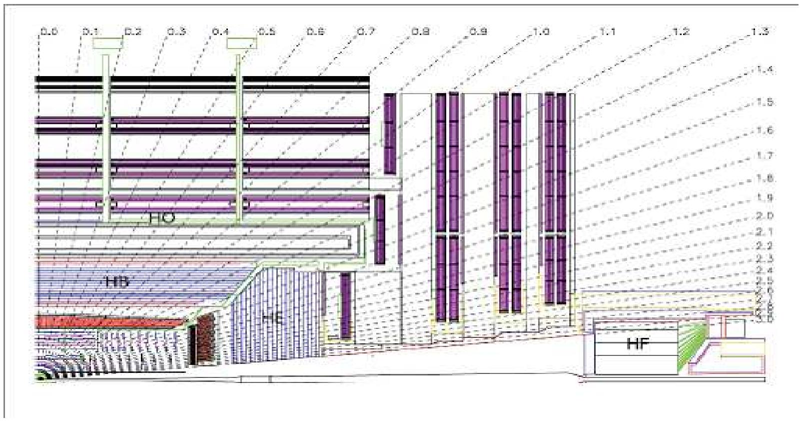

Sq'hma 2.5: *Cross-section of one quadrant of the hadronic calorimeter.*

within the magnetic field of the solenoid. In order to ensure hermeticity, it is complemented by very forward calorimeters (HF) located outside the muon system to complete the coverage up to $|\eta| < 5.2$. The HF are iron/quartz-fibre calorimeters, radiation-hard, located at 11.2 m from the interaction point. In the barrel, the volume allowed within the magnet is not sufficient for full shower containment and therefore an additional array of scintillators is placed outside the magnet (HO). The granularity of the sampling elements has been chosen such that the jet energy resolution, as a function of E_T, is similar in all three main parts of HCAL (HB, HE and HF).

Central HCAL

The central part of HCAL is divided into the barrel (HB) and the endcaps (HE) and covers up to $|\eta| < 3$ (HB covers up to $|\eta| < 1.3$). Both parts consist of brass absorber plates, a choice driven in part by the HE being inserted to the very ends of the solenoidal magnet, and plastic scintillators which are read-out by wavelength-shifting fibres.

The brass plates are $40 - 75$ mm and 79 mm thick in HB and HE respectively, and they are interleaved with the 3.7 mm thick plastic scintillator leaves (made of Kuraray SCSN81). Between ECAL and the first brass plate, there are 9 mm of extra scintillator (made of Bicron BC408) in order to sample hadronic showers developing in the inert material between the two detectors. The segmentation of the active medium is $(\Delta\eta, \Delta\phi) = (0.087, 0.087)$ up to $|\eta| = 1.6$, and $(\Delta\eta, \Delta\phi) = (0.17, 0.17)$ for higher η values, to match the ECAL granularity.

It can be noted that one of the main challenges in the design of HCAL was the mounting of HE to the muon endcap yoke (with the attached ECAL endcaps and ES detectors the weight totals 300 t), in conjunction with the minimization of the accompanying non-instrumented material; as a result a special interface was developed for the accurate positioning of HE.

Outer HCAL

As in the central pseudorapidity region the ECAL and HCAL detectors do not provide sufficient containment for hadronic showers, HCAL is extended outside the solenoid for $|\eta| < 1.3$. The outer HCAL (HO) uses the magnet coils as additional absorbers.
HO contains the same scintillators as the central HCAL, placed at a radius of 4.07 m. Up to $|\eta| \simeq 0.2$, there is a second layer of scintillators at 3.82 m, and an iron absorber between the two layers. This arrangement ensures a total of 11.8 λ_I (interaction lengths) for the whole HCAL in the CMS barrel region.

The forward calorimeter

The forward calorimeter (HF) is essentially a cylindrical steel structure with an outer radius of 130.0 cm, located around the beam pipe at 11.2 m from the interaction point, with a depth of 1.65 m. In order to withstand the extreme radiation at the high pseudorapidity region, the active medium comprises of quartz fibres (with fused-silica core and polymer hard-cladding). The fibres are placed inside holes in the absorber, at a distance of 5 mm from each other in both directions.
The signal is produced via Cherenkov mechanism, when charged shower particles with energies above their respective Cherenkov threshold (*e.g.* 6190 keV for electrons) generate light, which is then guided by the fibres to photomultipliers. This procedure is mostly sensitive to the electromagnetic component of showers, as it is mainly electrons which move at a speed close to that of light inside the medium. In addition, this mechanism renders the detector insensitive to the high neutron flux from showers initiated in the absorber.

2.2.6 Muon system

The muon system[26] is the outermost sub-detector of the CMS experiment, and it is interleaved with the iron wheels which serve as the return yoke of the magnet (Figure 2.6). Its goal is to identify muons and to provide, together with the inner tracker, an accurate measurement of their transverse momenta. This goal is crucial for the CMS, as is also proclaimed in its physics goals, in order to take full advantage of the detectability of muons (which permits the discernment of useful signatures over LHC background) and of their participation in several important channels. These channels include $t\bar{t}$, $W^{\pm}$, Z^0 and Higgs boson decays.
The muon system is composed of three independent subsystems, and, given its large volume and number of cells, gaseous detectors were chosen. The Drift Tubes (DT) are located in the barrel region, the Cathode Strip Chambers (CSC) in the endcaps, and the Resistive Plate Chambers (RPC) in the barrel and endcaps, adding redundancy to the measurement.

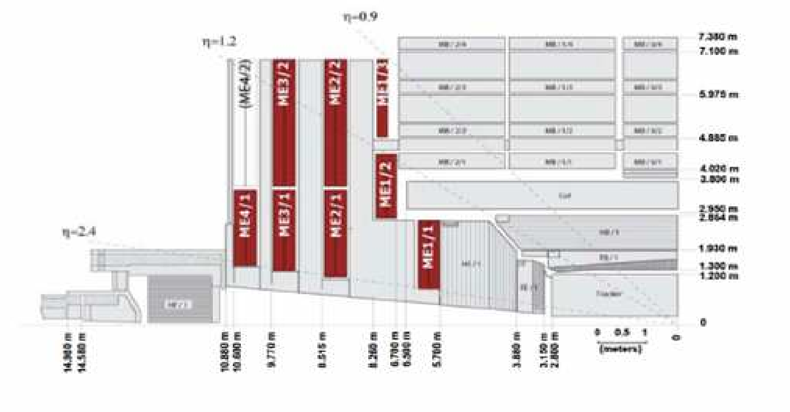

Sq'hma 2.6: *Quarter-view of the CMS detector, highlighting the muon cathode strip chambers at the endcaps.*

Drift tubes

Drift tubes (DT), made of aluminium and containing wires of stainless steel inside a 85% Ar - 15% CO_2 mixture, are installed in layers up to $|\eta| < 1.2$, an area with low track occupancy and low residual magnetic field. In total, there are about $172,000$ wires.

The drift tubes are arranged on four stations, which form concentric cylinders around the beam line. Each of the first three stations contains twelve layers of drift tubes, with wires placed so that eight $r-\phi$ measurements and four z measurements are provided, while the fourth station contains only the z-measuring planes. Each station has twelve unavoidable dead zones in the ϕ coverage because of the yoke supports, although they are placed so as not to overlap in ϕ.

Within single stations, spatial resolutions of $100\,\mu$m in the $r-\phi$ plane and $150\,\mu$m in the $r-\theta$ plane are achieved.

Cathode strip chambers

In the two endcaps, Cathode Strip Chambers (CSC) are used, since in these regions the muon rates and background levels are high and the residual magnetic field between the plates of the yoke is large and non-uniform. They are multi-wire proportional chambers with fast response time, fine segmentation, and radiation resistance. They cover the area of $0.9 < |\eta| < 2.4$, and they overlap with the drift tubes up to $|\eta| = 1.2$.

The CSCs are arranged in four disks (stations) perpendicular to the beam line and placed between the iron disks of the yoke. They comprise of six anode wire planes interleaved with seven cathode planes. The cathode strips, with 5 mm width, run radially outward and provide a precision measurement in the $r-\phi$

bending plane. The anode wires run approximately perpendicular to the strips and are also read out and used at Level-1 trigger, although they provide a coarser measurement; they consist of gold-plated wires of $30\,\mu$m diameter, at a spacing of about 2.5 mm. The total number of wires is about 2 million. The gas mixture used is $\mathrm{Ar} - \mathrm{CO}_2 - \mathrm{CF}_4$. A spatial resolution of $80 - 150\,\mu$m within a single station is achieved.

Resistive plate chambers

Redundancy and accurate time measurement for muon triggering are obtained with a system of resistive plate chambers (RPC), gaseous parallel plate detectors which are installed both in the barrel and in the endcaps and cover the region $|\eta| < 1.6$. The time resolution of RPCs is excellent, much shorter than 25 ns, providing unambiguous identification of the $p - p$ bunch crossing of the event.
The RPCs are double-gap chambers operated in avalanche mode to ensure good operation at high collision rates. They consist of Bakelite planes, coated with graphite layers on which voltage difference is applied to generate the electric field, and read-out strips placed between each two RPCs, gathering the signal from both. A total of six layers of chambers are embedded in the barrel iron yoke, two located in each of the first and second muon stations and one in each of the two last stations. The redundancy in the first stations is intended for low-p_T tracks which may stop before the two outer stations. In the endcaps three layers are present, one for each of the first three stations.

2.2.7 Muon reconstruction

The reconstruction of muons[20] in CMS proceeds in three stages, mainly using measurements from the muon system (§2.2.6) and the tracker detector (§2.2.3). The output of the consecutive stages forms candidates for different levels of the HLT. Initially, the Level-1 trigger runs on simple measurements from the muon detectors, providing muon candidates to the next levels.

The first step of the reconstruction, the "local reconstruction", runs on the output from Level-1 trigger. The specialized software combines the muon hits into muon track segments in each system, using pattern recognition techniques.

In the second stage, tracks are created by fitting the track segments and the detector hits from all three muon subsystems. The fitting is performed by Kalman Filter, using the detector hits as seeds. The formed tracks are called "standalone muons" and are passed to the L-2 of the HLT for the real-time evaluation of the event.
In addition to standalone muons, the segments from the first reconstruction stage are combined with tracks formed in the tracker detector to form a different class of muon candidates, the "tracker muons". This is shown to be more efficient for

muons of low transverse momentum.

In the third stage, the standalone muons are matched to the tracker tracks, and a subsequent common fitting of the detector hits of both tracks is performed. Different hypotheses are used for combining the measurements in the muon stations, in an effort to compensate for the muons' passing through the iron yoke.
Finally, the "global muons" are formed, passed to L-3 of the HLT, and comprise the main class of objects used in the muon identification. There are two additional classes: The "tracker muons" mentioned above, and the "calo muons", which combine tracker detector and calorimetric measurements.

2.3 ECAL design

In this section, the technical characteristics of the CMS ECAL are examined, as consequences of the specifics of the measurement that ECAL has to carry out. With this focus, §2.3.1 presents the considerations occuring from the physics of electromagnetic objects' measurement in CMS, §2.3.2 continues to the specific requirements that those impose on the detector, and §2.3.3 discusses the specifications into which the requirements "translate". With these demands in place, the choice for the components and materials of ECAL (and for the accompanying preshower detector) is discussed in §2.3.4, along with a brief description of its photodetectors and readout chain.
An overview of the ECAL's structure and characteristics can be found in §2.2.4.

2.3.1 Considerations from physics and the LHC environment

The electromagnetic calorimeter of CMS was designed to play an essential role in the study of the physics of electroweak symmetry breaking, in particular for the exploration of the Higgs sector. The CMS "benchmark channels" for Higgs boson discovery are $H \to \gamma\gamma$ in the low ($114 - 130\,\mathrm{GeV}$) mass region, $H \to WW \to 4l$ in the intermediate ($130 - 150\,\mathrm{GeV}$), and $H \to Z^0 Z^{0(*)} \to 4l$ for the intermediate and the high ($150 - 700\,\mathrm{GeV}$) mass regions. The electromagnetic final states were preferred over the hadronic ones because of the large QCD background in the LHC, so the aforementioned channels were the ones to set the CMS design goals, which were specified as[27]:

1. A very good and redundant muon system.
2. The best possible electromagnetic calorimeter consistent with 1.
3. A high quality central tracker to complement 1 and 2.
4. A financially affordable detector.

In addition, there are other "prime" potential discovery channels, enhancing the need for a detector oriented towards good lepton identification. These include the leptonic decays of new heavy vector bosons, $Z' \to 2l$, supersymmetric higgsinos, $h^0 \to 4l$, also any new high-mass object with one or more Z^0's in its decay chain, and cascade decays of gluinos and squarks, where the lepton pair mass provides information about the supersymmetric particle spectrum.

For charged leptons states, an excellent momentum resolution ($\leq 1\%$ below $100\,\mathrm{GeV}$) is desirable to discover the intermediate mass Higgs boson, as well as higgsinos and new heavy gauge bosons. As many of these states are predicted to decay via intermediate vector bosons, a dilepton mass resolution that matches the width of the Z^0 boson is a reasonable requirement.
However, the benchmark for optimizing the ECAL design has been the diphoton channel in the Higgs mass region up to $150\,\mathrm{GeV}$. The natural width of the Higgs

boson mass is expected to be small ($< 10\,\mathrm{MeV}$) in that region, so the observed width will be dominated by the instrumental resolution, therefore dictating a detector with excellent resolution for the electromagnetic energy and the diphoton mass.
Among the backgrounds to the Higgs boson signals, special care needs to be taken against neutral pions which are produced abundantly during the collisions and can be easily mistaken for single photons by their $\pi^0 \to \gamma\gamma$ decay. They carry mostly moderate ($20 - 60\,\mathrm{GeV}$) transverse energy.

Apart from the physics search, the LHC potential posed its own demands, because of the high multiplicity and frequency of inelastic events (estimated to produce $1,000$ charged tracks every $25\,\mathrm{ns}$ at high luminosities), and the background from the minimum-bias interactions. Resistance to the radiation flux was another crucial factor for the choice of detector materials and front-end electronics, while it also had to be balanced against the need for extreme hermeticity.
In addition to these considerations, the electromagnetic calorimeter had to be compact enough to fit along with the hadronic calorimeter inside the CMS superconducting solenoid.

2.3.2 Requirements

The CMS Technical Design Report[20] summarises the requirements from ECAL as "good electromagnetic energy resolution, good diphoton and dielectron mass resolution ($\sim 1\%$ at $100\,\mathrm{GeV/c^2}$), wide geometric coverage ($|\eta| < 2.5$), measurement of the direction of photons and/or correct localization of the primary interaction vertex, π^0 rejection and efficient photon and lepton isolation at high luminosities".
As mentioned in the previous paragraph, the decay of the Higgs boson to two photons has been used as the benchmark for optimising the ECAL design, dominated as it is by the detector performance (while the dilepton mass resolution is set by the width of Z^0). As will be seen in §2.3.4, the requirement for determination of the primary interaction vertex by ECAL was dropped later, with significant change on its overall design.

Mass resolution

As the reconstructed mass of diphotons is given by $m_{\gamma\gamma} = 2E_1E_2(1 - \cos\theta_{\gamma\gamma})$, its resolution depends on the resolution of the photons' energy and the error on their measured angular separation, according to:

$$\frac{\sigma_m}{m} = \frac{1}{2}\left(\frac{\sigma_{E_1}}{E_1} \oplus \frac{\sigma_{E_2}}{E_2} \oplus \frac{\sigma_\theta}{\tan\frac{\theta}{2}}\right)$$

where: $\frac{\sigma_m}{m}$ is the mass resolution, $\frac{\sigma_{E_{1,2}}}{E_{1,2}}$ are the energy resolutions for the two photons, θ is the angle between the two photons, and σ_θ is the angular resolution.

For optimum performance, each term of the energy resolution should be small and of the same order at the relevant electron/photon energies. Also, the direction of the photons has to be measured to a sufficient precision so as not to degrade the mass resolution, especially at high luminosities.

It should be noted that, in addition to the resolution requirements, the calorimeter should be able to detect electromagnetic particles down to very small transverse momenta, $\sim p_t \leq 5\,\mathrm{GeV/c}$, to assure good kinematic acceptance.

Energy resolution

For the energy range of $\sim 25 - 500\,\mathrm{GeV}$, appropriate for photons from the $H \rightarrow \gamma\gamma$ decay, the energy resolution can be parametrised as:

$$\frac{\sigma_E}{E} = \frac{a}{\sqrt{E}} \oplus b \oplus \frac{\sigma_N}{E}$$

where: a is the stochastic term, b is the constant term, and σ_N is the noise term.

The stochastic (or statistical) term represents statistics-related fluctuations such as intrinsic shower fluctuations, photoelectron statistics, sampling fluctuations, as well as effects from dead detector material. The fluctuations in the fraction of initial shower energy which generates a detectable signal, are the factor which places the overall limit on the resolution. While a is at a few percent level for a homogeneous calorimeter, it is typically $\sim 10\%$ for sampling calorimeters.
The constant (or systematic) term is the one which dominates at high energies. It represents the ability to contain shower losses, the uniformity in the response of the channels, and the stability of calibration. Radiation damage of the active medium adds to the constant term of calorimeters operating in a high-intensity environment. Apart from using radiation-hard materials, this effect can be minimised by frequent in situ calibration and monitoring. With effort, b can be reduced to values below one percent, but its relevance is always connected to the value that α can achieve.
Even in the absence of energy deposition in the calorimeter, the read-out chain generates Gaussian noise, which is summed over the channels within a few Moliere radii. The fluctuation of energy entering the measurement area from sources other than the primary particle also contributes ("pile-up energy"). The noise term is responsible for the degradation of the resolution at low energies.

As an illustration, for a Higgs mass around $100\,\mathrm{GeV/c}^2$ the mean photon energy in the central barrel region would be around $50\,\mathrm{GeV}$. If the ECAL constant term is required to be 0.5%, then the stochastic and noise terms in the barrel should be kept around $2\%/\sqrt{E}$ and $150\,\mathrm{MeV}$, respectively, to be of the same order.
In the outer part of the endcaps ($1.5 < |\eta| < 2.0$) the mean photon energy would

be around 140 GeV. This means that, keeping the same constant term, higher stochastic and noise terms are acceptable (around $5\%/\sqrt{E}$ and 250 MeV).

Angular resolution

In order to not dominate the mass resolution, the angular resolution should be around $50\,\mathrm{mrad}/\sqrt{E}$. The angular measurement requires the photon incidence positions on the ECAL to be measured accurately, as well as exact calculation of the primary vertex position. However, the latter depends strongly on the precise knowledge of the minimum-bias pileup at LHC energies.

Radiation hardness

Several physics search channels, in particular the Standard Model Higgs decays and various supersymmetric channels, require an extremely hermetic ECAL with high geometric acceptance. However, the coverage at high η is limited by the radiation dose which would be received. At the barrel (endcaps) region, for an integrated luminosity of $5 \times 10^5\,\mathrm{pb}^{-1}$, corresponding approximately to ten years of LHC running at nominal luminosity, the ECAL would receive an estimated dose of 0.5 krad (> 7 Mrad) and an equivalent neutron fluence of $2 \times 10^{13}\,n/\mathrm{cm}^2$ ($> 10^{14}\,n/\mathrm{cm}^2$). The active material, as well as the electronics and readout, have to be suitable for such a hostile environment.

Background rejection

The spatial separation between the two photons emitted from the decay of neutral pions within hadronic jets is ~ 1 cm in the barrel region of CMS, but much smaller at the endcaps. The distinction of the two photons, which will otherwise mimic one single photon, necessitates either adequately fine granularity of the ECAL cells, or the presence of a preshower detector.

Read-out speed

The time between proton bunches crossing at nominal LHC operation is 25 ns. It is obvious that the correct identification of collision events and handling of the pile-up energy necessitates the use of active material with short decay constant, as well as a quick read-out chain and front-end system.

2.3.3 Specifications

Types of detectors

In general, with sampling calorimeters it is difficult to obtain a stochastic term below about $10\%/\sqrt{E}$ without demanding strict mechanical tolerances, while homogeneous calorimeters have the potential to achieve stochastic terms of $\sim 2\%/\sqrt{E}$

due to their much smaller sampling fluctuations. In this case the challenge is the control of systematics which build up the constant term, which with effort can get as low as 0.5%. However homogeneous calorimeters do not provide longitudinal measurement, and are generally more expensive than sampling ones.

Apart from the calorimeter, the use of a preshower detector could enable the identification of pairs of photons from neutral pion decays (§2.3.2), especially in the endcaps region, where their spatial separation is smaller than the size of a typical calorimeter cell.

In principle, an important distinction between homogeneous and sampling calorimeters is that homogeneous ones aim at optimising the energy resolution (with their low stochastic term), while sampling calorimeters optimise the measurement of the direction of particles.

A usual choice for electromagnetic calorimeters is the use of scintillating crystals. The reason behind using crystals is that heavier materials are richer in electrons which interact strongly with light, while at the same time ordered systems can confine electrons in well separated energy bands, thus rendering the material transparent to its scintillation light. (In scintillation, light is emitted from the transition between a conduction band, where the electrons end up after excitation, and a valence band.) However, an obvious drawback of crystals is the inability to partition into smaller readout cells.

All the aforementioned facts were taken into account during the design of the detector and the choice of its material (§2.3.4).

Quantities

As mentioned in §2.3.2, the desired values for the stochastic term in the energy resolution are $\leq 2\%/\sqrt{E}$ in the central region, and up to $\leq 5\%/\sqrt{E}$ in the forward region.

The stochastic term relies on a good and stable sampling of the electromagnetic shower. A usual choice for the detector dimensions in crystal calorimetry is a length of $\sim 25\,X_0$ (radiation lengths), which contains almost all of the energy in an electromagnetic shower for the energies relevant at the CMS (§2.3.1), even more so for materials of lower atomic number, and a lateral area of $\sim 1 \times 1\,\rho_M$ (Moliere radius), which gathers $\sim 90\%$ of an electron's initial energy.

Understandably, the smaller the radiation length and Moliere radius of a medium the better it is, since this allows for a smaller detector and a more accurate measurement. High density is also crucial, in order to convert all of the incident particles' energy into light[30].

In addition, a good stochastic term depends heavily on the light yield, which should be high and preferably with output at a wavelength compatible with the available photodetectors' range (usually $\sim 400\,\mathrm{nm}$), and/or on photodetectors with good intrinsic gain. The photodetectors' area and quantum efficiency also influence the overall light yield. In addition, a small dependence of the light output on temperature and generally good mechanical properties are also essential.

For the constant term in the energy resolution, which practically forms the limit of the resolution value at high particle energies, the acceptable value is around 0.5%. This is achieved mainly by controlling the longitudinal leakage (therefore the depth of the active material), the effects of dead material, the calibration and intercalibration of the cells, and the radiation damage. The latter requires a sufficiently radiation-hard material and the monitoring of the active material during the detector's operational lifetime with the use of flashing light and laser, and it is quantified by requiring that the light attenuation length remains always > 3 times the crystal length. An additional issue is the longitudinal uniformity of the light collection which has to be ensured (*inter alia,* by accounting for focusing effect, attenuation).

The noise term in the energy resolution is expected to be kept around 150 MeV. The noise has dependence on the shaping time ($t_{sh.}$) in a complex way, through two of its sources, photodetector capacitance and dark current (which depend on $1/\sqrt{t_{sh.}}$ and $\sqrt{t_{sh.}}$ respectively). It also involves control of the equivalence of electronics noise to energy, and of the handling of the pile-up energy. The latter involves the fast shaping of signals and an inner detector radius large enough to enable good separation of objects. This last specification also stems from the requirement of good angular separation.
In the case of scintillating crystals, fast shaping and good read-out speed are related to the detector material having a short decay constant with no slow component. This can be enhanced with dopants, by creating a high concentration of acceptor levels which can speed the transition from the conduction band (however this is also expected to diminish the light yield).

Concerning the detector dimensions, the choice of the inner radius of the electromagnetic calorimeter was governed by many issues. As mentioned above, the pile-up, especially at high luminosities, and the two-shower separation ability drive the inner radius to larger values; while the installation of both calorimeters inside the coil, the cost of crystals, and the compactness of the overall detector drive it to smaller values. Eventually, allowing a radial space of 60 cm for the electromagnetic calorimeter and fitting $\sim 7\,\lambda_I$ of total calorimetry inside the coil (at $\eta = 0$) led to an inner radius of 1.3 m for the ECAL. At this radius, and for an approximate area of $\Delta\eta \times \Delta\phi \simeq 0.1 \times 0.1$ used for measuring the energy of a high-energy photon or an electron, there is an estimated average of 130 MeV of pile-up energy at a luminosity of $L = 10^{34}\,\mathrm{cm}^{-2}\mathrm{s}^{-1}$.
The final choice on the pseudorapidity coverage is $|\eta| < 2.6$, as the radiation dose doubles from $|\eta| = 2.5$ to $|\eta| = 3$. The resulting loss in efficiency affects mainly the $H \rightarrow 4l$ channels, by $\sim 20\%$.

Concerning the sensors, in addition to the intrinsic gain, area and quantum efficiency mentioned for the stochastic resolution term, other crucial characteristics are the stable response, tolerance to magnetic field, and compactness.

Finally, an overall acceptable cost for the detector materials and construction is essential.

In summary, the relevant quantities which have to be controlled to obtain the requirements described in §2.3.2 are:

- The radiation length and Moliere radius of the material should be as small as possible, with a density as high as possible; the Moliere radius and the total active length are additionally constrained by the outer radius of ECAL and its fitting inside CMS.
- The light yield of the material should be as high as possible, preferably with a wavelength compatible with the photodetectors' range.
- Small scintillation decay constant.
- Good radiation hardness of the material.
- Inner detector radius as large as possible (eventually fixed at 1.3 m by global CMS considerations).
- Concerning the photodetectors: gain, area, quantum efficiency and stable response are important.
- Finally the uniformity of the active material, as well as the control of dead areas, irregularities and calibration, all play an essential role.

2.3.4 Design and materials

ECAL history

Taking into account all the issues discussed above led to a decision about "a high energy resolution calorimeter using scintillating crystals readout with silicon photodiodes".
However the proposed design underwent changes as regards the material and the topology of the readout, before the current design was finally put forth and implemented. Initially, the proposals were also driven by the requirement for measuring the shower position in at least two depths, in order to provide a direct measurement of the photons' direction, a fact which changed later.
The first suggestion ("CMS Letter of Intent")[28] involved an electromagnetic calorimeter built of cerium fluoride (CeF_3) crystals, segmented longitudinally into two parts, with a lateral area of $\Delta\eta \times \Delta\phi = 0.02 \times 0.03$. In the early 90's, CeF_3

was the best choice available for satisfying the requirements and specifications for ECAL (§2.3.2, §2.3.3).

For the neutral pion rejection and the measurement of the photon direction, two possibilities were considered: Either a lateral segmentation of the first longitudinal part into four parts of $1.2 \times 2\,\text{cm}$ area, to a depth of $8\,X_0$, followed by a part of $\geq 17\,X_0$; or a position detector of 2 mm pitch, placed after the first longitudinal part, which would be $4-5\,X_0$ deep.

An alternative suggestion was also considered and tested at the same time, that of a lead/scintillator sampling calorimeter, read out by plastic wavelength shifter fibres running perpendicular to the plates through holes[27]. This kind of structure ("shashlik") permits the quick extraction of light from the scintillators. The detector under consideration consisted of 2 mm thick Pb and 4 mm thick scintillator plates, with a total of $26\,X_0$ depth extending to $\sim 45\,\text{cm}$. The fibres had a separation of 9.5 mm. The stochastic term was brought down to $\sim 8\%/\sqrt{E}$.

The technical advantages of CeF_3 were considered marginal with respect to the "shashlik", which had a lower cost. In 1992 however a new material for crystals was presented for use in high energy physics, lead tungstate (PbWO_4). Its characteristics are discussed in detail in the next section, as it formed the final choice for ECAL. All three designs were tested in a beam test in 1994, with PbWO_4 performing better with the design described below.

The preshower detector

Meanwhile, it was determined that a fine lateral size of crystal cells would be enough to distinguish photons from π^0 decays in the barrel region, although not at the endcaps. Therefore, the decision for a preshower detector at the endcaps was taken, consisting of two orthogonal overlapping planes of silicon strips with 2 mm pitch, measuring the x and y coordinates, placed after $\sim 3X_0$ of lead at each of the two endcaps.

However, it was still considered necessary for the ECAL to provide measurement at two depths during the LHC operation at high luminosity ($10^{34}\,\text{cm}^{-2}\text{s}^{-1}$), in order to determine the photons' direction and the primary vertex to which they belong. To this end, it was decided to use PbWO_4 crystals without any longitudinal segmentation, but with the addition of a preshower detector in front of the crystals during the high luminosity period, at the region $|\eta| \leq 1.1$. The barrel preshower was decided to consist of a single plane of silicon strips, measuring the z coordinate, behind $\sim 2.5X_0$ of lead.

Some details can be added here about the choice of the passive and active material for the CMS preshower detectors and their dimensions[31]. The optimum thickness of an absorber is $\sim 3X_0$, resulting from a balance between the probability to initiate a shower from a photon (given by $P = 1 - e^{-(\text{thickness}/X_0})$ and to

not degrade the performance of ECAL. Lead was chosen due to its high density, although, because of its malleability, it needs to be “sandwiched” between thin layers of aluminum for structural rigidity.
Solid-state detectors offer in general compactness and good segmentation, with linear response even in the dense core of electromagnetic showers. A usual choice of using p^+ strips on n bulk structure with DC-coupled electronics was made, and during the 90’s an international program was implemented for the development of wide-strip silicon detectors.
The size of the strips was determined by the area of the silicon wafers feasible to be constructed, along with a balance between the requirements for smaller strip size (from low noise and occupancy) and for larger one (for lower cost, and to avoid dominance from the sampling fluctuations).

After the initial proposal, two subsequent changes took place until the design of the preshower detector was fixed. First, the single $3X_0$-thick layer was abandoned[31]; the reason was the spiraling of low-energy charged shower particles after they leave the absorber, because of the presence of the magnetic field. This would cause “shifted” energy deposits in the second plane, which would result in a degradation in the π^0 rejection. Since placing the sensors as close as possible to the absorber turned out to be crucial, a design with two lead layers, of $\sim 2 + 1X_0$ thickness, was adopted. Finally, it was determined that there was no need for the ECAL to measure the photon direction or the interaction vertex, as this task could be carried out by the tracker detector. Therefore, the plans for a barrel preshower detector were abandoned[24].

A description of the final structure of the preshower detector is found in §2.2.4.

Lead tungstate crystals

A new kind of crystal was developed by the CMS collaboration using lead tungstate ($PbWO_4$), in an effort which started in 1992 and lasted almost a decade[24]. Lead tungstate is very effective at energy containment (because of its values for X_0, ρ_M and density, Table 2.2), and resulted in a detector with fine granularity and compactness. In addition, it is a quite fast scintillator, with $\sim 80\%$ of the light emitted within 25 ns. However, it has very poor light output ($\sim 100\,\gamma/\text{MeV}$) which is also temperature-dependent ($-2\%/^0\text{C}$). This issue had been overcome in part by the development of large-area silicon avalanche photodiodes for the readout, along with a sufficient cooling system.
An important part of the crystal development had been aimed towards the study and prevention of radiation damage. Ionising radiation forms colour centres in the crystals through impurities in the lattice and oxygen vacancies; the result is loss in light transmission, subject to the balance between damage and self-recovery. Eventually the best solution came from doping of the crystals with niobium and yttrium, which suppresses the colour centres.

	Radiation length X_0 (cm)	Density $\rho\,(g/\mathrm{cm}^3)$	Moliere radius ρ_M (cm)	Decay time τ (ns)	Maximum wavelength λ (nm)	Light yield LY (%NaI)
CeF_3	1.68	6.16	2.6	30	310/340	5
$Bi_4Ge_3O_12$	1.12	7.13	2.4	300	480	10
$PbWO_4$	0.89	8.3	2.2	15	420	0.5

P'inakas 2.2: *Properties of lead tungstate, compared to other materials commonly used in high energy physics.*

Finally, the crystals for the barrel region were constructed with a length of 23 cm, i.e. $25.8\,X_0$, and a lateral area of 2.2×2.2 cm, i.e. $1 \times 1\,\rho_M$. At the endcaps, they have a front area of 2.86×2.86 cm and a length of 22 cm, corresponding to $24.7\,X_0$. All crystals have the shape of truncated pyramids.
Details about the overall structure of the detector are found in §2.2.4.

ECAL photodetectors and read-out chain

Adding to the problem of lead tungstate's low light yield, the standard amplifying photodetector tubes cannot operate well in the magnetic field of 4 T. Therefore, silicon avalanche photodiodes (APDs) were used for the readout of the ECAL barrel crystals, and vacuum phototriodes (VPTs) for the endcap crystals[24][20]. The APDs have a significant internal gain of 50 up to 200, good quantum efficiency, and they can operate in the high magnetic field, but are unsuitable for the radiation at the endcaps. The light-to-electron conversion and the subsequent electron multiplication take place in a thickness of a few tens of μm, so they are both thin and non-sensitive to minimum ionising particles traversing the crystal (a minimum ionising particle traversing the APD is equivalent to ~ 100 MeV of energy deposited in the crystals). However the maximum area at which the APDs can be constructed is 5×5 mm, and therefore a pair of them is glued to the rear surface of each crystal. The VPTs are photomultipliers with gain ~ 10, and measure 25 mm in diameter, so there is one VPT attached to each endcap crystal.

In ECAL the crystals are complemented by a "light-to-light" readout chain, which begins with the photodetectors and the collection of scintillation light at the rear end of the crystals. The light output is thus converted into electric current, which is received by the front-end amplifiers and converted into voltage. This signal reaches the front-end electronics where the digitization is performed (along with other treatment of the signal, like pedestal adjustment and zero suppression), and therefore they deliver information in the form of bits. Finally the digitized signal is once more transformed to light, to be transmitted through optical fibres and leave the detector for the data acquisition system, in order to be used for triggering and possibly stored for offline analysis.

Κεφάλαιο 3

ECAL Studies

In this Chapter the reconstruction of electromagnetic objects in CMS and some relevant studies are presented.
The reconstruction of electrons and photons in the official reconstruction software is first introduced briefly. Then, three studies connected to the measurement of energy, position, and clustering in the electromagnetic calorimeter (ECAL) and the preshower detector (ES) are discussed in detail.
In addition, a brief presentation of the reconstruction of electromagnetic objects in the CMS Particle Flow algorithm is included in the last study.

3.1 Electron and photon reconstruction

Electrons are mainly characterized by the presence of a charged track pointing to a deposition of energy from an electromagnetic shower. Therefore the reconstruction of electrons[20][32] consists of the handling of measurements from the ECAL and tracker detectors and, to some extent, HCAL. Its main steps are briefly described in this paragraph. The "online" reconstruction steps, *i.e.* those performed by the triggering system (§2.2.2), have similarities to those performed "offline", *i.e.* on the stored data by the reconstruction software. Therefore, in order to give a more concise overview, the triggering steps will be described in parallel with the reconstruction steps.
In addition, the reconstruction chain for photons[20][33] practically forms a subset of the one for electrons, therefore it is included in the same description in a way that should cause no ambiguity.

L1 Trigger - Trigger primitives

Before the actual reconstruction starts, electromagnetic candidates are formed by the transverse energy measurement of adjacent ECAL trigger towers (*i.e.* groups of 5×5 crystals sharing the same readout electronics, §2.2.4). These "trigger primitives" are passed to the Level-1 trigger system (§2.2.2), where they are combined to form electron and/or photon candidates.

Clustering - Energy corrections

After the Level-1 trigger, the reconstruction is initiated by the ECAL measurement, and more precisely with the grouping of $PbWO_4$ crystals.
The main issues shaping the techniques developed for the reconstruction and identification of electromagnetic objects, including the grouping of individual channel (*i.e.* crystal) measurements to clusters, are linked to the presence of the tracker's and services' material budget in front of the calorimeters. The ECAL clustering algorithms are designed towards an appropriate combination of energy deposits in individual crystals for each incoming particle. An issue they specifically address is the spread of energy because of bremsstrahlung and conversions of secondary photons inside the tracker detector.
The grouping begins by the formation of clusters around crystals with the highest local energy deposits, when these are above $\sim 2\sigma$ over the electronics' noise. The clustering algorithm uses these crystals as seeds in the barrel region; it then runs over a fixed length of crystals in pseudorapidity η, performing a dynamical scan across the azimuthal angle ϕ until either a larger energy deposit or no deposit at all is encountered, thus defining the boundaries of a cluster. The clusters are grouped into "superclusters" in a similar way. The algorithm's extension in ϕ aims at minimizing the containment variations due to the strong magnetic field.
The superclustering in the endcaps region proceeds similarly, but the clustering uses a slightly different algorithm, which adds together clusters of fixed 5×5 size. The cluster positions are extrapolated to the ES, and ES clusters are built around them (§3.3.3). The total endcap energy is a linear combination of cluster energies in the endcaps and the geometrically matching ES clusters.
The barrel algorithm was designed for high-energy electrons and has also been tuned to work well for lower energies. However, in the case of single showers such as those coming from unconverted photons or electrons in beam tests, energy sums over fixed arrays of crystals offer better resolution.

The position of an ECAL cluster is calculated by weighting the mean position of the crystals, x_i, by the logarithm of their relative energy, E_i (the logarithm is taken since the energy density in a shower decreases exponentially with the distance from its core):

$$x = \frac{\Sigma x_i \cdot w_i}{\Sigma w_i}, \qquad \text{with weight } w_i = w_0 + \log \frac{E_i}{\Sigma E_j}.$$

The position of the supercluster is obtained from the mean of the energy-weighted positions of its clusters.

Certain corrections on the energy measured are required and can be pre-calculated and applied as functions of coordinates and energy. Their sources are: Rear leakage close to the cracks between modules and supermodules as a result of the reduced effective depth, containment variations because of the spread of energy due to showering inside the tracker and because of the variation of its material - and, in the special case of fixed-array clustering, lateral front leakage with dependence on pseudorapidity, and containment variations depending on the shower incidence position. The last variation is known as "local containment" and a method developed for its treatment in the ECAL Beam Test of 2006 is discussed in §3.2.

In the case of photon candidates, the final energy measurement depends upon the ratio of the energy contained within the 3×3 array of crystals centered on the seed crystal to the total energy of the supercluster. This quantity is used to determine if the photon is converted or unconverted. If the γ is unconverted, then the energy of the 5×5 crystals around the crystal with highest energy is used. Otherwise, the energy of the whole supercluster is used.

L2 Trigger

The first stage of the HLT for electrons, L-2, checks the spatial matching of the reconstructed superclusters with the trigger primitives, essentially verifying the Level-1 trigger results. Also, this is the only HLT step used for photons.

Matching between ECAL measurement and tracker hits

The position of the supercluster is propagated backwards to the tracker detector, in order to find the associated hits in the pixel detector (§2.2.3). The propagation is done on a helical trajectory taking into account the magnetic field, and under both charge hypotheses. After the innermost pixel hit compatible with the supercluster within a predefined geometrical window in (η, ϕ) is found, it is used to make an updated calculation of the trajectory, and search for a second hit within a narrower window in the next pixel layers. These two innermost hits are the "seeds" which will be used to initiate the electron track building.

L2.5 Trigger

The second step of the HLT is based on the search for hits in the pixel detector described above. If pixel hits consistent with a supercluster are found, then an electron candidate is formed, otherwise a photon candidate is formed.

Electron track building

The track building is initiated from the innermost pixel hit found, by propagating the state vectors (*i.e.* momentum and direction information) of each hit to

the next detector layer.
The radiation losses after each hit in the tracker layers do not follow a Gaussian distribution, which would be the case in *e.g.* multiple scattering. For this reason the propagation is performed using Gaussian mixtures[34] for the distribution of the state vectors and their errors, and Bethe-Heitler modeling for the energy losses. This algorithm is found to model particularly well the electron track at its two ends, enabling the calculation of the momentum at its inner and outer points and the calculation of the electron isolation, which are to be used in the final steps of triggering and preselection.

Electromagnetic object isolation

The two detectors whose isolation measurement is useful for the triggering and the preselection for the electron reconstruction are the tracker and the hadronic calorimeter (HCAL).
The tracker isolation calculation consists of summing the transverse momentum of tracks found within a hollow cone around the candidate's track. The tracks entering the sum have to pass a momentum threshold, $p_T > 1.5\,\mathrm{GeV/c^2}$, and originate from a point consistent with the candidate's calculated interaction vertex in the longitudinal direction, $|z^e - z^{trk}| < 0.1\,\mathrm{cm}$. The cone lies within $0.02 < \Delta R < 0.2$ ($\Delta R = \sqrt{\Delta\phi^2 + \Delta\eta^2}$). The exclusion of the cone's central region aims at excluding the contribution from bremsstrahlung radiation and its subsequent conversions to electron pairs.
The HCAL isolation is calculated by the sum of the energy deposited in the HCAL towers, within a cone of $\Delta R < 0.15$ behind the ECAL seed cluster.

For photons, the detectors used for the isolation are ECAL and HCAL. A description of the isolation variables can be found in §4.3.3, where they are used for the photon identification.

L-3 trigger

Eventually, the relative isolation sum of the tracks with respect to the candidate's transverse momentum, as described above, and the sum of the HCAL energy are examined. As a final requirement, the ratio of the energy of the ECAL cluster which seeds the supercluster over the momentum at the beginning of the track is calculated and checked.

Final preselection - Track-ECAL matching

The reconstruction preselection uses additionally the ratio of the calorimetric activities, defined for electrons as the ratio of the energy deposited in the HCAL towers behind the ECAL seed cluster, over the seed cluster's energy. The ratio has to be $H/E < 0.2$. For photons, the whole ECAL supercluster is used, and the ratio must be $H/E < 0.5$, while the supercluster must have $E_T > 10\,\mathrm{GeV}$.

Finally, a spatial matching between the track and the supercluster is performed for electrons. The two relevant variables are

$$\Delta\eta_{in} = \eta_{SC} - \eta_{trk}^{extr.}, \;\; \Delta\phi_{in} = \phi_{SC} - \phi_{trk}^{extr.}$$

where η/ϕ_{SC} is the supercluster's position, and $\eta/\phi_{trk}^{extr.}$ is the closest point to the supercluster's position after extrapolation of the track from its innermost point.

Photon conversions

In addition to photon reconstruction, a check for photon conversions is performed. After a loose supercluster preselection, a backward propagation starts from each cluster of the supercluster, taking into account the measured ECAL energy and the expected mean energy loss of electrons in the tracker material. For the tracks which are built in this way, the innermost tracker hits are used as starting points for the other arm of the conversion, by moving outwards. All found tracks with opposite charges are combined and conversion candidates are formed. The candidates are finally examined for the angular separation in $\Delta\phi$ and $\Delta\cot\theta$ between the two arms, and for the χ^2 value of the vertex fitting.

3.2 Crystal containment corrections in the energy measurement

3.2.1 Energy containment in ECAL crystals

A fraction of the energy of incoming electromagnetic particles will be lost to ECAL because of showering in the gaps between adjacent crystals, modules, and supermodules. In addition, when the energy deposited in ECAL by a particle is summed over a fixed array of crystals there is variation in the energy containment between events. The magnitude of both these effects depends on the particle's position of impact on the crystal's surface. More specifically, the energy containment depends on the distance of the incidence point from the crystal surface's two central axes, decreasing towards the crystal edges.

3.2.2 Ln(E2/E1) Method

The containment variation can be compensated for with the use of predetermined correction functions, according to the position of the impact point. Two methods have been developed for their derivation, which use the pattern of the energy deposition in the cluster for measuring the "centrality" of the impact on the hit crystal.

The first method determines the impact position, and subsequently its distance from the crystal centre, by weighting the positions of all crystals in the surrounding array according to the logarithm of the energy received by each crystal.

The second method, known as "Ln(E2/E1)"[35], is the one used in the analysis presented here[36]. This method calculates the point of incidence of the particles on a crystal's surface by using the balance of energy deposited in subgroups of the surrounding crystals.

As shown in Figure 3.1, in the case of the energy summed on an array of 3×3 crystals, two submatrices E_1, E_2 of either 3 or 6 crystals are defined, according to the energies W_2, W_1 deposited on the two immediate neighbours of the central crystal. The orientation of the submatrices always remains the same, with W_1 (and E_2) towards higher values of η or ϕ, but the number of crystals in each submatrix varies: The neighbour which acquired the largest energy always denotes the smaller submatrix. (Corresponding definitions are used for the 5×5 array.)

There is a rough correspondence between $\ln(E_2/E_1)$ values and the x, y coordinates, as confirmed by test beam measurements (Figure 3.2). Events impacting near the centre of a crystal deposit most of their energy on the middle column of the matrix, resulting in higher mean values of $\ln(E_2/E_1)$, while events near the crystal edges divide their energy almost equally between the two submatrices and have a value close to zero.

Using this parametrisation, the crystal's surface is divided into bins of $\ln(E_2/E_1)$,

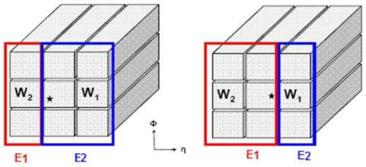

Sq'hma 3.1: *Definition of submatrices across the* η *direction for the "Ln(E2/E1)" method, for the energy sum on an array of* 3×3 *crystals.* E_2 *is always the submatrix at the side of higher* η*, and vice versa for* E_1*, but their size is defined by the energy deposition (*W_1*,* W_2*) on the hit crystal's immediate neighbours. The figures show the cases for a)* $W_2 > W_1$*, b)* $W_2 < W_1$.

and the gaussian mean of the energy measurements in each bin is plotted as a function of $\ln(E_2/E_1)$, and it is normalized to the largest energy value.
The correction functions are then obtained by fitting the distribution. The fit is performed for each half of the crystal independently, using third-degree polynomials. The analysis is performed independently across each direction, for arrays of both 3×3 and 5×5 crystals centred around the hit one. Figure 3.3 is an example of the plots obtained for an individual crystal after the analysis.

3.2.3 Beam test and event selection

An overview of ECAL can be found in §2.2.4, but it is useful to repeat at this point that the ECAL barrel consists of 36 "supermodules", each of them holding 1700 $PbWO_4$ crystals. Each supermodule is segmented into four "modules" along its long side, *i.e.* across the η direction of CMS.
This study uses data collected during the 2006 ECAL Beam Test, which took place at Point H4 of the SPS accelerator at CERN. During this Beam Test, nine ECAL supermodules equipped with the full readout electronics have been tested using electrons in an energy range between 15 GeV and 250 GeV. The quasi-projective geometry of ECAL inside CMS was retained with respect to the beam. The impact point position of the beam on the crystals' front face was measured with an accuracy of $125\,\mu$m by four planes of fibre hodoscopes.
When analyzing each direction, only events lying on a narrow band in the other direction were kept (within either ±2 mm or ±4 mm around the mean incidence point) in order to disentangle the effects of the two directions. The analysis was performed both on individual crystals and on groups of crystals (*e.g.* crystals on the same module) by taking their average containment of energy.

An analysis with simulated data was performed in parallel. The overall agreement with the Beam Test results was good, except for one case which is discussed

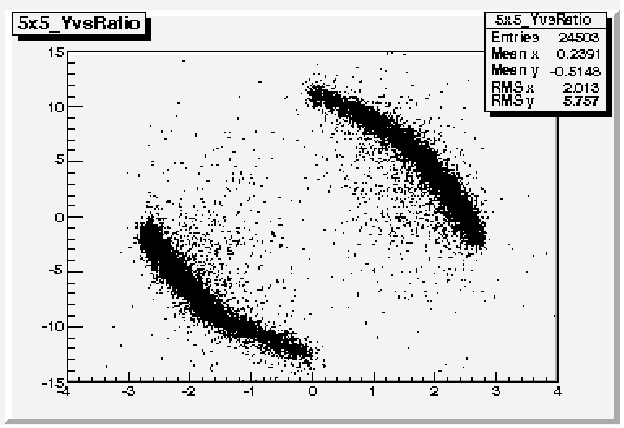

Sq'hma 3.2: *Correspondence between the distance of the incidence point from the crystal centre (vertical axis) and the* $\ln(E_2/E_1)$ *value (horizontal axis); in this example, for energy summed on* 5×5 *crystals, across the* ϕ *direction.*

3×3 crystals		5×5 crystals	
lower η	higher η	lower η	higher η
$1.2 - 2.3\%$	$2.1 - 3.0\%$	$0.5 - 2.0\%$	$1.1 - 2.1\%$
lower ϕ	higher ϕ	lower ϕ	higher ϕ
$0.4 - 1.9\%$	$1.2 - 2.9\%$	$0.1 - 1.5\%$	$0.5 - 1.8\%$

P'inakas 3.1: *Overall ranges of energy loss for impact at the crystal edges, with respect to impact at the crystal centre.*

in the next paragraph.

3.2.4 General characteristics of the containment - Derivation of the correction functions

The overall percentage of energy losses for electron incidence close to the crystal edges, with respect to incidence close to the centre, lies within the ranges shown in Table 3.1.

The results justify the derivation of "sets" of containment correction functions, where each set would consist of separate functions for (i) 3×3 and 5×5 arrays, (ii) each direction (η/ϕ), and (iii) each half of the crystal (*i.e.* in the manner of Figure 3.3).

The asymmetry in containment between the opposite edges of the crystals across

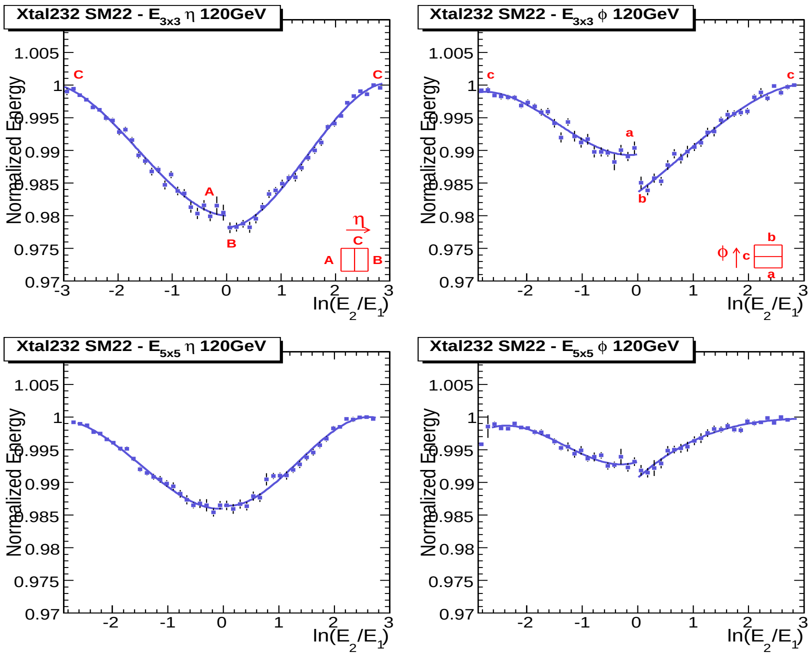

Sq’hma 3.3: *Normalised energy vs.* $\ln(E_2/E_1)$ *on one of the studied crystals, fitted with* 3^{rd} *degree polynomial functions. Upper row: energy summed on* 3×3 *crystals; lower row:* 5×5 *crystals. Left column: results across* η*; right: results across* ϕ*. The schematic index shows the correspondence between* $\ln(E_2/E_1)$ *and the crystals' surface.* $A(a)$ *and* $B(b)$ *denote the opposite edges of the surface across the* $\eta(\phi)$ *direction, while* $C(c)$ *corresponds to its centre.* $B(b)$ *is the edge with the higher value of* $\eta(\phi)$*.*

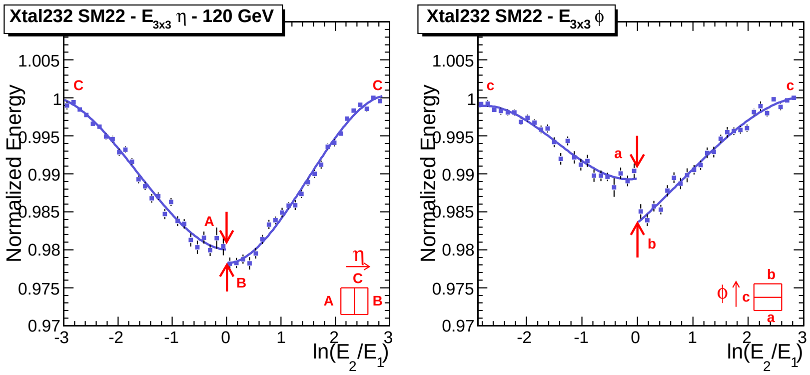

Sq’hma 3.4: *Normalized energy vs.* $\ln(E_2/E_1)$ *on one crystal: Asymmetry between opposite edges across the same direction. (Energy summed on* 3×3 *crystals; left:* η*, right:* ϕ*.) The schematic index shows the correspondence between* $\ln(E_2/E_1)$ *and the crystals’ surface.* $A(a)$ *and* $B(b)$ *denote the opposite edges of the surface across the* $\eta(\phi)$ *direction, while* $C(c)$ *corresponds to its centre.* $B(b)$ *is the edge with the higher value of* $\eta(\phi)$*.*

the same direction, which calls for separate functions for each half of the crystal, is demonstrated in Figure 3.4. This asymmetry is expected because of the quasi-projective geometry of the supermodules, and it is enhanced by keeping only those events which deposited the largest part of their energy at the hit crystal.
On the other hand, the need for separate corrections for each direction (Figure 3.5) is not fully understood. All analysed crystals had larger energy loss across their η direction than across ϕ at an average of $\sim 0.5\%$, independently of the specific half-side or the size of the array, an effect which is in contrast with the simulation but which was also present in studies with data from the 2004 Beam Test[37]. Two possible explanations are the construction of the supermodules being less uniform across η, and effects arising from the intercalibration coefficients (discussed below).

The containment was found to be practically independent of the beam energy up to 150 GeV (Figure 3.6).

Notably, all the features mentioned above are observed on different supermodules indistinguishably, indicating that the same corrections could be globally used on all ECAL barrel supermodules.
However, analysis on crystals located on different modules of the same supermodule showed an overall dependence of the energy loss on the module. The losses became more significant moving towards modules of higher η. The variation reaches $\sim 0.5\%$ and $\sim 0.8\%$ for the η and ϕ directions on the surface respectively, when comparing between crystals of lowest and highest η values across the supermodule. In any case, this dependence describes the *average* behaviour of crystals in diffe-

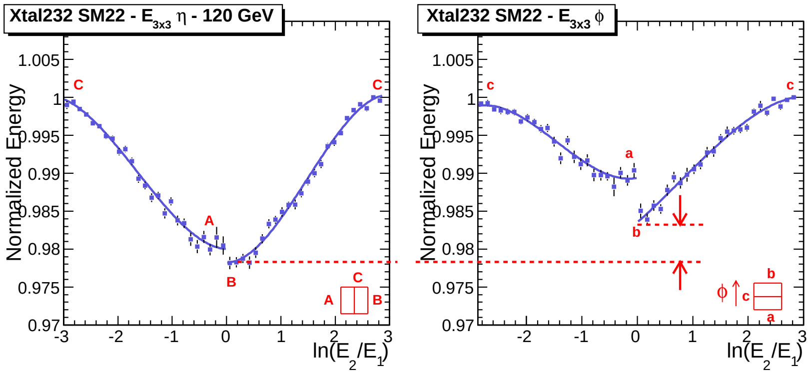

Sq'hma 3.5: *Normalized energy vs.* $\ln(E_2/E_1)$ *on one crystal: Asymmetry between* η *and* ϕ *direction. (Energy summed on* 3×3 *crystals; left:* η*, right:* ϕ*.) The schematic index shows the correspondence between* $\ln(E_2/E_1)$ *and the crystals' surface.* $A(a)$ *and* $B(b)$ *denote the opposite edges of the surface across the* $\eta(\phi)$ *direction, while* $C(c)$ *corresponds to its centre.* $B(b)$ *is the edge with the higher value of* $\eta(\phi)$*.*

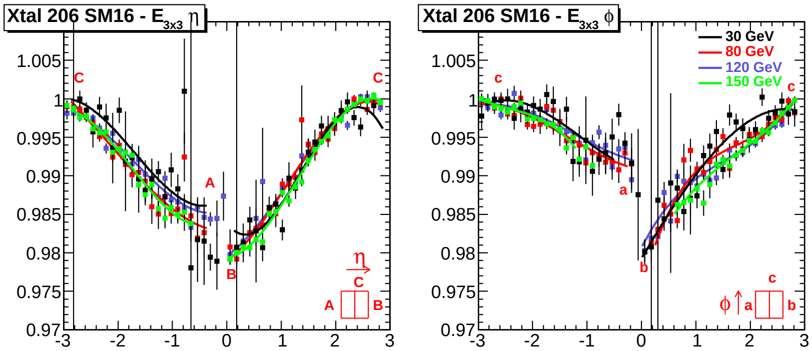

Sq'hma 3.6: *Normalized energy vs.* $\ln(E_2/E_1)$ *for various beam energies; the energy is summed on a matrix of* 3×3 *crystals. The schematic index shows the correspondence between* $\ln(E_2/E_1)$ *and the crystals' surface.* $A(a)$ *and* $B(b)$ *denote the opposite edges of the surface across the* $\eta(\phi)$ *direction, while* $C(c)$ *corresponds to its centre.* $B(b)$ *is the edge with the higher value of* $\eta(\phi)$*.*

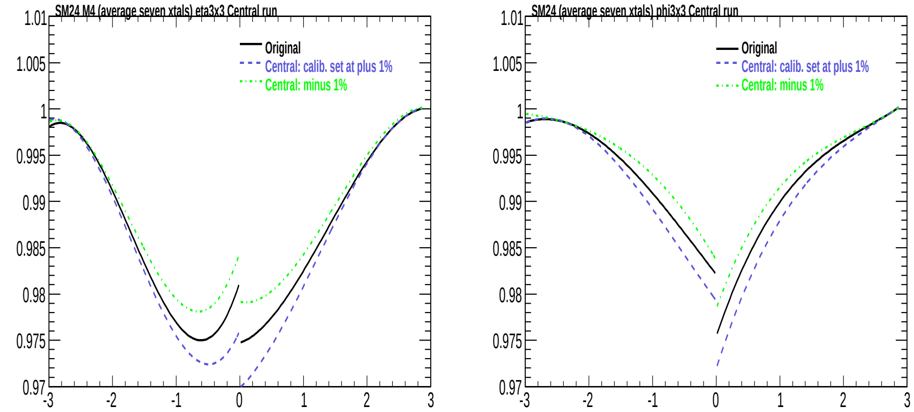

Sq’hma 3.7: *Averaged normalized energy vs.* $\ln(E_2/E_1)$ *across* η *(left) and* ϕ *(right), for 7 crystals, after changing individually their intercalibration coefficients by* $\pm 1\%$*. Similar results are obtained after changing by* $\pm 1\%$ *the intercalibration coefficients of two or three of their immediate neighbours.*

rent modules, but the containment can fluctuate between *individual* crystals in any module, within the overall observed range (Table 3.1). However, it was found that this crystal-by-crystal fluctuation, as well as its different behaviour across the two directions, can be reproduced by varying the intercalibration coefficients of either the hit crystal or its immediate neighbours by up to 1% (Figure 3.7)

Taking all of these characteristics into consideration, four sets of correction functions, one corresponding to each module, were produced by averaging several crystals belonging to the same modules and supermodules.

3.2.5 Tests of the correction functions

The sets of corrections have been applied on a number of crystals, belonging to either the corresponding or to different modules (as mentioned above, the supermodule from which the corrections were calculated is irrelevant). The examined crystals are left with a residual loss with a maximum close to the edges, ranging from $\sim 0.3\%$ to $\sim 1\%$.

In addition, the effect of the containment corrections on the energy resolution has been studied. As an example, in Figure 3.8 the energy resolution obtained for a crystal, after applying the set of corrections from the same module of another supermodule, is compared to the resolution obtained when using direct position information from the hodoscopes, and to the resolution after correcting the residual error for this specific crystal.

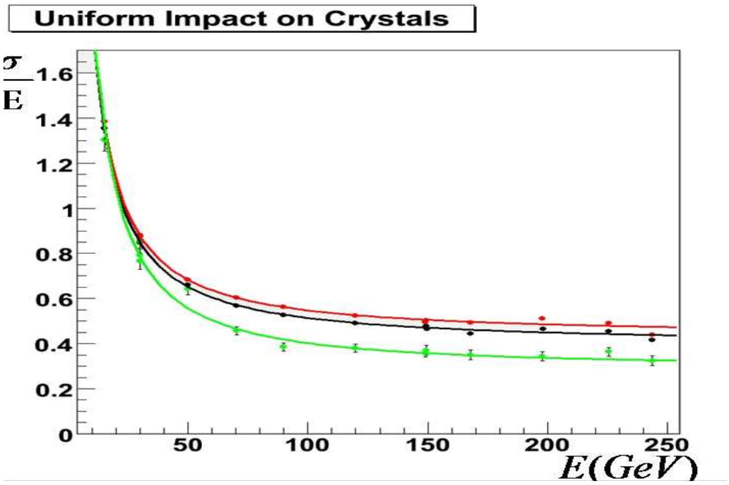

Sq'hma 3.8: *Energy resolution for one crystal using the position information from the hodoscopes (bottom), after applying one of the sets of produced correction functions (top), and after additionally correcting for the crystal's residual error (middle).*

3.3 Electron position resolution with the preshower detector

The studies of electron and photon position measurement in CMS are based on the information obtained from the electromagnetic calorimeter (ECAL) in both the barrel and endcaps regions. In the endcaps region, the position resolution could potentially be improved by taking advantage of the finer granularity of the preshower (ES) detector. (A description of ECAL and ES is found in §2.2.4, Figures 2.3, 2.4.)

In order to compare the performance of the two detectors in the position measurement, the geometrical matching between the electron position in ECAL/ES and the corresponding track in the tracker detector is used. Both the (η, ϕ) coordinates, in which ECAL is designed to operate, and the Cartesian coordinates, in which ES is designed to operate, are checked.

3.3.1 Event selection

The analysis[38] was performed on a dataset of events with electrons from Z^0 decays, produced under the official CMS simulation schedule in 2007[39]. The events were selected by single and double electron triggers. Only electrons reaching the endcaps region covered by both the tracker and the ES ($1.65 < |\eta| < 2.5$) and having transverse momenta $p_T^e > 20\,\mathrm{GeV/c}$ were considered.
Isolation criteria based on information from the tracker detector (§2.2.3) were imposed: The sum of transverse momenta of tracks with $p_T^{track} > 1.5\,\mathrm{GeV/c}$ inside a hollow cone of $0.02 < \Delta R < 0.3$ around the electron's direction was used ($\Delta R \equiv \sqrt{\Delta\eta^2 + \Delta\phi^2}$, with η: pseudorapidity, ϕ: azimuthal angle). Electrons were considered to be isolated when the ratio of the sum of p_T^{track} over the electron's p_T^e was smaller than 0.01 (Figure 3.9).

3.3.2 Clustering and position measurement

The clustering algorithm for ES was optimized for the ECAL endcaps clustering algorithm which was in use when this analysis was performed (the current ECAL clustering is described in §3.1). Each of the clusters at the ECAL endcaps ("EE") is assigned ES clusters by extrapolation of its barycentre towards the nominal interaction vertex, and a subsequent search performed around the intersection point on each of the ES planes. The search runs on ±15 strips around the intersection point and on the corresponding rows of strips in the sensors directly above and below it. The ES clusters are formed by the most energetic strips along with the ±2 neighbouring ones on the same row. A maximum of 4 ES clusters is allowed for each EE basic cluster.
The energy deposited in each of the ES clusters which correspond to a single EE cluster is shown in Figure 3.10.

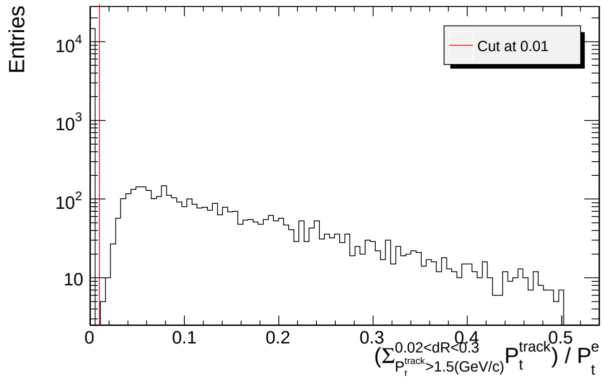

Sq'hma 3.9: *Tracker isolation for simulated electrons from Z^0 decay.*

For both the cases of individual ES clusters and energy-weighted groups of ES clusters, each ES layer provided two-dimensional points, $(X_x,\, Z_x)$ and $(Y_y,\, Z_y)$, which could be combined to provide three-dimensional points:
X-plane: $(X_x,\, Y'_x,\, Z_x) = (X_x,\, \frac{Y_y}{Z_y} * Z_x, Z_x)$
Y-plane: $(X'_y,\, Y_y,\, Z_y) = (\frac{X_x}{Z_x} * Z_y,\, Y_y, Z_y)$
The two points are equivalent; in all of the following, the value of the $\phi\,(\eta)$ coordinate was arbitrarily chosen to be read from the point formed on the $X\,(Y)$ plane. The z coordinates were set to the default values for each ES plane used in the production of the samples, namely $|Z_x| = 303.215\,\text{cm}$, $|Z_y| = 307.185\,\text{cm}$. For $|X_x|$ and $|Y_y|$ the maximum spatial error is corresponding to a minimum ionizing particle, as derived from the pitch between the silicon strips $(1.9/\sqrt{12}\,\text{mm})$.

3.3.3 Comparison in geometrical matching with track

Determination of the matching variables in η, ϕ coordinates

Two of the variables ("inner") used in the identification and selection of electrons concern the geometrical matching between the ECAL and tracker detectors. These variables measure the difference between the energy-weighted position of the EE supercluster, $(\eta^{EE}_{SC}, \phi^{EE}_{SC})$, and the extrapolation from the innermost track point up to the EE $(\eta^{extr}_{trk\_in}, \phi^{extr}_{trk\_in})$:

$$\Delta\eta^{EE}_{in} = \eta^{EE}_{SC} - \eta^{extr}_{trk\_in}, \;\; \Delta\phi^{EE}_{in} = \phi^{EE}_{SC} - \phi^{extr}_{trk\_in}$$

In the case of $\Delta\eta^{EE}_{in}$ the extrapolation is a simple projection from the innermost track point up to EE. In the case of $\Delta\phi^{EE}_{in}$ the propagation is performed using a helix, up to a distance of $\sim 4\,\text{cm}$ inside the crystals in order to compensate for the electrons' showering; more precisely, the approximation for a slightly curved helix

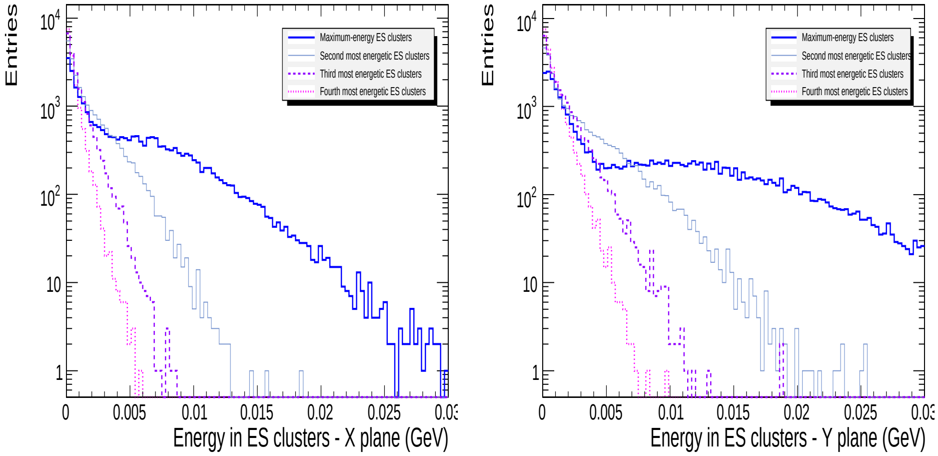

Sq’hma 3.10: *Energy deposited in individual ES X-plane (left) and Y-plane (right) clusters: maximum-energy cluster (solid thick), second most energetic (solid thin), third most energetic (dashed) and fourth most energetic (dotted).*

segment is used (*i.e.* the radius at the detector is much larger than the radius at the start of the track[40]).
Another relevant pair of geometrical variables (“outer”) is given by the matching between the position of the electron seed-cluster on EE ($\eta^{EE}_{seed}, \phi^{EE}_{seed}$) and the extrapolation of the track from the outermost track point up to the EE ($\eta^{extr}_{trk\_out}, \phi^{extr}_{trk\_out}$):

$$\Delta\eta^{EE}_{out} = \eta^{EE}_{seed} - \eta^{extr}_{trk\_out}, \;\; \Delta\phi^{EE}_{out} = \phi^{EE}_{seed} - \phi^{extr}_{trk\_out}$$

The variable $\Delta\phi^{EE}_{out}$ is used in the identification of electrons least affected by bremsstrahlung emission. However, in this analysis the “outer” variables can serve as a better measure of the position resolution (with respect to the “inner” ones), since the distance between the ES detector and the outermost tracker hit is small, so the outermost hit provides a good estimation of the electron’s position.

In the present analysis, position information from the ES was used as well for the determination of the geometrical matching variables mentioned above. Because of the differences in the two subdetectors’ structure, the calculation of the variables needed to be performed in a way different than in the EE case. The differences in the calculation are:

- The EE cluster which received the largest amount of energy is considered; the coordinates of only the ES cluster with the largest amount of received energy, among the ES clusters corresponding to that specific EE cluster, were used. (Instead of the energy-weighted position of all the clusters, which is used in ECAL).

This choice was found to perform better, and the reason is related to the bremsstrahlung radiation: Electrons with small bremsstrahlung losses result in more "focused" depositions of energy, and in that case the ES finer granularity provides a better measurement than ECAL. The ES behaviour according to the bremsstrahlung fraction is discussed in more detail below.

- In the case of $\Delta\phi_{in}$, the helix propagation starts from the track vertex (instead of the innermost track point).
  The observed improvement with this choice was a result of the algorithmic treatment of the electron's momentum at the track vertex (and not so much a result of the different spatial start of the track extrapolation, even though this also became more accurate). More specifically, the electron's momentum at each layer of the tracker detector is reconstructed according to a Gaussian Sum Filter of components (§3.1, [34]), and the difference in results was related to using the mode of the Gaussian components (instead of their mean value).
  The ES measurement was sensitive to this effect because of its finer granularity, and this modification was subsequently applied to the ECAL reconstruction software as well.

Comparison in η, ϕ

The $\Delta\eta_{in}$ distribution (Figures 3.11) as obtained from the ES (solid line) showed a prominent improvement with respect to the EE (dashed line). For the $\Delta\phi_{in}$ distribution the ES offered only a slight improvement (Figures 3.11). This can be explained by the sensitivity of the $\Delta\phi_{in}$ variable to bremsstrahlung emission from electrons inside the tracker: ES is expected to be more accurate than EE in the case of electrons with low or moderate bremsstrahlung, while it would be less accurate in the case of large bremsstrahlung, when the supercluster of EE crystals is developed to gather the spread energy of the photons more effectively. This effect is made clear in Figures 3.12, where $\Delta\phi_{in}$ was evaluated for three different groups of electrons for each detector separately. Electrons were classified according to their value of the "bremsstrahlung function":

$$f_{brem} = (P_{in\_trk} - P_{out\_trk})/P_{in\_trk}$$

where P_{in_trk}, P_{out_trk} is the momentum at the innermost and outermost track measurement respectively.
The distributions of the outer variables, $\Delta\eta_{out}$ and $\Delta\phi_{out}$, as obtained from the ES, show a clear improvement with respect to the EE (Figures 3.13). As mentioned, these variables provide a better measure of the accuracy of the position measurement, because of the proximity of the EE/ES to the pixel outermost hit.

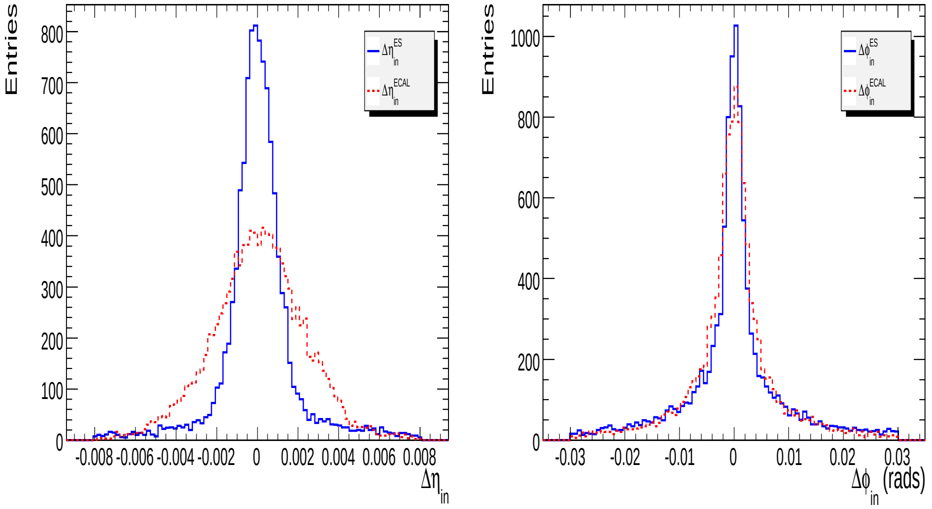

Sq'hma 3.11: $\Delta\eta_{in}$ *(left) and* $\Delta\phi_{in}$ *(right) from ES (solid line) and EE (dashed).*

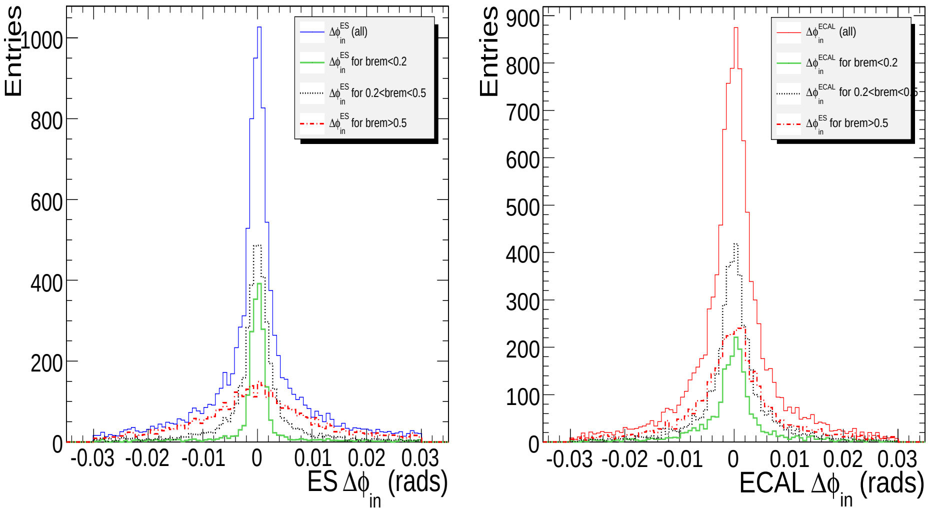

Sq'hma 3.12: $\Delta\phi_{in}$ *from ES (left) and EE (right), broken down for electrons with bremsstrahlung fraction smaller than* 0.2 *(thin solid line), between* 0.2 *and* 0.5 *(dotted), and larger than* 0.5 *(dashed).*

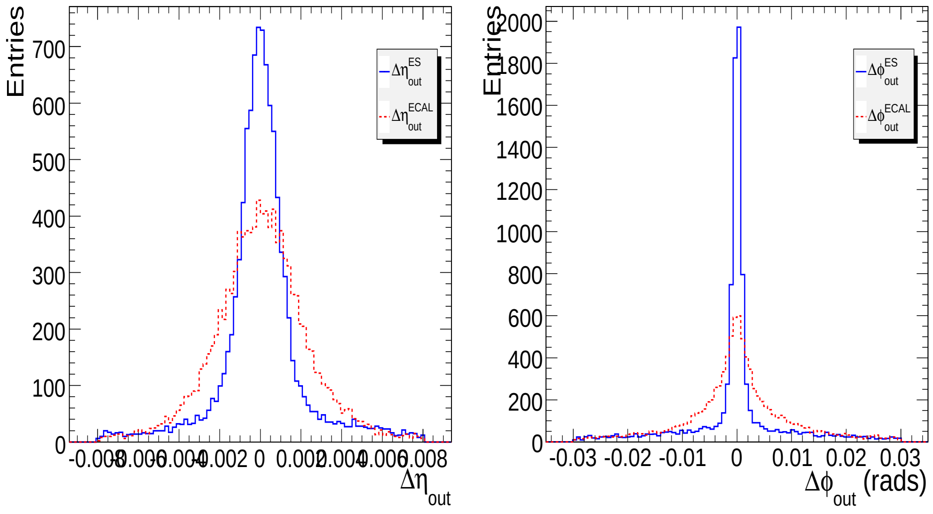

Sq'hma 3.13: *$\Delta\eta_{out}$ (left) and $\Delta\phi_{out}$ (right) from ES (solid line) and EE (dashed).*

Determination of the matching variables in cartesian coordinates

As ES is designed to give optimum position measurement in cartesian coordinates, the analysis was repeated with a geometrical matching in x, y. This required the development of dedicated functions to complement the official reconstruction software, for the extrapolation of the electron tracks. A number of differences arose in their implementation with respect to the matching variables in η, ϕ:

- The full helix formula was used (instead of the approximation of the helix segment).
- The trajectory was allowed to extrapolate up to a plane created with the appropriate z value (instead of extrapolating up to a specific point).
- Optimizing the existing algorithm, the beginning of the coordinates was placed at the interaction vertex (instead of the calculated track vertex).

The new sets of functions were found to agree with the previous ones within less than 10^{-4} rad in ϕ, and were used for the geometrical matching by forming the $\Delta x_{in}^{EE(ES)}$, $\Delta x_{out}^{EE(ES)}$ and $\Delta y_{in}^{EE(ES)}$ and $\Delta y_{out}^{EE(ES)}$variables, according to the respective quantities in η, ϕ described at the beginning of this paragraph.

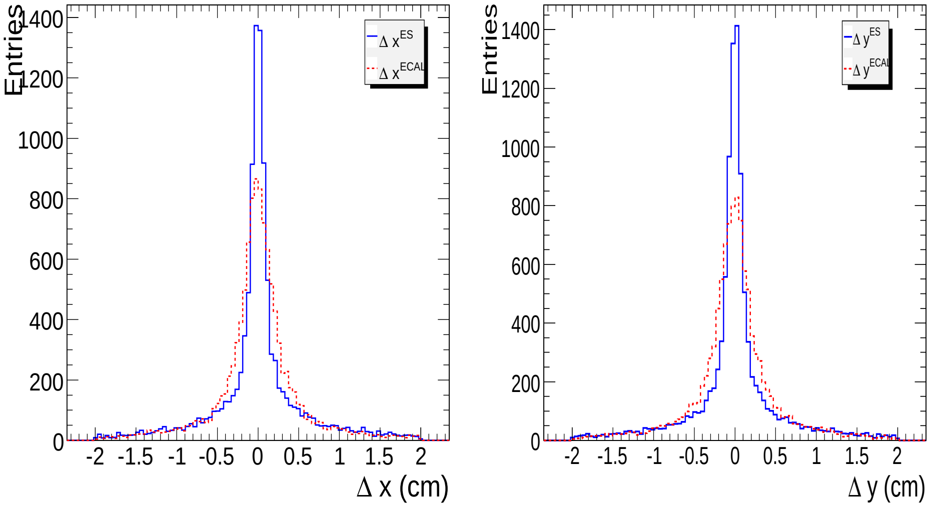

Sq’hma 3.14: Δx_{in} *(left) and* Δy_{in} *(right) from ES (solid line) and EE (dashed).*

Comparison in cartesian coordinates

Figure 3.14 shows the values of Δx_{in}, Δy_{in} achieved by ES and EE. Figure 3.15 shows the “effective sigma”[1] and the “effective two-sigma” of Δx_{in} for the two detectors. For comparison, the values for the Δx_{out} from ES are also presented, *i.e.* for the matching between the x measurement and the extrapolation from the outermost track point. ES is found to have better resolution than EE within one effective sigma but not within two sigma, where the resolution is dominated by the high-bremsstrahlung events.

Indeed, in Figure 3.16 the last plot is broken down to electrons with low (< 0.2) bremsstrahlung and medium / high bremsstrahlung, according to their value of the “bremsstrahlung function” described above. In some cases high-bremsstrahlung events were found to correspond to unusually large values of Δx_{out}, as a result of the endcaps clustering algorithm. (The algorithm currently in use for ECAL clustering is discussed in §3.1).

3.3.4 Conclusions

The position resolution for electrons from Z^0 decays when using the measurement from the ES detector is improved with respect to the EE, as seen from the $\Delta\eta, \phi_{out}$ variables. In addition, the electron identification variable $\Delta\eta_{in}$ is also

---

[1] “Effective sigma” refers to that width away from the mean within which 68.3% of a distribution’s values fall.

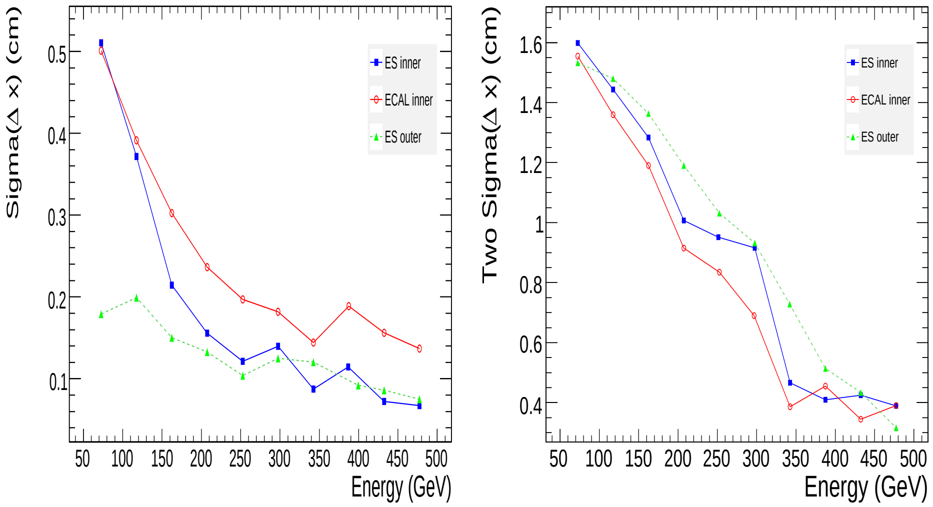

Sq’hma 3.15: *“Effective sigma” (left) and “effective two-sigma” (right) of* Δx_{in} *from ES (squares) and EE (circles).* Δx_{out} *from ES is also plotted (triangles).*

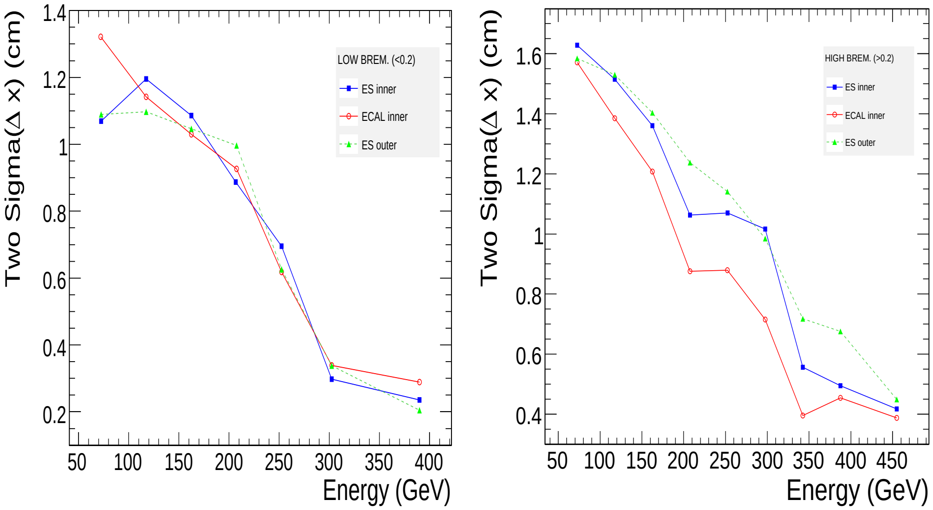

Sq’hma 3.16: *“Effective two-sigma” of* Δx_{in} *from ES (squares) and EE (circles), and* Δx_{out} *from ES (triangles), for values of bremsstrahlung function* < 0.2 *(left) and* > 0.2 *(right).*

improved significantly, while ES performs better in $\Delta\phi_{in}$ for electrons with low bremsstrahlung losses. It was found in general that for electrons with low bremsstrahlung fraction ES is superior, while in the opposite case ECAL performs better at collecting all the spread radiation.

3.4 Electromagnetic objects in the Particle Flow algorithm

In addition to the standard reconstruction of objects in CMS, the Particle Flow ("PF") algorithm was developed, following the practice of previous collider experiments, and is used in an increasing number of physics analyses. This section gives an overview of the reconstruction of electrons and photons in PF, and of the study of the relevant commissioning of the preshower detector (ES) with LHC data.

The main characteristic of the PF algorithm is that the reconstruction of every object in the event occurs from a common set of measurements; therefore, in order to describe the reconstruction of photons, the reconstruction for all kinds of particles has to be overviewed in parallel. This is discussed in a qualitative manner in §3.4.1, along with an introduction to the general principles of the PF algorithm.
The reconstruction of electrons follows in more detail in §3.4.2.
Finally, the commissioning of the ES detector in the PF algorithm with photons from the first LHC collisions in 2009 is presented in paragraph §3.4.3.

3.4.1 Overview of the Particle Flow algorithm - Photon reconstruction

The aim of the PF algorithm[41][42] is to reconstruct and identify all stable particles in each event, through a combination of all CMS subdetectors. A list of individual particles is thus created and subsequently used for the reconstruction of the event, *inter alia,* in building hadronic jets, tagging b and τ jets, determining the missing transverse energy, quantifying the isolation of particles.

Building of PF blocks

The logic permeating the PF algorithm is treating the subdetectors' measurements as "building elements", and creating "blocks" by linking spatially the elements in an appropriate manner. In the end, each block will constitute a particle.
More specifically, the "building elements" include tracks formed in the tracker detector, clustered energy measurements in the calorimeters, and tracks in the muon system.
The topological linking of the elements proceeds in-out, allowing the PF reconstruction to take advantage of the position resolution of the tracker detector. However, a very accurate reconstruction of tracks is required in order to make this approach meaningful. Therefore, a special iterative algorithm was developed, involving the removal of the used hits at each step while at the same time loosening the constraints on the track seeding.

The clustering algorithm for the calorimeters and the ES detector consists of three steps: First, "cluster seeds" are identified as energy measurements larger than that of their immediate neighbours and above a given energy. Second, "topological clusters" are grown from the seeds by aggregating cells with at least one side in common with a cell already in the cluster and with an energy in excess of a given threshold (in the ECAL and ES, these thresholds represent two standard deviations of the electronics noise). Finally, the energy of each cell is shared to all clusters according to the cell-cluster distance (assuming Gaussian shower shapes), and the determination of the cluster energies and positions is recalculated. The calculation is iterated until convergence is reached.

After the elements are built, they are connected with the linking algorithm to form blocks, which are then the inputs to the particle reconstruction and identification. Each block typically contains up to three elements, with the smallness of the blocks ensuring the persistance of the algorithm performance, regardless of the event complexity. The linking is performed between (i) tracker tracks and ES/ECAL/HCAL clusters, (ii) between ES/ECAL clusters and ECAL/HCAL clusters respectively, (iii) between tracker tracks and tracks in the muon system. In the first two cases, in order to establish a link the extrapolated position from the innermost detector element has to fall within the boundaries of a cluster. The cluster envelope can be enlarged by up to the size of one cell in each direction to account for the presence of gaps between calorimeter cells, cracks between calorimeter modules, the effect of multiple scattering for low-momentum charged particles, and the uncertainty on the position of the shower maximum (the extrapolation is performed at a depth corresponding to the expected maximum of a typical longitudinal electron shower profile in ECAL and at a depth corresponding to one interaction length in HCAL). The link distance is defined as the distance in the (η, ϕ) plane between the extrapolated position and the cluster position. In the third case, a link between a track in the tracker and a track in the muon system is established when a global fit between the two tracks returns an acceptable χ^2 value. When several tracker tracks can be fit with a given muon track, only the link that returns the smallest χ^2 is retained.

The link between ES and ECAL clusters is studied in more detail in §3.4.3.

Object reconstruction

After the collection of blocks is assembled for each event, the reconstruction of objects takes place.

Muons are the first to be formed, from linked tracks in the tracker and the muon system, if the momentum of the combined track is consistent with that from the tracker. The corresponding track is subsequently removed from the block, and the expected energy depositions in the calorimeters are subtracted from the corresponding clusters.

Next, electrons are formed from tracks and linked ECAL clusters, including those coming from bremsstrahlung photons, and the corresponding elements are removed from the block. (The reconstruction and identification of PF electrons is discussed in more detail in §3.4.2.)

Before proceeding, the linking between the tracker and the calorimeters is revisited. If more than one tracks are linked to a HCAL cluster, their momenta are summed. If more than one tracks are linked to an ECAL cluster, only the closest one is kept. If, however, a track is linked to more than one ECAL clusters, the closest cluster is kept and a decision must be taken about whether the rest of the links are kept or rejected: The linked ECAL clusters are ordered according to their distance from the track, and added increasingly to the measured HCAL energy; as long as the sum of energy is smaller than the track momentum, the links are kept. (This choice is related to the presence of photons, where there are not any real links, and the presence of hadrons, where the links should be preserved.)
If the total calorimetric energy is still smaller than the track momentum, then the search for muons is repeated with relaxed criteria. The remaining elements and blocks are used for the reconstruction of hadrons and photons.

Each track gives rise to a charged hadron, and the relevant elements are removed from the block.
In addition, the cases where the calorimetric (ECAL+HCAL) energy of only the closest clusters to the track is larger than the track momentum are examined further: If that energy is larger than the total energy collected in the ECAL, then the energy in the ECAL gives rise to a photon, and the remaining excess (with respect to the track momentum) gives rise to a neutral hadron; otherwise, the excess gives rise to a photon.
After all the tracks and the corresponding calorimetric clusters are removed, the remaining clusters give rise either to photons, if they had never been linked to a track, or to neutral hadrons, if they had links which were then disabled.

3.4.2 Electron reconstruction

Track building

Tracking is considered to be the cornerstone of the PF algorithm in CMS, since the granularity of the tracker detector is superior to the other detectors', and since PF aims at reconstructing all individual particles of an event, even if belonging to hadronic jets.
The tracking and pre-identification of electrons is based on an iterative strategy, as hits unambiguously assigned to tracks get removed and the remaining ones are refitted, with progressively looser criteria.

The first step of the tracking is identifying "seed tracks", *i.e.* tracker hits belonging to track candidates, which will be considered for the full application of the tracking algorithm.

One track-seeding method relies on tracks reconstructed with the Kalman Filter (KF) algorithm, as the Gaussian Sum Filter method[34] proves too CPU-intensive for this step. Although less precise than the GSF algorithm for the description of radiative losses, KF is capable of reconstructing accurately tracks with negligible bremsstrahlung emission.
Each KF track is extrapolated up to ECAL; if it is matched with a topological cluster both spatially (§3.4.1) and in momentum-energy, it is selected for further consideration. Otherwise, a "light" GSF refit is performed, using a smaller number of gaussian components than usual, and the track is passed through a multivariate analysis using a Boosted Decision Tree; the input for this selection uses the number of tracker hits, the energy loss in the track, the quality of fit from both fitting algorithms, and the matching with ECAL. If the track does not satisfy the selection, the track is no longer considered for electron reconstruction. (At this step, the electron candidate sample is still dominated by pions faking electrons.)
A second track-seeding strategy proceeds inwardly, by starting from the ECAL topological cluster and selecting the tracker hits compatible with a track, under both charge hypotheses.

Eventually, the track-seeds from both strategies are merged in a common collection, and the GSF fitting algorithm is used for the building of tracks. The emerging tracks are used both within the PF framework and the official CMS reconstruction framework.

However, before proceeding with the electron reconstruction, a cleaning of the tracks is needed to ensure there is no duplication because of bremsstrahlung photon conversions.
The cleaning strategy is applied only to pairs of GSF tracks which have a distance $|\Delta\eta| < 0.05$ and $|\Delta\phi| < 0.3\,\text{rad}$ between them, since this is the commonest case for conversion legs.
If one or both the tracks have a distance of more than 5 cm between their innermost tracker hit and the beam line, then the one with the smallest distance is considered to be the primary track. Otherwise, if both tracks were seeded from ECAL topological clusters, then the one with momentum matching better the topological cluster's energy is considered to be the primary one. If at least one of the tracks was seeded from the tracker, then two criteria are applied sequentially: The reconstructed charge has to be the same at the vertex and at the outermost tracker hit; and if the tracks share at least 50% of the hits then the one with most hits is considered as the primary, unless they have the same number of hits, when the one with the best χ^2 fit is selected.

Bremsstrahlung recovery - Clusters association

In the next step, an identification of the potential bremsstrahlung clusters is carried out. For each tracker layer, bremsstrahlung emission is sought by extra-

polating a straight line, tangential to the direction of the GSF track, up to the ECAL. If an ECAL cluster, not already linked to another track, can be linked to the straight line then its energy is assigned to the total electron energy.
Finally, in order to assign correctly the electron cluster to the GSF track, and also deal with late bremsstrahlung emission, a special treatment is used: After linking a cluster to the GSF track, all clusters which belong to the same topological cluster (§3.4.1), within a distance $|\Delta\eta| < 0.05$ from the track, and not linked to any other KF track, are considered. The cluster closest to the GSF track extrapolation is considered to be the electron cluster, while any other clusters are simply added to the list of clusters connected to the GSF track.
When the list of the ECAL clusters associated to the GSF track is defined, the ES clusters associated to them and the HCAL cluster linked to the GSF track, if any, are stored in the list of the electron identification elements. All the ECAL clusters connected to the GSF track and to its tangents form one PF ECAL supercluster.

Electron identification

In the last step of electron selection, variables from the three involved detectors are input in a discriminator using a multivariate Boosted Decision Tree (BDT). These variables are:

- Tracker - ECAL matching observables:
  - fraction of energy in ECAL over momentum at outermost tracker hit, E_{ECAL}/p_{out},
  - ratio between bremsstrahlung as measured by ECAL and tracker, $\sum \frac{E_\gamma}{p_{in}-p_{out}}$,
  - total ECAL energy over innermost track momentum, $\frac{E_{ECAL}+\sum E_\gamma}{p_{in}}$ (where $\sum E_\gamma$ is the energy associated with bremsstrahlung),
  - matching in pseudorapidity, $|\eta_{GSF} - \eta_{ECAL}|$,
  - appropriate cluster-extrapolation matching, for determining the presence of early (in the first three tracker layers) and late bremsstrahlung are taken into account, as they cause bias in the ECAL-tracker matching.
- Calorimetric observables:
  - lateral shower shape variable, $\sigma_{\eta\eta}$,
  - hadron fraction of the shower energy, $H/(H + E_{ECAL})$.
- Tracking observables:
  - "bremsstrahlung fraction", $f_{brem} = \frac{p_{in}-p_{out}}{p_{in}}$,
  - number of reconstructed hits and χ^2 value of KF tracks,
  - η, p_T, χ^2 value, and momentum resolution $(\frac{\sigma_{p_T}}{p_T})$ of GSF tracks.

3.4.3 Preshower commissioning in the Particle Flow algorithm

As described in §3.4.1, the “building ingredients” of the PF algorithm are tracks, energy clusters, and the links between them. The links play a major role in the reconstruction algorithm, as they define the “blocks” from which the particles are inferred, and missing links could result in the creation of additional particles and therefore in double counting of energy in the event. In the analysis presented here, the linking between the ECAL and ES detectors was tested with photons from the first LHC collisions, at $\sqrt{s} = 900\,\mathrm{GeV}$[42].
The used simulated datasets came from the official CMS simulation of summer 2009. Events from both collisions and simulation were selected without any requirement other than having a good fraction of high-quality tracks.

Most electromagnetic particles entering the ES start showering in the lead radiator; a small fraction of the shower energy is detected in the silicon-strip layers, and the shower develops further in the crystals of the ECAL endcap, where it is detected as an ECAL cluster (a detailed description of ECAL and ES is found in §2.2.4). The energy of both electrons and photons is obtained from the ECAL cluster energy, and from the energy detected in the two layers of the ES, in an attempt to correct for the energy lost in the lead radiator.

An example of reconstructed PF photons, with the corresponding ECAL and ES clusters, is shown in Figure3.17. In PF, an ECAL cluster is considered to be linked to a ES cluster if at least one strip in the ES cluster overlaps with at least one crystal in the ECAL cluster, in the (η, ϕ) plane (§3.4.1). As missing links could give rise to a lower performance of the electron identification in the endcaps, and to a slightly lower energy response for both electrons and photons, the procedure is checked in real data with respect to the simulation. The performance of the ECAL-ES linking procedure was investigated using photon candidates with an energy larger than 2 GeV (the threshold is applied because of limitations in the simulation production).

Figure 3.18 shows the difference between the ECAL cluster position and the position of all linked clusters in the outermost ES layers (“ES2”), along the x and y directions. Along the y direction, which is measured with high precision by the ES2 layer, the width of the distribution is dominated by the ECAL cluster width. Along the x direction, it is dominated by the ES strip length.
The fraction of the ECAL clusters linked to a number of clusters in ES1 (the innermost ES layers) and ES2 is shown in Figure 3.19. A larger number of clusters is observed in ES2, which is placed behind a larger amount of lead radiator than ES1. The agreement between data and simulation validates the ECAL-ES link procedure.

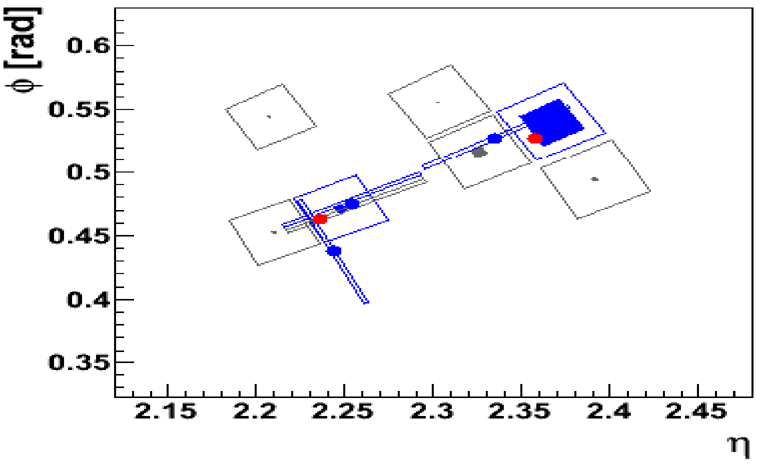

Sq'hma 3.17: *Two Particle Flow photons, reconstructed in the 2009 data from one ECAL cluster (red dots), linked to ES clusters (blue squares).*

Figure 3.20 shows the total energy deposited in ES (sum for all linked ES clusters on both planes) as a function of the energy measured in the ECAL cluster. The observed difference requires more investigation after establishing the correspondence between detector counts and minimum ionizing particles with collisions data.

It could be noted that the same study was repeated with the early data from LHC collisions at $\sqrt{s} = 7\,\text{TeV}$ with the same overall results[43].

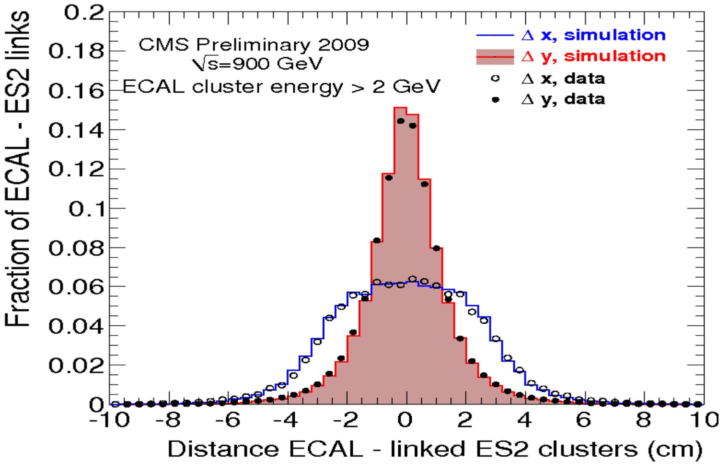

Sq'hma 3.18: *Distance between the cluster positions on ECAL and on the outermost ES plane, along the x(y) direction, for photons reconstructed in the particle flow from an ECAL cluster and at least one ES cluster. The data are shown for x(y) as hollow points (solid dots), and the simulation as an empty histogram (full histogram). The distributions are normalized to unity.*

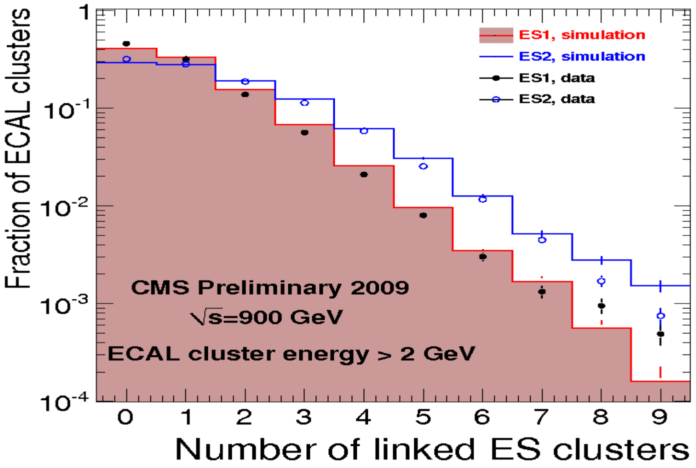

Sq'hma 3.19: *Probability of an ECAL cluster to be linked to a number of clusters in the innermost (ES1) and outermost (ES2) ES planes (data: full points; simulation: full histogram).*

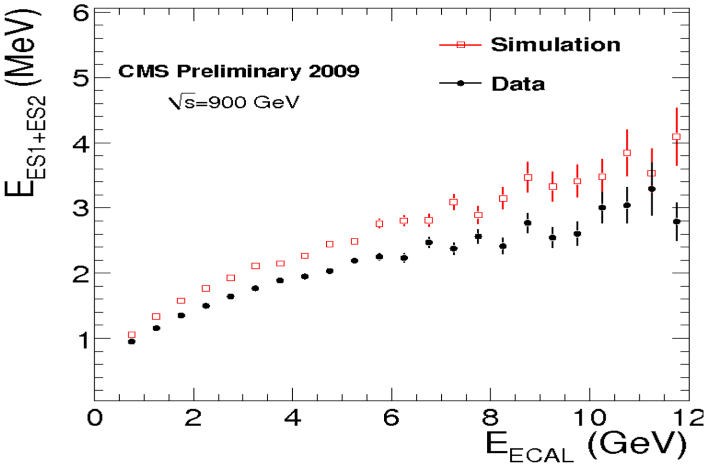

Sq'hma 3.20: *Profile of the sum of energy deposited in linked ES clusters of both planes as a function of the energy in the ECAL cluster: mean value and RMS from data (circles) and simulation (boxes).*

Κεφάλαιο 4

Search for anomalous trilinear gauge couplings in the $Z^0\gamma$ channel

This chapter describes the search for anomalous trilinear gauge couplings (aTGCs) in the $Z^0(\rightarrow l^+l^-)\gamma$ channel, performed on $\sim 36.1\%\,\mathrm{pb}^{-1}$ of LHC collisions data collected by the CMS experiment during 2010 [44][45].
It begins with the characteristics of the signal under study, and the main backgrounds to this search, in §4.1. §4.2 introduces the event generators capable of producing datasets with anomalous trilinear vertices, and gives the details of the simulation used in the analysis.
The criteria for the identification of the objects involved in the final state and the selection of events are discussed in §4.3. In addition, §4.4 introduces the data-driven method employed for estimating the main backgrounds to the signal under study. The results from the analysis on the collisions data are presented in §4.5.
Finally, the statistical analysis of the measurement is discussed in §4.6; the study is concluded with the placement of limits on the values of aTGCs.

4.1 Signal and backgrounds

4.1.1 Characteristics of the $Z^0\gamma$ final state

The final state under study is characterized by one pair of oppositely charged leptons of the same flavour, and one photon. The leptons are the decay products of a Z^0 boson. Since the process involves anomalous Trilinear Gauge Couplings (aTGCs), it occurs through the *s*-channel of Figure 4.1.
The same final state can occur within Standard Model (SM) through the t and u-channels of Figure 4.1, but, since in this case the two bosons do not originate from a common vertex, it is treated as a background to the search for anomalous

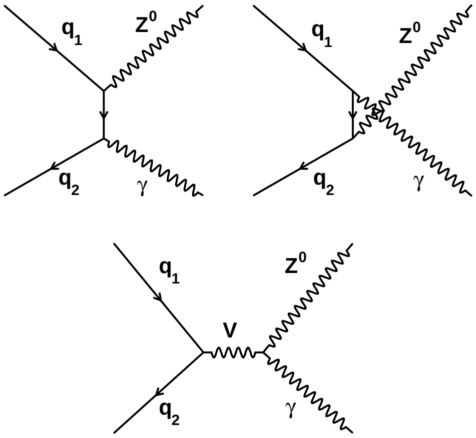

Sq'hma 4.1: *Leading order diagrams for the $Z^0\gamma$ production. The two diagrams in the first row are permitted within the Standard Model. The diagram in the second row, with $V = Z^0$ or γ, can occur if anomalous trilinear vertices exist.*

couplings. Within SM there can also be contribution from final state radiation (Figure 4.2) and emission from fermion loops, but the latter is almost negligible (lower by an order of 10^{-3} with respect to the t-channel process[7]). Different SM contributions which can mimic a $Z^0\gamma$ signal are discussed below, in the sections about reducible backgrounds (§4.1.4).

If the $Z^0\gamma$ production through the s-channel happens in nature, in the LHC it will occur from the interaction between a - most probably valence - quark, and a sea anti-quark. The mediator can be an off-shell Z^0 which radiates a photon and becomes on-shell, or, less probably, a photon which emits a Z^0 and becomes

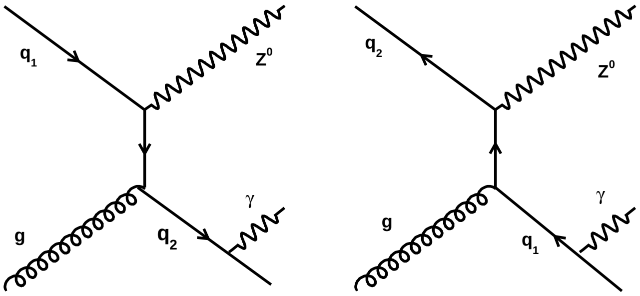

Sq'hma 4.2: *Standard Model $Z^0\gamma$ production through final state radiation.*

on-shell (Equation (1.4)).
The Z^0 can subsequently decay into leptonic modes and hadronic modes, which in the LHC are overwhelmed by the size of QCD background and thus not considered for the analysis. Other possible Z^0 decays are into pairs of neutrinos, which are not discussed in this study. In the following, the leptonic decay modes into electrons and muons are examined.
The branching ratio for the leptonic decays of Z^0 is: $3.363 \pm 0.004\%$ for electrons and $3.366 \pm 0.007\%$ for muons[46].

Although there are four possible anomalous couplings for each $Z^0\gamma V$ $(V = Z, \gamma)$ vertex (Equation (1.4)), in the following only the CP-conserving couplings h_3^V, h_4^V will be discussed for simplicity. There will be no loss of generality, since the CP-violating couplings $h_{1,2}^V$ have behaviour similar to $h_{3,4}^V$ respectively. In the following, generation-level information from the "BAUR $Z^0\gamma$" matrix element generator (§4.2.2) was used for the cross-sections and the distributions of kinematic variables; the only selection cuts applied at generation-level are:

- photon transverse energy $E_T^\gamma \geq 5\,\text{GeV}$,
- leptons' transverse momentum $p_T^{lepton} \geq 5\,\text{GeV/c}$,
- photon - lepton separation in the final state $\Delta R(l,\gamma) \geq 0.5$ (where $\Delta R(l,\gamma) \equiv \sqrt{(\Delta\phi)^2 + (\Delta\eta)^2}$, ϕ: azimuthal angle, η: pseudorapidity).

Cross-sections for the SM $Z^0\gamma$ process, for indicative values of aTGCs used in the present analysis, and for the main backgrounds, can be found in Table 4.1. The cross-sections for all simulated samples with aTGCs which were used in the analysis are gathered in Table 4.3, §4.2. The choice of values for $h_{3,4}^V$, along with the assumptions for the other new physical variables entering the calculations, are discussed in §4.6.1.

4.1.2 Signal properties - Discovery variables

Any contributions from vertices with non-zero trilinear couplings will complement the SM processes with the same final state, therefore the cross-section is expected to increase in the presence of aTGCs. The dependence of the cross-section on each coupling is bilinear. The coupling h_3^V enters the lagrangian with operators of dimension 6 [5] and gives a dependence of $\hat{s}^{3/2}$ on the centre-of-mass energy, while h_4^V has operators with dimension ≥ 8 and a dependence of $\hat{s}^{5/2}$; the result is a stronger effect of h_4^V on the cross-section and a general enhanced sensitivity at larger centre-of-mass energies.
As evident from Equation (1.4) in §1.2.2, the two trilinear vertices, $Z^0Z^0\gamma$ and $Z^0\gamma\gamma$, have in principle different contributions to the cross-section. The higher contribution comes from $Z^0Z^0\gamma$, since an off-shell Z^0 emits a massless photon rather than the other way around.

	SM	0, 0.004 $(ZZ\gamma)$	0, 0.004 $(Z\gamma\gamma)$	0.12, -0.004 $(ZZ\gamma)$	0.12, -0.004 $(Z\gamma\gamma)$
Cross-section (LO) (pb)	22.53	45.64	41.51	51.99	46.31
Expected ($36.1\,\mathrm{pb}^{-1}$)	813.33	1647.60	1498.51	1876.84	1671.79

	Z+jets	W+jets	$t\bar{t}$	QCD (e)	QCD (μ)
Cross-section (NLO) (pb)	3048	31314	157.5	$6.45 \cdot 10^{6}$	84679
Expected ($36.1\,\mathrm{pb}^{-1}$)	110032	1130435	5686	$2.3 \cdot 10^{8}$	3056912

P’inakas 4.1: *Cross sections and expected number of events at integrated luminosity of* $36.1\,\mathrm{pb}^{-1}$ *for the SM* $Z^0\gamma$ *channel, for indicative values of aTGCs, and for the datasets taken into account in the present analysis as main backgrounds to the* $Z^0\gamma$ *process. The pairs of numbers on the first row denote the values for the* h_3^V *and* h_4^V *(*$V = Z^0, \gamma$*) anomalous couplings respectively, for both possible anomalous vertices* $Z^0\gamma V$*. The exponents* $n_{3,4}$ *entering the form-factors expression (Equation* (1.6)*) are set equal to zero, as explained in* §*1.2.3. (The cross sections for all the aTGC values used in the analysis can be found in Table 4.3,* §*4.2.)*

	h_3^Z		h_4^Z		h_3^γ		h_4^γ	
LEP II ($700\,\mathrm{pb}^{-1}$) ($\Lambda = 2\,\mathrm{TeV}$)	-0.20	0.07	-0.05	0.12	-0.049	-0.008	-0.002	0.034
CDF ($5\,\mathrm{fb}^{-1}$) ($\Lambda = 1.2\,\mathrm{TeV}$)	-0.018	0.020	$-9 \cdot 10^{-4}$	$9 \cdot 10^{-4}$	-0.021	0.021	$-9 \cdot 10^{-4}$	0.001
CDF ($5\,\mathrm{fb}^{-1}$) ($\Lambda = 1.5\,\mathrm{TeV}$)	-0.017	0.016	$-6 \cdot 10^{-4}$	$5 \cdot 10^{-4}$	-0.017	0.016	$-6 \cdot 10^{-4}$	$6 \cdot 10^{-4}$
D0 ($\Lambda = 1.5\,\mathrm{TeV}$) ($1\,\mathrm{fb}^{-1}\,l$, $3.6\,\mathrm{fb}^{-1}\,\nu$)	-0.033	0.033	-0.0017	0.0017	-0.033	0.033	-0.0017	0.0017

P’inakas 4.2: *Existing lower and upper experimental limits at* $95\%CL$ *on the anomalous couplings* $h_{3,4}^V$ *(*$V = Z^0, \gamma$*), in combined electron, muon, and, for Tevatron, neutrino decay channels. For each quoted value, all other aTGCs are assumed equal to zero. The* Λ *variable is discussed in* §*1.2.3.*

The existing experimental limits on $h^V_{3,4}$ are found in Table 4.2 [47]. Their values used in the production for the present analysis are $h_3 = \{0, \pm 0.12\}$, $h_4 = \{0, \pm 0.004\}$. Further details on the production characteristics are given in §4.2.3 and §4.6.1.

The increase in the number of events in the case of aTGCs is prominent in the distribution of the photon's transverse momentum p^γ_T (Figure 4.3), starting at values larger than $\sim 100\,\mathrm{GeV/c}$ (also Figure 4.6, §4.2). Since the p^γ_T distribution is quite differentiating between aTGCs and SM, and as it also has functional dependence on the values of $h^V_{3,4}$, it serves as an excellent discovery variable, enabling likelihood fits on collisions data (§4.6).

As mentioned, the production of the off-shell boson will occur from the interaction between a sea anti-quark and, almost always, a valence quark, resulting in a boost along the incoming quark's direction. In this way the presence of anomalous couplings can have a visible effect on the invariant mass of the final three-body system and on the distributions of the leptons' transverse momenta (Figure 4.8, §4.2)[12].

The presence of anomalous couplings will also affect the helicity distribution of the lepton pair, since in the s-channel process the transverse momenta of the two final bosons will be equal. The lepton decay angles will act as projectors of the different helicity components, which in this case follow that of Z^0. As a result, the azimuthal decay angles of the leptons, ϕ^l, can be shown to correlate to the photon azimuthal angle ϕ^γ[11].

These variables can be investigated for the presence of new physics when sufficient data become available from LHC collisions. However, the p^γ_T distribution will still have an advantage in being more sensitive to non-standard couplings, since it is directly observable.

4.1.3 Irreducible backgrounds

As discussed above, the production of Z^0 and γ from a common vertex is prohibited within SM, but the same final state can occur at Born level through Z^0 production with simultaneous initial state radiation (ISR) or final state radiation (FSR) processes (Figures 4.1, 4.2). In the former, a photon is emitted off one of the interacting quarks, and in the latter it is emitted off one of the leptons from the Z^0 decay.

In principle, FSR can be either distinguished, since it is collinear with the leptons in most of the cases, or taken into account in the lepton reconstruction. On the other hand, ISR forms an irreducible background.

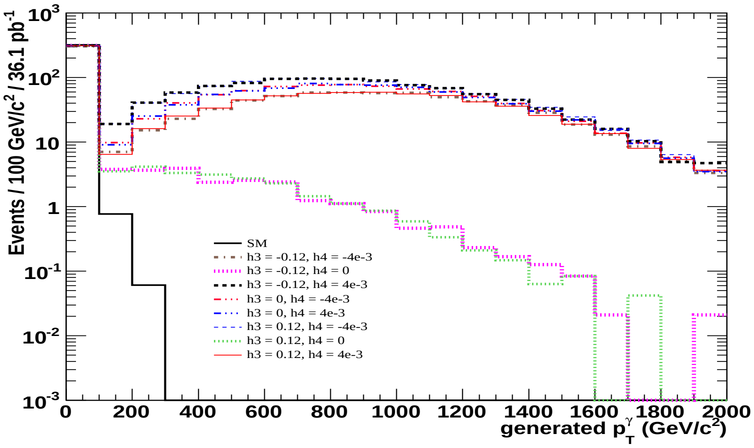

Sq'hma 4.3: *Generated transverse energy of matrix element photons in the* $Z^0\gamma$ *sample, for SM and various values of the anomalous couplings* $h_{3,4}^Z$. *Distributions are scaled to* $36.1\,\mathrm{pb}^{-1}$.

4.1.4 Reducible backgrounds

Reducible backgrounds can occur from misidentification of either the photon or one or both of the leptons. Among these backgrounds the only sizeable one is $Z^0/\gamma^* + jets$, where jets can fragment to neutral mesons and then be mistakenly reconstructed as single photons. The most effective way to deal with the part of the background which might survive the application of suitable selection cuts (§4.3.3) is to make use of data-driven methods for estimation of the remaining number of background events in the measurement (§4.4). In any case, as the momentum distribution of the neutral mesons (*e.g.* π^0, η, ρ) falls off, the probability of misidentification becomes very small at higher energies; normally it is negligible for photon transverse momenta $>\sim 100\,\mathrm{GeV/c}$.

In addition, a final state of a dilepton and a photon can occur from a variety of processes within SM, but in these cases the dilepton mass distribution is non-peaking around the Z^0 mass.

Less significant backgrounds involving misidentification are:

- $t\bar{t} \rightarrow l^+l^- + jets$, with a photon from misreconstruction,
- $pp \rightarrow W^\pm(\rightarrow l^\pm\nu_l) + jets$, involving leptons and photons from misreconstruction,
- QCD processes resulting in lepton pairs and photons, either real or from misreconstruction.

However these processes are non-peaking around the Z^0 mass and usually involve multiple misidentifications. They are easily removed by event and object selection cuts.
The cross-sections of the mentioned backgrounds are found in Table 4.1.

In conclusion, the tell-tale signature of the process under study, *i.e.* the enhanced distribution of p_T^γ, is well conspicuous with respect to SM in higher values ($>\sim 100\,\mathrm{GeV/c}$), and its observation would provide direct evidence of new physics. In low values however, which are practically the only ones accessible with $36\,\mathrm{pb}^{-1}$ of data at $\sqrt{s} = 7\,\mathrm{TeV}$ collisions, the presence of new effects can be told apart from the irreducible ISR background only by statistical fits. Therefore, the main difficulty lies in the reduction and correct estimation of the remaining background from $Z + jets$.

4.2 Event generation

This section describes the simulated datasets and the event generators used in the present analysis. The "Baur $Z^0\gamma$" matrix element generator plays a central role as it was developed specifically for the production with anomalous signals, therefore it is discussed in more detail. A description of the related production is offered along with generation-level plots of kinematic quantities.

4.2.1 CMS simulation

The simulated samples of the signal processes used in the analysis were generated with both the Baur $Z^0\gamma$ (§4.2.2) and Sherpa (§4.2.6) event generators. The background comes from the official production of the CMS experiment in fall 2010 using the MadGraph[48] and Pythia[49] generators (a discussion of the various background processes is found in §4.1.3, 4.1.4).
The events which were generated using the MadGraph matrix element generator can be examined as an example of the simulation within the CMS framework. These events have to be interfaced to Pythia for the parton showering and hadronization. MadGraph uses the CTEQ 6l1 PDF set of parton density functions, and the kT-MLM scheme for jet matching with Pythia. The rest of the simulation chain is common to all production used by the experiment: The actual interfacing to Pythia is done inside the official CMS reconstruction framework[20], using the commonly used text file format LHE (Les Houches Event)[50]. The generated events are then propagated through the full volume of the detector, and their interactions with its active and dead areas are simulated by a package based on the GEANT4 toolkit[51]. The resulting detector hits are digitized, at which step the effect of electronics noise is added, and they are finally converted into simulated output of the electronics. No pile-up events were added for the present analysis, because of the low instantaneous luminosity during the LHC operation in 2010 (maximum $\sim 2 \times 10^{32}\,\mathrm{cm}^{-2}\mathrm{s}^{-1}$).

4.2.2 The Baur $Z^0\gamma$ event generator

A dedicated implementation of the matrix element generator by U.Baur *et al.*[12] was developed for the official CMS reconstruction framework. The "Baur $Z^0\gamma$" generator[52] permits the generation of events which include the anomalous vertices $Z^0Z^0\gamma$ and $Z^0\gamma\gamma$, along with the corresponding interface to Pythia. The generator produces Born-level 3-body events ($q\bar{q} \rightarrow \gamma\, l^+l^-$) in the final state.

Originally the Baur $Z^0\gamma$ code produced weighted events, therefore an unweighting technique was used in order to pass them to Pythia for hadronization: 10 million events were created, of which the first 0.5 million were skipped in order to stabilize the generator, and the maximal weight of the following 9.5 million events was selected. This maximal weight is then used for unweighting the events, by

comparing a random number with the ratio of each event's weight to the maximum; if the random number is smaller than the ratio, then the event is selected and its weight is set to unit.
An issue which arises after the unweighting of the events is that the Baur generator sums over all initial parton states (involving up, down, strange and charm quarks), while Pythia requires one specific parton initial state. In order to choose specific initial states for the selected unweighted events, the following technique is employed: Using the 4-vector of the initial-state parton as input to the parton density function, the latter returns flavours distributed by their associated probabilities for the specific momentum slice. The initial state is selected randomly, assigning equal probabilities to all flavours.
Finally, the interface to the official CMS software reads the generated information, saved in LHE format, and passes it to Pythia for the hadronization process, which is followed by the detector simulation and the reconstruction (§4.2.1).

Comparisons have been performed in the SM production, between the Baur $Z^0\gamma$ and MadGraph generators on generation level, and between Baur and Sherpa on reconstruction level. These are found at the end of this Paragraph (§4.2.7). It should be noted that Baur and Sherpa are the only event generators which can treat anomalous vertices and which are currently available within the CMS reconstruction software.

4.2.3 Characteristics of the Baur $Z^0\gamma$ production

Although Baur $Z^0\gamma$ has the functionality of next-to-leading-order (NLO) calculations, only processes at Born level are activated for the production of the present datasets. This is done in order to have a correct matching with Pythia avoiding double counting of jets, and also because of the Baur algorithm using a narrow width approximation for the Z^0 mass at NLO, thus lacking the possibility of bremsstrahlung emission off the final leptons.
The two leptonic Z^0 decay channels, *i.e.* to electrons and muons, involving the $Z^0Z^0\gamma$ vertex, were produced separately. The following kinematic cuts were imposed:

- transverse photon energy $E_T^\gamma \geq 5\,\mathrm{GeV}$,
- transverse leptons' momentum $p_T^{lepton} \geq 5\,\mathrm{GeV/c}$,
- photon - lepton separation in the final state $\Delta R(l,\gamma) \geq 0.5$ (with $\Delta R(l,\gamma) = \sqrt{(\Delta\phi)^2 + (\Delta\eta)^2}$, ϕ: azimuthal angle, η: pseudorapidity).

Nine datasets were produced for each channel, with the anomalous couplings taking the discrete values $h_3 = \{0, \pm 0.12\}$, $h_4 = \{0, \pm 0.004\}$. No formalism with form-factors was used, *i.e.* the exponents $n_{3,4}$ in Equation (1.6) were set to zero (a more detailed discussion about this choice is found in §1.2.3). The cross-sections of the produced samples are listed in Table 4.3.

h_3^Z	-0.12	-0.12	-0.12	0	0 (SM)	0	0.12	0.12	0.12
h_4^Z	-0.004	0	0.004	-0.004	0 (SM)	0.004	-0.004	0	0.004
σ_{LO} (pb)	40.71	23.39	51.98	45.64	22.53	45.64	51.99	23.38	40.89

P'inakas 4.3: *Born-level cross-sections for the* Baur $Z^0\gamma$ *production in the* $Z^0Z^0\gamma$ *vertex, according to the values of the anomalous couplings* $h_{3,4}^Z$ *in each process.*

4.2.4 Scaling to NLO

Since the next-to-leading order (NLO) calculations are not used in the Baur $Z^0\gamma$ production, the effect of higher contributions has been taken into account by reweighting, with use of the "k-factors" method. The reweighting was applied on the distributions of the final photon transverse momentum, p_T^γ, as this is the sensitive variable used in the present search for aTGCs (§4.1.2). Since the criteria used in the event selection are quite generic and do not affect differently the leading order (LO) and NLO p_T^γ spectrum shape, there are no concerns for the use of a scaling between LO and NLO.

The two cases of initial state radiation (ISR) and final state radiation (FSR) were calculated and applied separately.

The k-factor calculation for FSR was performed using the MCFM[53] code, and is found to have a constant value of 1.2.

For the calculation of the k-factor for ISR, both the LO and NLO p_T^γ distributions were generated with Baur $Z^0\gamma$, without passing through Pythia and the rest of the simulation process (Figure 4.4). The p_T^γ-dependent k-factor is defined as the ratio of the NLO and LO differential cross-sections:

$$k = \frac{d\sigma_{NLO}/dp_T}{d\sigma_{LO}/dp_T}$$

The same criteria as for the photon selection were imposed (§4.3.3), with the additional requirement that the three-body invariant mass be $M_{ll\gamma} \geq 110\,\mathrm{GeV/c^2}$, a choice which rejects most of FSR and keeps $\sim 99\%$ of ISR events. The resulting ratio of differential cross-sections was fit with a three-order polynomial, with the addition of a flat line above 150 GeV/c (Figure 4.4).

The k-factors were calculated in the SM case and applied to all datasets. In the samples with aTGCs, the high-p_T^γ events are produced mainly through LO processes; this results in lower NLO/LO ratios with respect to SM for momenta larger than the order of a few hundreds of GeV/c (Figure 4.5). However, this difference in k-factors is compensated to some extent by the sharply falling aTGC p_T^γ spectrum (Figure 4.1, §4.1), and is taken into account by an additional systematic uncertainty of 10% in the signal modelling.

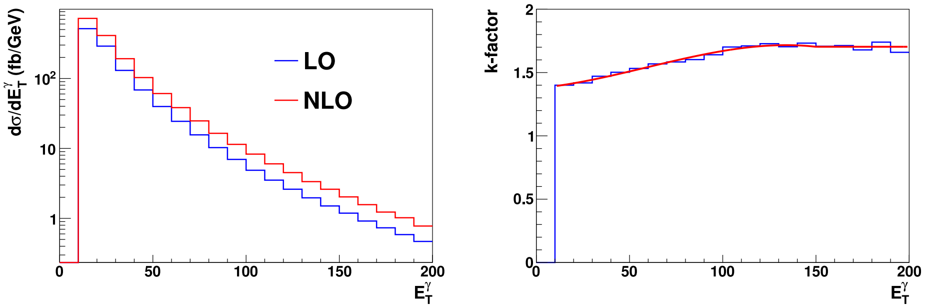

Sq’hma 4.4: *Left: Differential cross-section of the SM $Z^0\gamma$ process at NLO (upper) and LO (lower), for the photon occurring from initial state radiation, calculated with the* Baur *$Z^0\gamma$ event generator, with the kinematic cuts used in the analysis selection (§4.3.3)[45]. Right: The ratio of NLO/LO and the resulting k-factor as a function of the final photon’s transverse energy[45].*

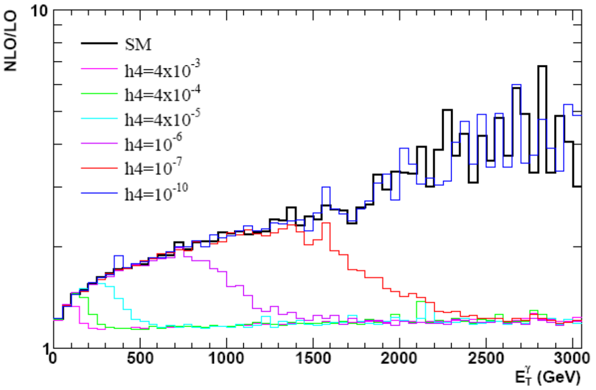

Sq’hma 4.5: *The E_T^γ-dependent k-factors, for various values of the h_4^γ coupling[45]. The events with higher E_T^γ tend to be produced in leading-order processes; therefore, using the SM k-factor could result in an overestimation of the signal in the presence of aTGC. However, this is compensated in part by the sharply falling E_T^γ distributions, and this effect is taken into account in the systematic uncertainties of the signal-modelling.*

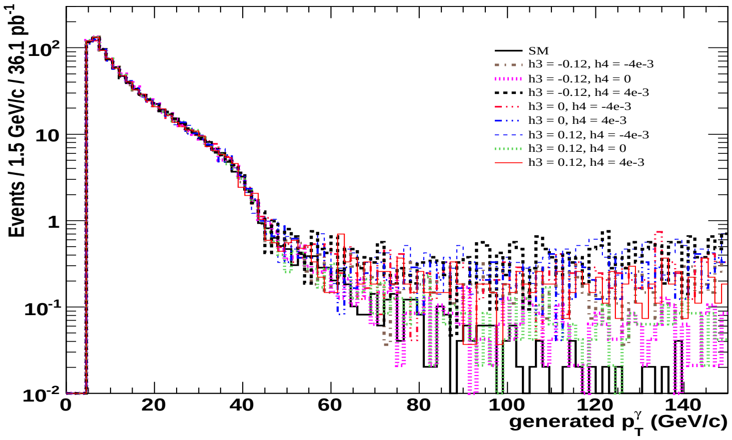

Sq’hma 4.6: *Generated transverse energy of matrix element photons in the* $Z^0\gamma$ *sample, for SM and various values of the anomalous couplings* $h^Z_{3,4}$*. Distributions are scaled to* $36.1\,pb^{-1}$*.*

4.2.5 Baur $Z^0\gamma$ production for SM signal and anomalous couplings

The generation-level distributions of kinematic quantities at LO are presented in this section. The distributions of the SM and the eight samples with aTGCs are plotted together for comparison. All results are scaled to $36.1\,\mathrm{pb}^{-1}$ to match the integrated luminosity collected by LHC in the relevant channels during the 2010 Run.

Figure 4.6 and Figure 4.7 show the transverse momentum and pseudorapidity distribution of the photon. (The transverse momentum is shown in the range of values relevant for the first LHC data; the full range of the photon transverse momentum is found in Figure 1 of §4.1.) Figure 4.8 shows the transverse momentum distribution of the muons, and Figure 4.9 shows their pseudorapidity distribution. The distributions for electrons are similar.

4.2.6 Production with the Sherpa generator

Sherpa[54] is a standalone generator which includes its own showering model and provides higher-order QCD contributions to the Born-level calculations. More specifically, in addition to the tree-level diagrams, Sherpa has the functionality of gluon emission from one of the initial-state quarks (LO process), and of bremsstrahlung emission from the final-state quark in quark-gluon interactions (process of leading-logarithm order). The relevant Feynman diagrams are found in Figures 1.4 and 1.5, §1.3.

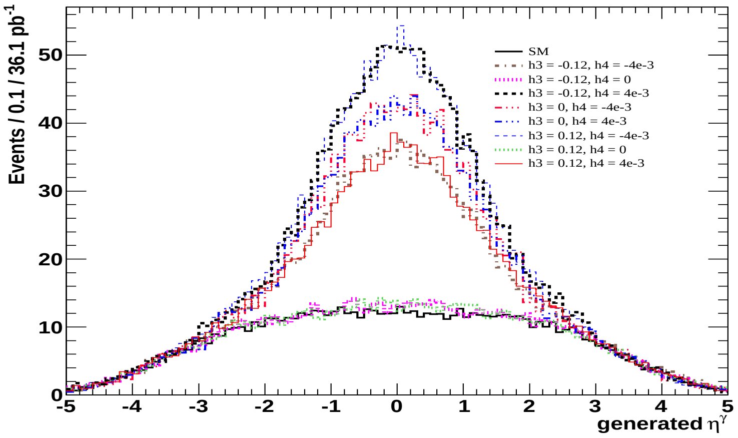

Sq'hma 4.7: *Generated pseudorapidity distribution of matrix element photons in the* $Z^0\gamma$ *sample, for SM and various values of the anomalous couplings* $h^Z_{3,4}$. *Distributions are scaled to* $36.1\,\mathrm{pb}^{-1}$.

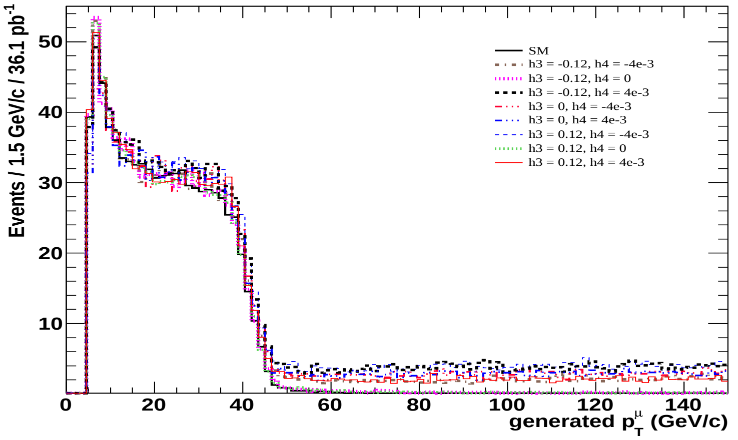

Sq'hma 4.8: *Generated transverse momentum of muons in the* $Z^0(\rightarrow \mu\mu)\gamma$ *sample, for SM and various values of the anomalous couplings* $h^Z_{3,4}$. *Distributions are scaled to* $36.1\,\mathrm{pb}^{-1}$.

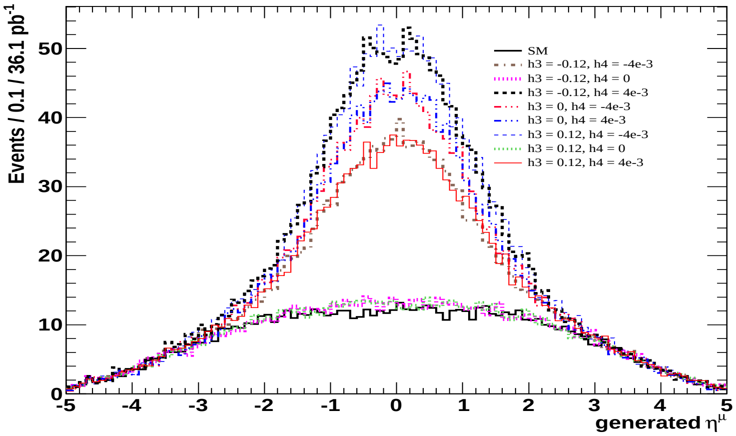

Sq'hma 4.9: *Generated pseudorapidity distribution of muons in the* $Z^0(\rightarrow \mu\mu)\gamma$ *sample, for SM and various values of the anomalous couplings* $h^Z_{3,4}$. *Distributions are scaled to* $36.1\,\mathrm{pb}^{-1}$.

Sherpa v1.2.2 was used for the production of datasets for both $Z^0\gamma V$ $(V = Z^0, \gamma)$ vertices, with the couplings taking the values $h^V_3 = \{0, \pm 0.12\}$, $h^V_4 = \{0, \pm 0.004\}$. No form-factor parameterization was used for the couplings (§1.2.3).
The kinematic cuts imposed are:

- photon transverse energy $E^{\gamma}_T > 5\,\mathrm{GeV}$,
- leptons' transverse momentum $p^{lepton}_T > 5\,\mathrm{GeV}$,
- spatial separation between the final photon and the leptons $dR(l, \gamma) > 0.5$,
- dilepton invariant mass $M_{ll} > 10\,\mathrm{GeV/c}^2$,
- jet transverse momentum $p^{jet}_T > 10\,\mathrm{GeV}$,

and for the interacting partons:

- transverse momentum $p^{parton}_T > 10\,\mathrm{GeV}$,
- spatial separation between the final photon and each parton $dR(parton, \gamma) > 0.05$
- spatial separation between partons $dR(parton, parton) > 0.001$.

In order to scale to NLO by using the k-factors derived with the Baur $Z^0\gamma$ generator, the Sherpa datasets were assumed to have only the leading-order cross-sections.

4.2.7 Comparison of generators

The SM production with the Baur generator was compared to the one with Madgraph at the generation level, and to the Sherpa production after the reconstruction.

The Madgraph[48] generator is interfaced to Pythia for the hadron showering and hadronization (§4.2.1) and includes QCD corrections. More specifically, the Madgraph production is of LO and, in contrast to Baur, can also contain up to two jets. In addition to the generation cuts described in §4.2.3, in MadGraph a minimum cut of 10 GeV/c is applied on the transverse momentum of the jets. Figure 4.10 shows comparisons in the distributions of SM photon transverse momentum, pseudorapidity, azimuth angle and spatial separation between photon and leptons. Figure 4.11 compares the maximum and minimum momentum lepton, the dilepton invariant mass, and the dilepton-plus-photon invariant mass distributions in SM. All the plots show agreement between Baur and Madgraph generation with no jets, while the Madgraph samples with up to two jets have a harder ISR photon transverse momentum spectrum. The same behaviour is also seen in the maximum transverse momentum spectrum of the leptons.

The Sherpa[54] production includes up to one jet and uses the generation cuts described in §4.2.6. Figure 4.12 show the comparison of reconstructed photon quantities in SM, with distributions of the transverse momentum, pseudorapidity, azimuth angle and spatial separation. Figure 4.13 show the comparison in the maximum and minimum transverse momentum lepton distribution, and the invariant mass of the dilepton and dilepton-plus-photon distributions. There is good overall agreement.

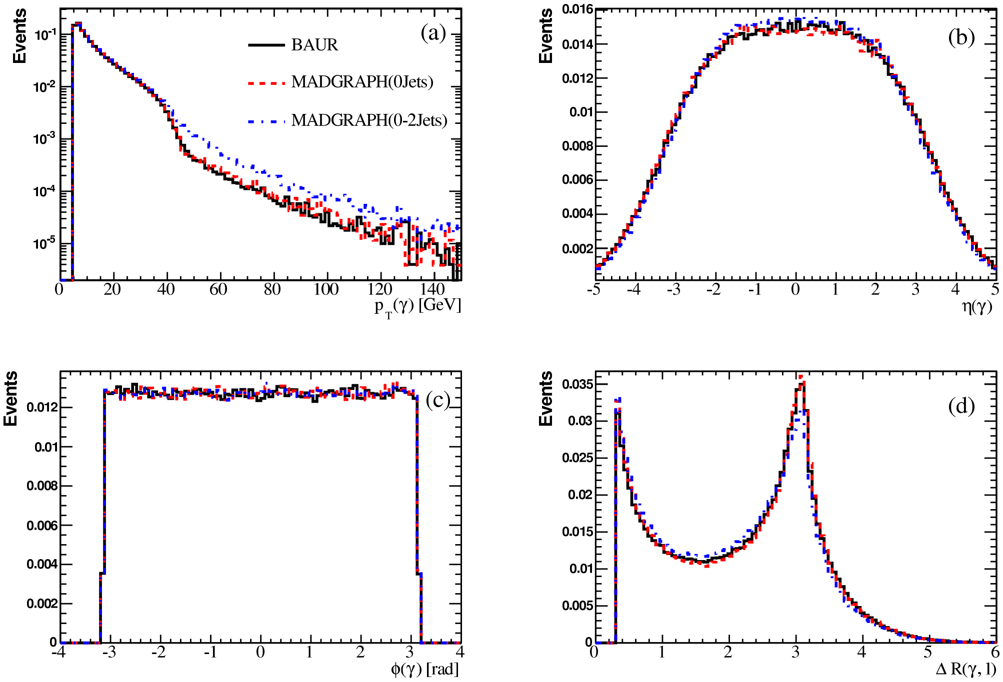

Sq’hma 4.10: *(a) Photon transverse momentum distribution in* Baur *(black solid histogram),* Madgraph *with* 0 *jets (red dashed) and* Madgraph *up to* 2 *jets (blue dot-dashed). (b) Photon* η *distribution, (c) Photon* ϕ *distribution. (d) Photon spatial separation from the leptons.*

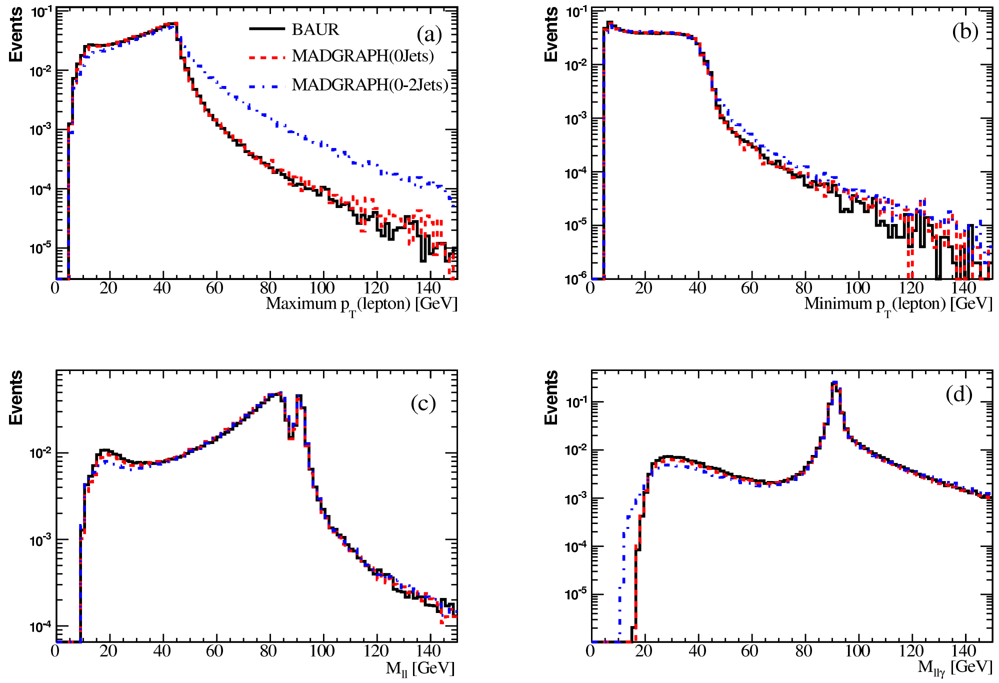

Sq'hma 4.11: *(a) Transverse momentum of the leading lepton in* Baur *(black solid histogram),* Madgraph *with* 0 *jets (red dashed histogram) and* Madgraph *up to* 2 *jets (blue dot-dashed). (b) Transverse momentum of the trailing lepton. (c) Di-lepton invariant mass distribution. (d) Di-lepton + photon invariant mass distribution.*

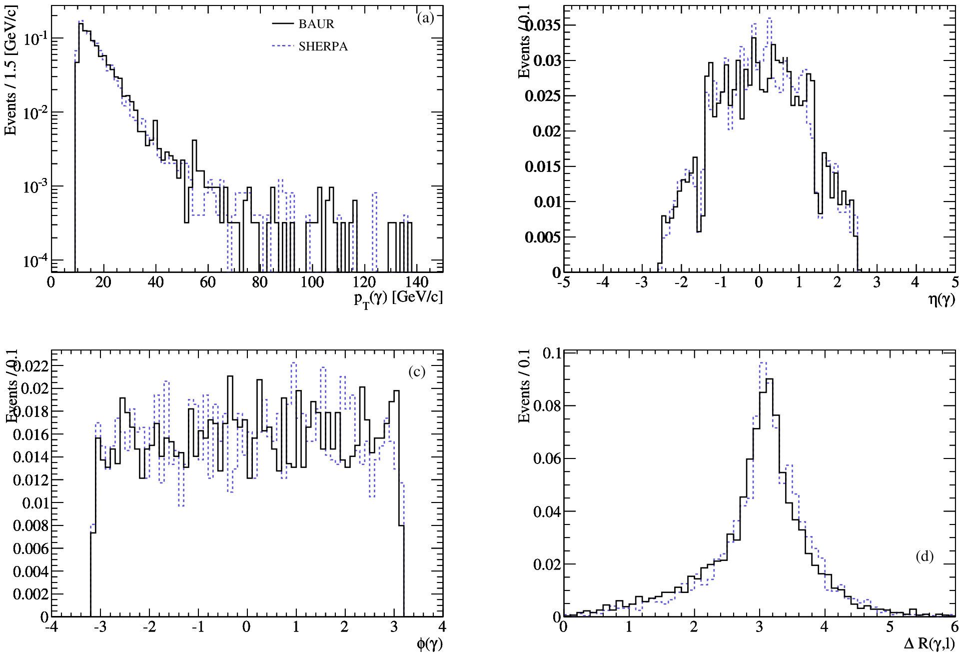

Sq'hma 4.12: *(a) Final photon transverse momentum distribution from* Baur *(black solid) and* Sherpa *(blue dashed histogram). (b) Photon η distribution. (c) Photon ϕ distribution. (d) Spatial separation between photon and leptons.*

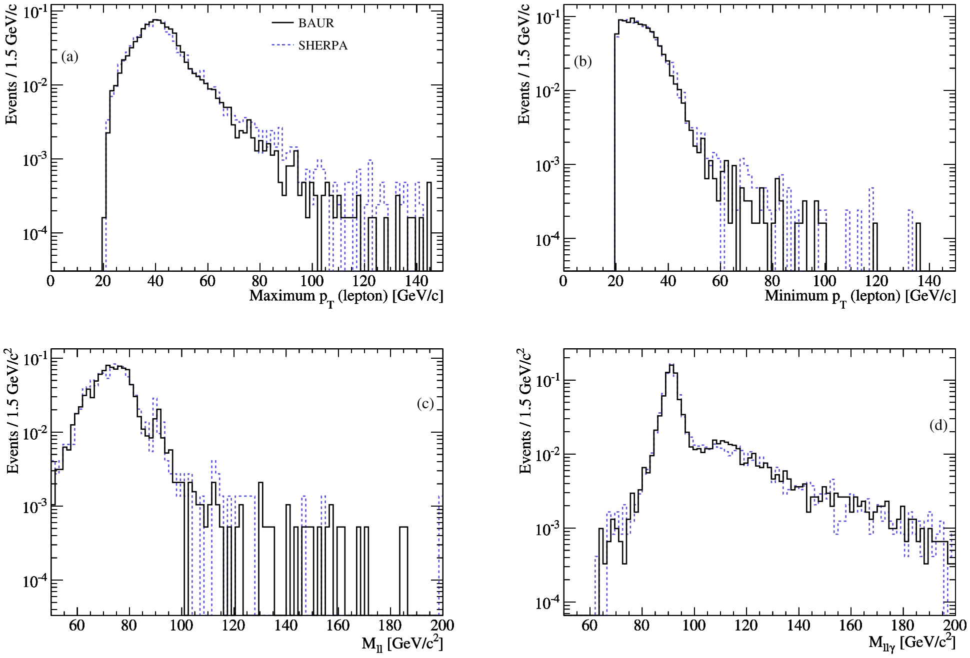

Sq'hma 4.13: *(a) Transverse momentum of the leading muon from* Baur *(black solid) and* Sherpa *(blue dashed histogram). (b) Transverse momentum of the trailing muon. (c) Di-lepton invariant mass distribution. (d) Di-lepton plus photon invariant mass distribution.*

Process	σ_{NLO} (pb)	cm **dataset name**
$Z^0(\rightarrow ll) + jets$ (dilepton mass $\geq$ 50GeV/c^2)	3048	DYJetsToLL_TuneZ2_M-50 _7TeV-madgraph-tauola
$t\bar{t} + jets$	157.5	TTJets_TuneZ2_7TeV-madgraph-tauola

P'inakas 4.4: *Simulated datasets used for the background processes*

4.3 Event selection

This section deals with the identification of the physics objects involved in the $Z^0\gamma$ study. The basic behaviour of muons, electrons and photons within the cm detector is examined, followed by discussion of the selection and isolation variables and cuts, along with their efficiency as derived from dedicated studies. The identification chains have been developed for the use of the whole collaboration, and their validity for electroweak studies was first verified in the measurement of $W^{\pm}$ and Z^0 production[55], and subsequently demonstrated in the present analysis[44].

4.3.1 Muons

Triggering

The event preselection used three different unprescaled single muon triggers[1], to be in line with the various triggers used during different periods of data taking. These use information from the tracker and the muon system to select candidates with pseudorapidity $|\eta| < 2.1$, transverse impact parameter $d_0 < 2\,\mathrm{cm}$, and transverse momentum $p_T > 9$, 11, or 15 GeV/c. (Table 4.8, §4.5)
The triggering efficiency for the specific preselection scheme used is estimated by dedicated analyses to be larger than 80% for muons with $p_T > 5\,\mathrm{GeV/c}$ and improving greatly with increasing p_T, accompanied by very good rejection[55].

Preselection

The muons considered for further selection are identified by the so-called "Tight" selection scheme, which is described here.
As detailed in §2.2.7, two of the categories of reconstructed muons in CMS are the Global (which are initiated from a track in the muon system that has to match a tracker track), and the Tracker muons (which are initiated from a tracker track that has to match at least one track segment in the muon system). The Tracker muon algorithm is more efficient for muon momentum values around a few GeV/c,

---

[1] Prescaled triggers are used in order to compensate for periods of reduced luminosity during a LHC beam fill, and therefore keep the trigger rates stable. As mentioned in the text, this analysis made use of triggers without this special weighting (unprescaled).

since it requires less hits in the muon detectors, while the Global algorithm becomes superior when more than one segments are present in the muon system, *i.e.* at higher momenta.

The Tight selection scheme requires a muon to be reconstructed as both Global and Tracker. Both categories are designed to be quite inclusive, but not necessarily with high purity, so some additional criteria are needed to ensure rejection of unwanted muon candidates[56].

The "prompt" muons, *i.e.* those coming from boson decays, usually leave several hits in the muon system, as well as in the tracker. Undesired muons from meson decays or within hadron jets can leave the same signals, but these tend to be non-isolated, have displaced vertices, and contorted track stubs in the tracker and the muon system. On the other hand, particles that reach the muon system but are not muons tend to lack the "normal" depositions in all of the sub-detectors, and usually have mismatched track stubs and leave hits only in the first muon station. (An overview of the muon system is found in §2.2.6.)

Those characteristics give rise to the following additional criteria for the Tight muon selection:

- track segments in at least 2 muon stations,
- a normalized fit of the overall Global muon track with value of $\chi^2 < 10$,
- the tracker track must have more than 10 hits in the silicon strip tracker detector, and at least 1 hit in the silicon pixel detector (§2.2.3),
- for the tracker track, the impact parameter in the transverse plane with respect to the beam spot position has to be $|d_0| < 0.2\,\text{cm}$.

Finally, a dedicated cosmic tagger algorithm[56] as well as timing cuts are used to reject cosmic radiation. In any case the presence of cosmics is found to be negligible after putting in place the cut on the impact parameter.

The Tight muon selection is shown to have considerably improved efficiency over selections based only on either Global or Tracker muons. In analyses with minimum-bias events, about 50% of Tight muon candidates are prompt muons, while fake muons make up $< 0.5\%$ of the candidates.

Isolation

An isolation cut is imposed on the muon candidates after preselection. The isolation variable is defined as:

$$I^{\mu} = \frac{\Sigma E_T^{Ecal} + \Sigma E_T^{Hcal} + \Sigma p_T^{Trk}}{p_T}$$

where ΣE_T^{Ecal}, ΣE_T^{Hcal} are the sums of the energy deposits in the calorimeters, and Σp_T^{Trk} is the sum of the tracker tracks' p_T, all within cones of $\Delta R = \sqrt{\Delta\eta^2 + \Delta\phi^2}$

around the muon candidate. Within these cones, the candidate's own track, and the energy deposits inside a small cone centred on the maximum energy point, are excluded from the sums. More specifically, the values of the outer cone and of the inner ("veto") cone are:

- in the Tracker: $\Delta R = 0.3$, veto 0.015,
- in ECAL: $\Delta R = 0.4$, veto 0.045/0.070 in the Barrel and the Endcaps region respectively; additionally, a three-crystal-wide strip along the ϕ direction is excluded from the sum,
- in HCAL: $\Delta R = 0.4$, veto 0.15.

Relative isolation is used because the muons originating from background processes tend to have lower p_T values than the prompt ones, and the background rejection is improved by normalizing the isolation energy to the p_T.
The isolation cut is placed at $I^{\mu} = 0.15$.
As an illustration of the above, Figure 4.14 shows the isolation distributions for simulated samples of the prompt muons from the SM $Z^0(\rightarrow \mu^+\mu^-)\gamma$ signal, and of the muon-enriched QCD sample.

Kinematic selection

Having identified all of the muons in each event, only events with at least two muons with $p_T > 20\,\mathrm{GeV/c}$ and $|\eta| < 2.4$ are accepted. After this criterion the background from non-prompt muons becomes insignificant.
Additionally, at least one of the muons must have $|\eta| < 2.1$ and be matched to the HLT muon object which triggered the event. Finally, the dimuon invariant mass has to be larger than $50\,\mathrm{GeV/c^2}$.

After the application of all the selection criteria, the final transverse momentum distribution is plotted for the simulated SM $Z^0\gamma$ dataset and all of the datasets with the anomalous vertex $Z^0Z^0\gamma$, in Figure 4.15.

Selection efficiency

The efficiency of the various selection requirements for muons has been checked in the data, with dedicated analyses using the so-called tag-and-probe method[55]. The events studied have two muons originating from Z^0 boson decay.
The selected events must have fired one of the muon triggers, and include at least two oppositely charged muon candidates within $|\eta| \leq 2.1$ (high HLT efficiency region for muons), with invariant mass within $60 - 120\,\mathrm{GeV/c^2}$. The "tag" muon must pass the full identification criteria described above and match one of the HLT muon triggers. The "probe" is different in each of the steps described below

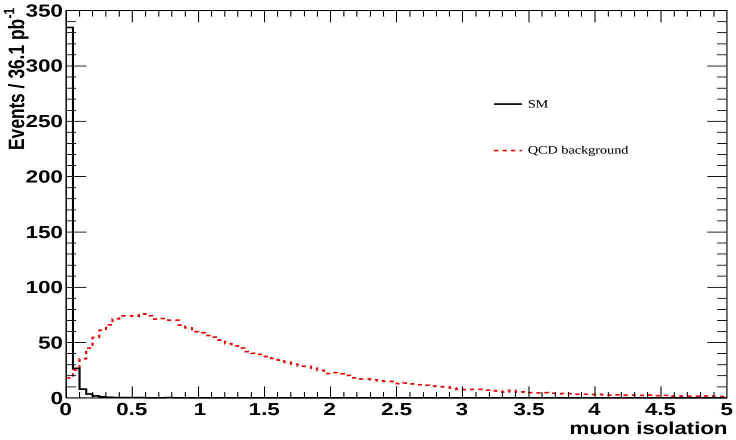

Sq'hma 4.14: *Distributions of the muon isolation variable, for simulated prompt muons from the SM* $Z^0(\to \mu^+\mu^-)\gamma$ *signal, and for the muon-enriched QCD sample. Distributions are scaled to* $36.1\,\mathrm{pb}^{-1}$.

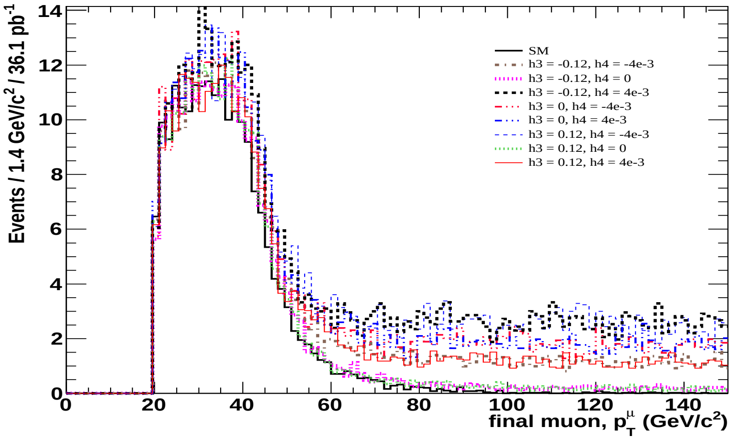

Sq'hma 4.15: *Reconstructed transverse momentum of muons in* $Z^0(\to \mu^+\mu^-)\gamma$ *samples, for SM and various values of the anomalous couplings* $h^Z_{3,4}$, *after the full muon identification chain. Distributions are scaled to* $36.1\,\mathrm{pb}^{-1}$.

Efficiency	**Data**(%)	**Simulation**(%)
ϵ_{Trk}	99.2 ± 0.1	99.53 ± 0.01
ϵ_{Mu}	97.6 ± 0.2	97.91 ± 0.02
ϵ_{Id}	99.4 ± 0.1	99.62 ± 0.01
ϵ_{Iso}	98.0 ± 0.1	98.23 ± 0.02
ϵ_{HLT_9}	89.8 ± 0.6	95.09 ± 0.04
ϵ_{HLT_11}	92.0 ± 0.4	95.09 ± 0.04
ϵ_{HLT_15}	92.8 ± 0.3	-

P'inakas 4.5: *Efficiency of the various muon selections in collisions data and simulation. The efficiencies are defined in §4.3.1.*

according to the specific aspect under testing.

The efficiency checks deal separately with the reconstruction, identification, isolation and triggering parts of the muon selection; the reconstruction efficiency is calculated separately for the tracker and the muon system. More specifically, the efficiencies under study are the following: (the efficiencies are calculated sequentially, and the corresponding probe definitions at each step are the candidates passing the previous one)

- Tracker reconstruction efficiency (ϵ_{Trk}): The efficiency of reconstructing the tracker track of the muon, with the required number of hits in the pixel and silicon detectors. The probe is a tracker track accompanied by calorimetric measurements compatible with a minimum ionizing particle.

- Efficiency of reconstruction in the muon system (ϵ_{Mu}): The efficiency of reconstructing the track in the muon system, with the required number of hits in the muon stations and chambers.

- Identification efficiency (ϵ_{Id}): The efficiency for forming both Global and Tracker muons, and satisfying the d_0 and χ^2 requirements.

- Isolation efficiency (ϵ_{Iso}): The efficiency of passing the isolation cut, I^{μ}.

- Triggering efficiency (ϵ_{HLT}): The efficiency for satisfying the requirements of a muon HLT trigger. All three different HLT used were examined.

The efficiencies are quoted in Table 4.5. The results using simulated datasets are found to agree with generation-level information within the errors, apart from triggering. The overall muon identification efficiency is the product of the individual values.

4.3.2 Electrons

Triggering

The event preselection used two different unprescaled single electron triggers, to be in line with the triggers used during different periods of data taking. As detailed in §2.2.2, the L1 electron triggers are based on energy measurements in ECAL, while HLT also uses information from the pixel detector. The HLT threshold for the candidate's transverse energy was either $15\,GeV$ or $17\,GeV$, depending on the period of data-taking (Table 4.7, §4.5).
The efficiency of these triggers is found to be consistent with 100% in dedicated analyses using data samples selected by minimum bias triggers[55].

Preselection

Electrons are in general distinguished by their characteristic cluster shape, their matching with a track, and the reduced hadronic activity. The variable associated with the cluster shape is $\sigma_{i\eta i\eta}$, which provides a measure of the extent of the ECAL superclusters in pseudorapidity, calculated with logarithmic weights of the crystals' energies.[2] The matching between the track origin and the supercluster position is performed in pseudorapidity and azimuthal angle, $\Delta\eta_{in}$, $\Delta\phi_{in}$ (§3.1, §3.2), and the hadronic activity is monitored by the ratio of the calorimetric energy measurements, H/E. An overview of the electromagnetic calorimeter can be found in §2.2.4.
The specific values used for the identification variables are[32]:

- Supercluster within $|\eta| < 1.444$, $1.566 < |\eta| < 2.5$; this is the ECAL fiducial region, excluding the transition region between barrel and endcaps and the area shadowed by services, and taking into account the geometrical coverage of the tracker,
- supercluster energy $E_T > 20\,GeV$,
- missing hits in *at most* one layer of the silicon detector before the calculated origin of the track, in order to reject photon conversions,
- $\sigma_{i\eta i\eta} \leq 0.01$ for the barrel region, 0.03 for the endcaps,

---

[2] The full expression for $\sigma_{i\eta i\eta}$ is

$$\sigma^2_{i\eta i\eta} = \frac{\sum_i^{5\times5} w_i(i\eta_i - i\eta_{seed})^2}{\sum_i^{5\times5} w_i}, \quad w_i = \max\left(0,\, 4.7 + \ln\frac{E_i}{E_{5\times5}}\right),$$

where $i\eta_i$ and E_i are the η index and the energy of the i^{th} crystal, $i\eta_{seed}$ is the η index of the crystal with the highest energy deposit ("seed"), and $E_{5\times5}$ is the energy in the matrix of 5×5 crystals around the seed crystal. The formation of superclusters is discussed in §3.1.

- $\Delta\phi_{in} \leq 0.8$ for the barrel, 0.7 for the endcaps,
- $\Delta\eta_{in} \leq 0.007$ for the barrel, 0.01 for the endcaps,
- $H/E \leq 0.15$ for the barrel, 0.07 for the endcaps.

This preselection scheme was developed for a high electron reconstruction efficiency of 95%, albeit with an estimated loss around $1-2\%$ on purity, due to misreconstruction of jets.

Isolation

For implementing isolation requirements on the preselected electron candidates, all three involved detectors, namely the tracker, ECAL and HCAL, are used separately. The variables of Σp_T^{Trk}, ΣE_T^{Ecal} and ΣE_T^{Hcal} are defined in the way described for the muon case (§4.3.1). The cuts placed on each detector's relative energy sums are:

- $\Sigma p_T^{Trk}/E_T < 0.15$, 0.08, for barrel and endcaps respectively,
- $\Sigma E_T^{Ecal}/E_T < 2.0$ and 0.06, for barrel and endcaps respectively,
- $\Sigma E_T^{Hcal}/E_T < 0.12$ and 0.05, for barrel and endcaps respectively.

As an illustration of the above, Figures 4.16-4.21 show the distributions of the three isolation variables for simulated samples of electrons (from the SM $Z^0(\rightarrow e^+e^-)\gamma$ signal) and of electron-enriched QCD samples, for the barrel and endcaps regions separately.

Kinematic selection

The acceptable events are triggered by single electron triggers, but must have at least two electron candidates, both passing the preselection and having $p_T > 20\,\mathrm{GeV/c}$. This requirement practically eliminates any contamination from misreconstruction. The dielectron invariant mass has to be larger than $50\,\mathrm{GeV/c^2}$.

The electron transverse momentum distribution after the application of all the selection criteria is plotted for the simulated SM $Z^0\gamma$ dataset and all of the datasets with the anomalous vertex $Z^0Z^0\gamma$ in Figure 4.22.

Selection efficiency

The efficiency of the electron selection has been studied with dedicated analyses making use of the tag-and-probe method, in datasets with $Z^0 \rightarrow e^+e^-$ decays[55]. The events are selected by one of the single electron triggers, and by having the invariant mass formed by the "tag" electron and the "candidate" electron falling between $60-120\,\mathrm{GeV/c^2}$. The tag electron must satisfy a more stringent set of

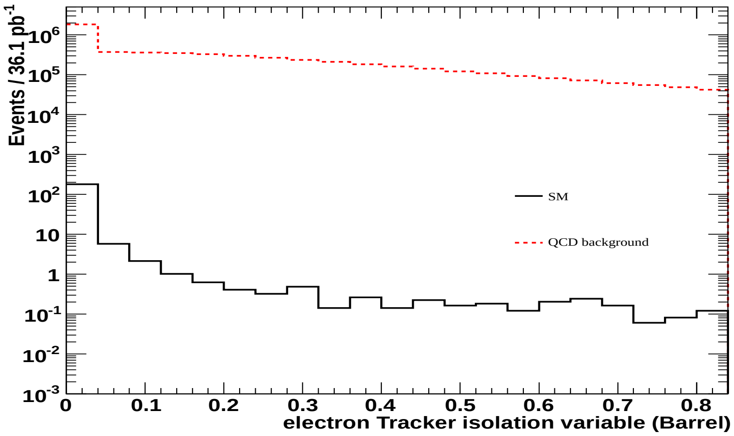

Sq'hma 4.16: *Distributions of the electron tracker isolation variable in the barrel region, for simulated electrons from the SM* $Z^0(\rightarrow e^+e^-)\gamma$ *signal, and for the electron-enriched QCD sample. Distributions are scaled to* $36.1\,\mathrm{pb}^{-1}$.

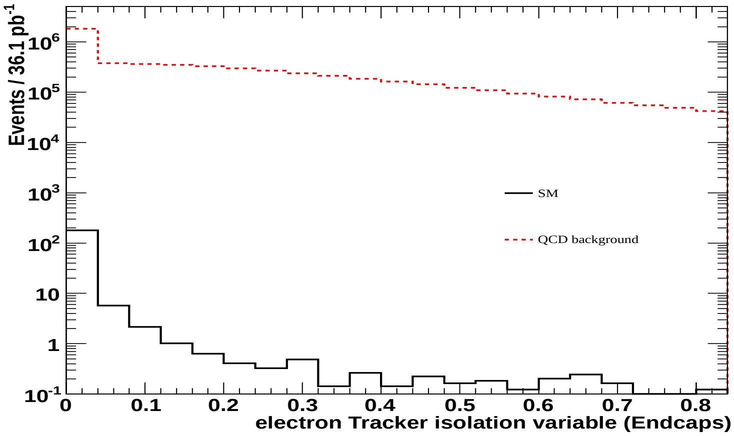

Sq'hma 4.17: *Distributions of the electron tracker isolation variable in the endcaps region, for simulated electrons from the SM* $Z^0(\rightarrow e^+e^-)\gamma$ *signal, and for the electron-enriched QCD sample. Distributions are scaled to* $36.1\,\mathrm{pb}^{-1}$.

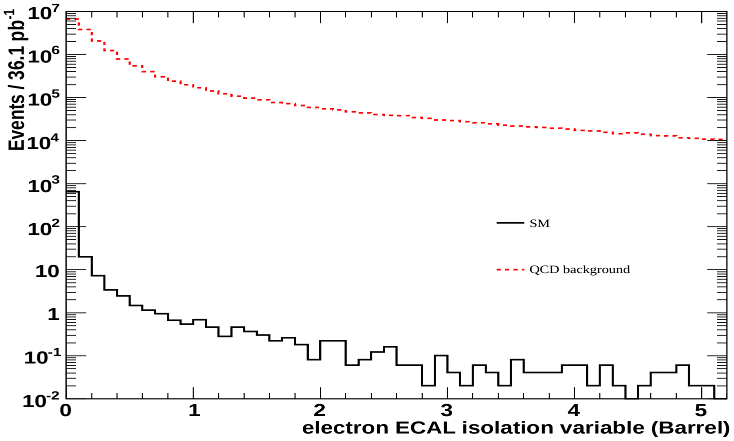

Sq'hma 4.18: *Distributions of the electron ECAL isolation variable in the barrel region, for simulated electrons from the SM* $Z^0(\rightarrow e^+e^-)\gamma$ *signal, and for the electron-enriched QCD sample. Distributions are scaled to* $36.1\,\mathrm{pb}^{-1}$.

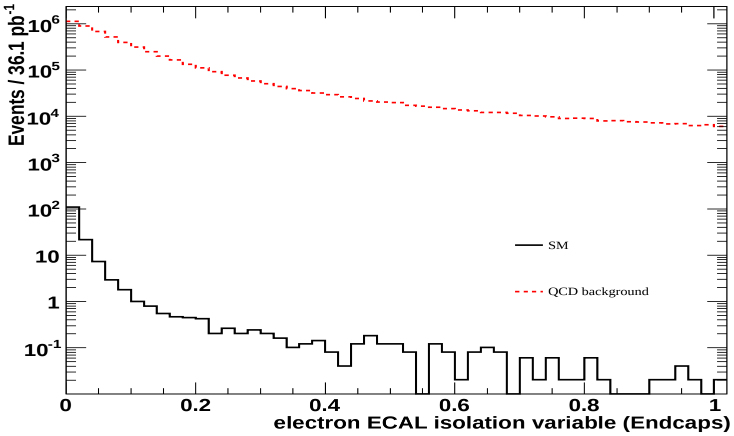

Sq'hma 4.19: *Distributions of the electron ECAL isolation variable in the endcaps region, for simulated electrons from the SM* $Z^0(\rightarrow e^+e^-)\gamma$ *signal, and for the electron-enriched QCD sample. Distributions are scaled to* $36.1\,\mathrm{pb}^{-1}$.

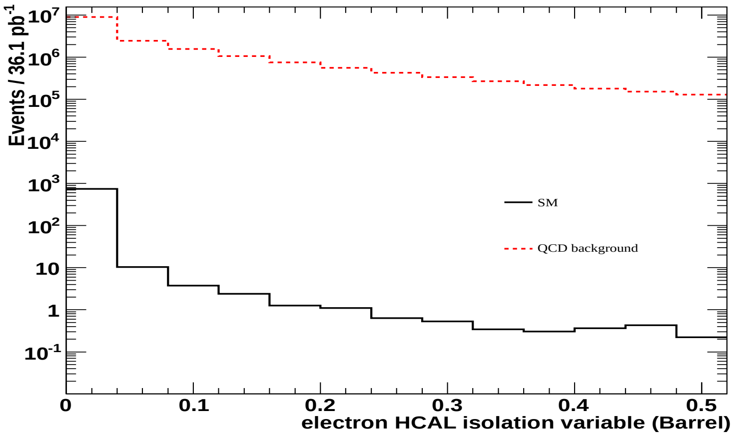

Sq'hma 4.20: *Distributions of the electron HCAL isolation variable in the barrel region, for simulated electrons from the SM* $Z^0(\rightarrow e^+e^-)\gamma$ *signal, and for the electron-enriched QCD sample. Distributions are scaled to* $36.1\,\mathrm{pb}^{-1}$.

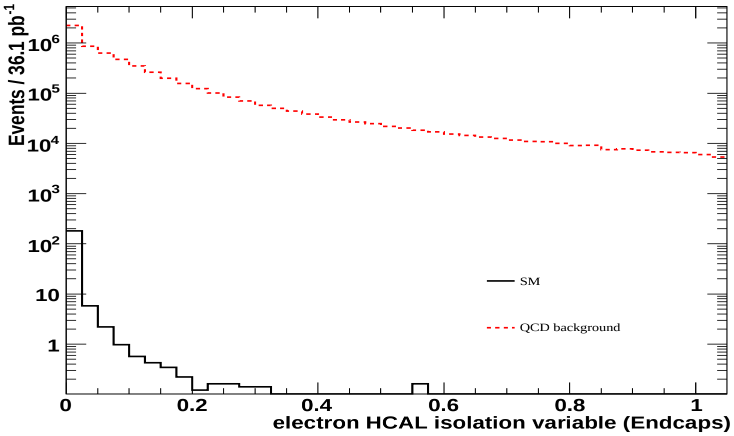

Sq'hma 4.21: *Distributions of the electron HCAL isolation variable in the endcaps region, for simulated electrons from the SM* $Z^0(\rightarrow e^+e^-)\gamma$ *signal, and for the electron-enriched QCD sample. Distributions are scaled to* $36.1\,\mathrm{pb}^{-1}$.

criteria than the one used in the analysis, while the candidate must at this step consist of simply an ECAL supercluster. The requirements for the tag electron are:

- Matching with an electron trigger,
- supercluster within $|\eta| < 1.444$, $1.566 < |\eta| < 2.5$,
- transverse momentum $p_T > 20\,\mathrm{GeV/c}$,
- no layers with missing hits in the silicon detector before the first calculated hit of the track,
- $\sigma_{i\eta i\eta} \leq 0.01$ for the barrel region, 0.03 for the endcaps,
- $\Delta\phi_{in} \leq 0.06$ for the barrel, 0.03 for the endcaps,
- $\Delta\eta_{in} \leq 0.004$ for the barrel, 0.007 for the endcaps,
- $H/E \leq 0.04$ for the barrel, 0.025 for the endcaps,
- no spatial matching with other tracks, in order to reject electrons coming from photon conversions.

The efficiency checks deal with the reconstruction, the identification, and the triggering parts of the electron selection. The efficiencies are calculated sequentially, and the corresponding "probe" definitions at each step are the candidates passing the previous ones. More specifically, the examined efficiencies are:

- Reconstruction efficiency (ϵ_{Reco}): The probe consists simply of the candidate's ECAL supercluster. In order to pass the selection, it has to satisfy the H/E and $\sigma_{i\eta i\eta}$ requirements of the analysis.
- Identification efficiency (ϵ_{Id}): The probe has to pass the rest of the cuts used in the analysis.
- Triggering efficiency (ϵ_{HLT}): The probe must satisfy the trigger requirements.

The different efficiencies are quoted in Table 4.6, separately for the barrel and the endcaps regions. The results on the simulation are found to agree with generation-level information within $\sim 0.96 - 1.0$. The overall electron identification efficiency is the product of the individual values.

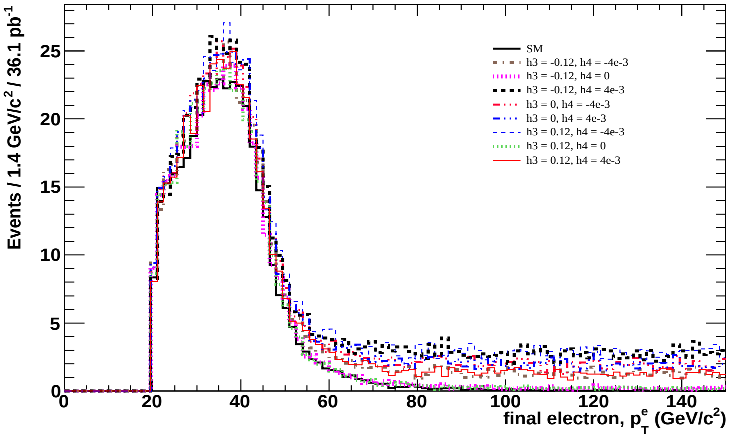

Sq’hma 4.22: *Transverse momentum of electrons in* $Z^0(\rightarrow e^+e^-)\gamma$ *samples, for SM and various values of the anomalous couplings* $h^Z_{3,4}$, *after the full electron identification chain. Distributions are scaled to* $36.1\,\mathrm{pb}^{-1}$.

Efficiency	**Data**(%)	**Simulation**(%)
Barrel		
ϵ_{Reco}	98.3 ± 0.6	98.6
ϵ_{Id}	93.8 ± 0.3	96.0
ϵ_{HLT}	96.7 ± 0.2	97.0
Endcaps		
ϵ_{Reco}	96.3 ± 0.3	96.6
ϵ_{Id}	88.8 ± 1.3	92.6
ϵ_{HLT}	95.2 ± 0.3	97.5

P’inakas 4.6: *Efficiency of the various electron selections in collisions data and simulation. The efficiencies are defined in §4.3.2. The HLT efficiency refers to the trigger with* $p_T > 17\,\mathrm{GeV}$.

4.3.3 Photons

Preselection

After an acceptable lepton pair is formed (§4.3.1, §4.3.2), the event is required to have at least one reconstructed photon candidate. In general photons are characterised by energy depositions in the ECAL. Therefore the candidate will basically have to consist of an ECAL supercluster, without any associated tracker activity, and with minimal hadronic activity. More specifically the preselection criteria are[33]:

- ECAL supercluster transverse energy $E_T > 10\,\mathrm{GeV}$,
- Supercluster pseudorapidity within $|\eta| < 1.442$, $1.566 < |\eta| < 2.5$,
- Calorimetric energy ratio $H/E < 0.05$, where the HCAL energy is summed inside a cone of $\Delta R < 0.15$ behind the photon's position on ECAL.
- No hits in the pixel detector and no overlapping of prompt electron tracks with tracks from photon conversions,
- In addition, the cluster shape variable must be $\sigma_{i\eta i\eta} < 0.013$ for the barrel, 0.03 for the endcaps.

Isolation

Hadronic jets, which form the main background to photon identification, typically have a larger number of neutral and charged particles reconstructed in their immediate vicinity. Therefore, hadronic and electromagnetic deposits arising from jets will be less isolated than from prompt photons.
The isolation scheme developed for rejection of background from misreconstructed hadronic jets uses all three involved detectors, namely the tracker, ECAL and HCAL. The relevant variables are:

- In the tracker, the sum of tracks' p_T inside a hollow cone around the position of the photon candidate, inside an annular region of inner radius $R = 0.04$ and outer radius $R = 0.4$. Although there is no track, the inner veto is enforced in order to avoid counting the momenta of any photon conversion tracks. The isolation must satisfy $I^{trk} < 2 + 0.001\,p_T^{\gamma}$.
- The sum of energy deposited in HCAL around the photon candidate, in an annular region of inner radius $R = 0.15$ and outer radius $R = 0.4$. The isolation has to be $I^{hcal} < 2.2 + 0.0025\,p_T^{\gamma}$.
- In ECAL, an isolation variable which consists of the sum of energy deposited in the crystals, in an annulus $0.06 < R < 0.4$ around the photon candidate. Additionally, a three-crystal-wide strip along the ϕ direction is excluded from

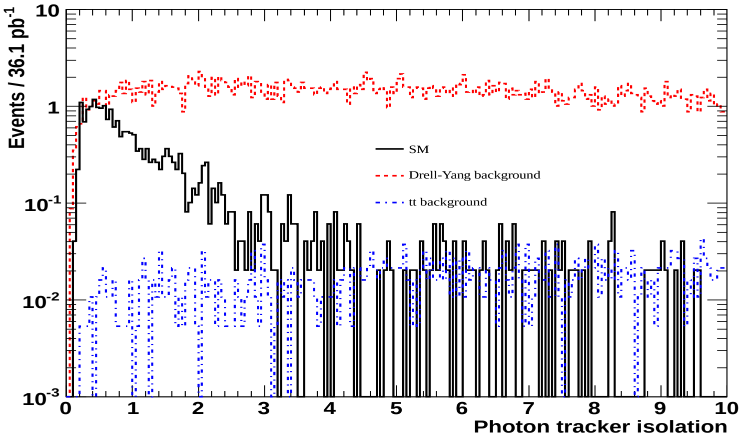

Sq'hma 4.23: *Distribution of tracker isolation variable for photons in the* $Z^0(\rightarrow \mu^+\mu^-)\gamma$ *and* $Z + jets$*,* $t\bar{t} + jets$ *background samples, after photon preselection. Distributions are scaled to* $36.1\,\mathrm{pb}^{-1}$.

the sum, in order to exclude energy from conversion of the photon, spread in ϕ due to the magnetic field. The isolation must be $I^{ecal} < 4.2 + 0.006\,E_T^{\gamma}$.

The distribution of the three isolation variables, i.e. $I^{trk} - 0.001\,p_T^{\gamma}$, $I^{hcal} - 0.0025\,E_T^{\gamma}$, $I^{ecal} - 0.006\,E_T^{\gamma}$, is shown in Figures 4.23 - 4.25 for both the SM signal photon and the two main background samples, $Z + jets$, $t\bar{t} + jets$.
The final distribution of the photon p_T^{γ} in SM and in the datasets with aTGCs is shown in Figure 4.26 for the low p_T^{γ} region, effectively accessible with the 2010 collision data, and in Figure 4.27 for the higher p_T^{γ} region, where deviation from SM is expected to be more prominent. Finally, Figure 4.28 shows the distribution in the simulated SM sample, both before and after the application of the k-factors, for scaling from LO to NLO (§4.2.4).

Selection efficiency

Because of the current low number of photons available from $Z^0(\rightarrow l^+l^-)\gamma$ events, which form the standard choice for photon studies, the efficiency was checked by a tag-and-probe method using electrons from $Z \rightarrow e^+e^-$ decays, which act as a substitute for photons if the pixel hit veto requirement is not enforced. More specifically, the requirement for the tag is the whole photon selection except for the pixel hit veto. The probe must have $p_T > 20\,\mathrm{GeV/c^2}$, and spatial separation $\Delta R > 0.4$ from jets. In addition, the probe has to have a track, in order to reduce hadronic background. The efficiency is calculated as the fraction of events having a probe which pass the photon identification chain except for the pixel veto requirement.

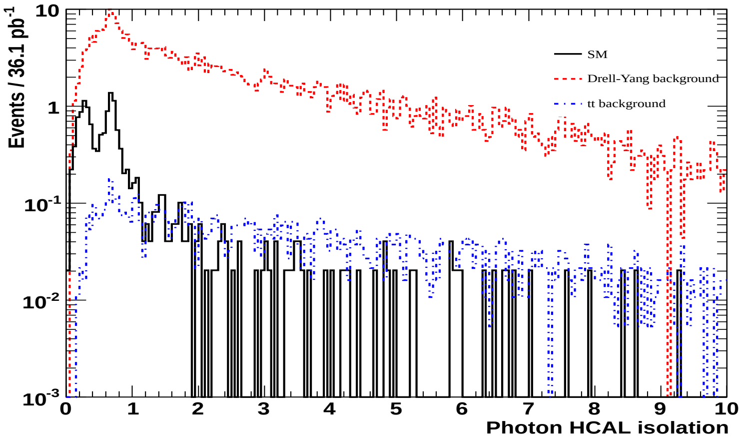

Sq'hma 4.24: *Distribution for HCAL isolation variable for photons in the* $Z^0(\to \mu^+\mu^-)\gamma$ *and* $Z + jets$, $t\bar{t} + jets$ *background samples, after photon preselection. Distributions are scaled to* $36.1\,\mathrm{pb}^{-1}$. *The double peaks are due to different contributions from the barrel and endcap regions.*

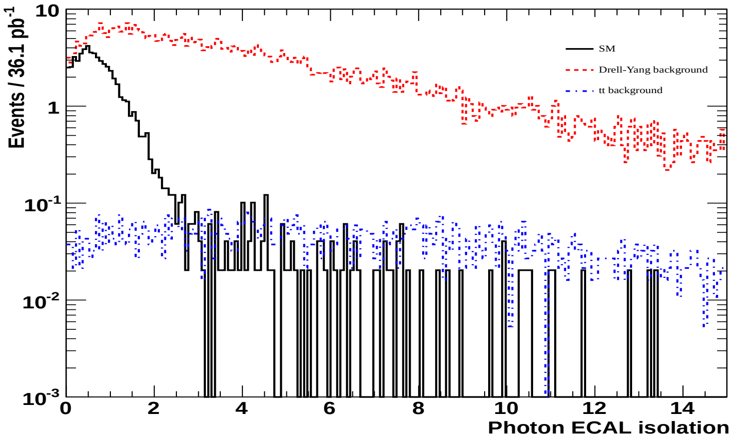

Sq'hma 4.25: *Distribution for ECAL isolation variable for photons in the* $Z^0(\to \mu^+\mu^-)\gamma$ *and* $Z+jets$, $t\bar{t}+jets$ *background samples, after preselection. Distributions are scaled to* $36.1\,\mathrm{pb}^{-1}$.

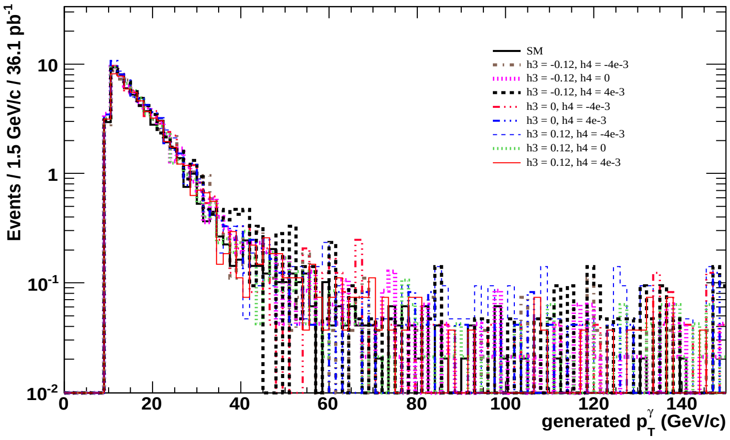

Sq'hma 4.26: *Distribution of photon transverse momentum in the* $Z^0(\rightarrow \mu^+\mu^-)\gamma$ *sample for SM and various values of the anomalous couplings* $h^Z_{3,4}$, *after the full photon identification chain. Distributions are scaled to* $36.1\,\mathrm{pb}^{-1}$.

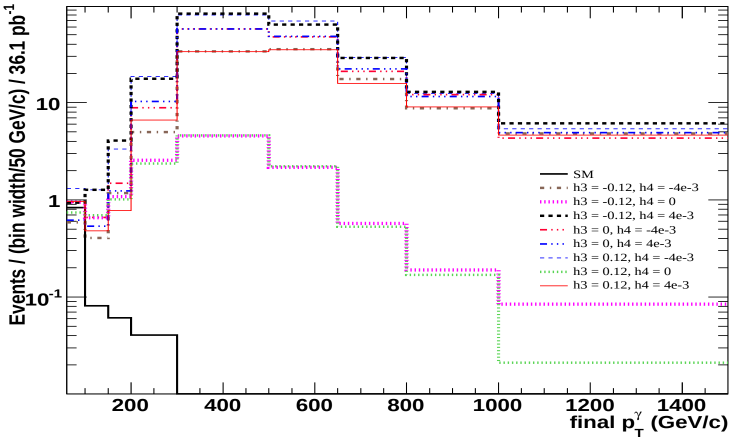

Sq'hma 4.27: *Distribution of photon transverse momentum in the* $Z^0(\rightarrow \mu^+\mu^-)\gamma$ *sample for SM and various values of the anomalous couplings* $h^Z_{3,4}$, *after the full photon identification chain. Distributions are scaled to* $36.1\,\mathrm{pb}^{-1}$.

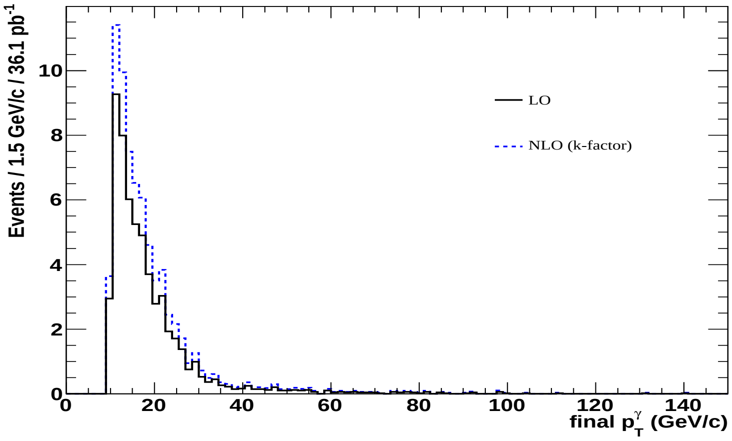

Sq'hma 4.28: *Distribution of photon transverse momentum in the* $Z^0(\rightarrow \mu^+\mu^-)\gamma$ *sample for SM, before and after the application of k-factor for scaling from the simulated LO distribution to NLO (§4.2.4). Distributions are scaled to* $36.1\,\mathrm{pb}^{-1}$.

After comparing the results of the tag-and-probe method in collisions data with the results in the simulation, and also with the use of generated-level information for photons in the simulation, agreement within 1% was found. Consequently, the results from the simulation were used to quote the efficiency of the photon identification.
The calculated value for the identification efficiency is larger than 95% for the whole p_T^γ range.

Final event selection

- $E_T^\gamma > 10\,GeV$,
- $\Delta R(lepton, \gamma) > 0.7$.
- $m_{ll} > 50\,\mathrm{GeV/c^2}$.

Figure 4.29 shows the distribution of the reconstructed invariant mass of the two muons plus the photon, as a function of the mass of the two muons, for the simulated production of the SM and one of the aTGCs pairs. The belt around $M_{\mu\mu\gamma} = M_{Z^0}$ corresponds to events with the photons coming from bremsstrahlung radiation. Within SM, the belt around $M_{\mu\mu} = M_{Z^0}$ corresponds to photons of ISR. After implementing the object and kinematic selections described above, the events with a lepton pair and a photon are additionally required to have a spatial

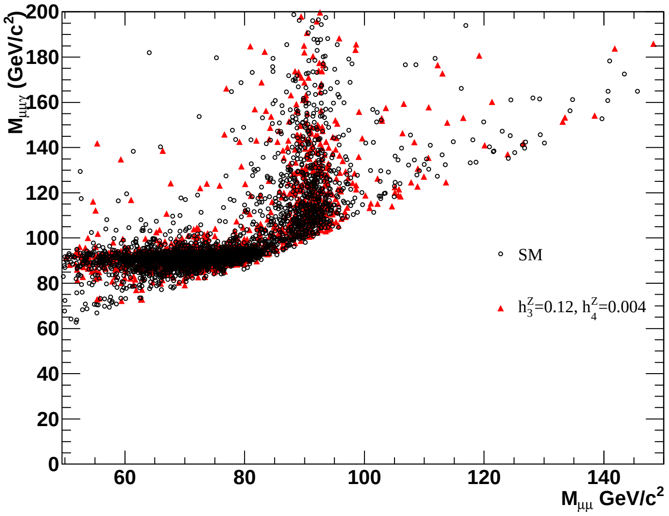

Sq'hma 4.29: *Distribution of the reconstructed invariant mass of the two muons plus the photon as a function of the mass of the two muons, for the simulation of the SM (black circles) and one of the aTGCs pairs (red triangles).*

separation of $\Delta R(lepton, \gamma) > 0.7$ between each lepton and the photon, in order to reject bremsstrahlung radiation.

4.4 Background estimation from data

The $Z^0(\to ll) + jets$ process forms the main background to the $Z^0\gamma$ signal (§4.1.4). Even after the complete event selection (§4.3.3), the collisions datasets are expected to include a number of $Z^0 + jets$ events, coming from the misreconstruction of hadronic jets as photons. The defence against this contamination is to provide an estimation of the number of $Z^0 + jets$ events, and take it into account in the analysis. This is done by using data-driven methods – developed and tested on simulated datasets, but constructed in such a way as to extract results from the actual measurement itself.

For the present analysis, the so-called "ratio method" was developed[44]. This is a variation of the "fake-ratio method" which has been used in the past for lepton selection[57]. In order to introduce the ratio method more clearly, the fake-ratio method is first briefly presented.

The notion underlying the *fake-ratio method* is that, given a population of a specific physics object, the size of its fraction which will satisfy a defined set of selection cuts is a property of the object itself (within kinematic dependence), and not of its production mechanisms. Therefore this measurement can be "transferred" between different datasets containing the specific object, which in the present case is hadronic jets faking photons.

The general idea is to measure how often a "loose fake" physics object, which is defined as a fake object which satisfies *some* of the identification criteria, also manages to satisfy the *full* "real object" identification chain. This measurement is usually performed using a population of fake objects. Then, this information is used to extrapolate from a sample containing loose fake objects to the final population after the full identification selection. For instance, in the case of $Z^0\gamma$:

$$\left[\frac{\text{jets faking } \gamma'\text{s after full identification}}{\text{jets satisfying loose identification}}\right]_{QCD\,sample} = \left[\frac{Z^0 + \text{jets faking } \gamma'\text{s after full identification}}{Z^0 + \text{jets satisfying loose identification}}\right]_{Z^0\gamma\,sample}$$

$$\Rightarrow \text{Background} \equiv \left[Z^0 + \text{jets faking } \gamma'\text{s after full identification}\right]_{Z^0\gamma\,sample} =$$

$$= \mathcal{R} \times \left[Z^0 + \text{jets satisfying loose identification}\right]_{Z^0\gamma\,sample}, \tag{4.1}$$

where

$$\mathcal{R} \equiv \left[\frac{\text{jets faking } \gamma'\text{s after full identification}}{\text{jets satisfying loose identification}}\right]_{QCD\,sample}.$$

The population satisfying the full identification criteria is usually known as the "numerator", while the population satisfying the looser set of criteria is the "denominator". The measurement of this ratio in samples rich in jets, could then be

applied to $Z^0\gamma$ datasets containing jets.
One of the advantages of the fake-ratio method is the cancellation of systematic uncertainties for those identification cuts which are included in both the numerator and denominator definitions. Traditionally, it is common practice to form the denominator definition by removing the strongest selection cut from the numerator.

Ideally, the denominator should contain only fake objects, without any contamination from real ones. However, controlling the denominator's composition is one of the main issues when applying the fake-ratio method.
The *ratio method* circumvents this issue by introducing a different definition for the denominator: Instead of satisfying a loose set of photon identification criteria, the denominator now has to satisfy an "anti-selection", *i.e.* one which selects candidates that are *not* photons.

Therefore, in the ratio method, the ratio is calculated according to:

$$\frac{\mathrm{jets\,faking\,}\gamma'\mathrm{s\,after\,full\,identification}}{\mathrm{jets\,satisfying\,anti\,photon\,selection}} \tag{4.2}$$

where the full photon identification selection is the one described in §4.3.3, while the anti-photon selection consists of:

- pseudorapidity of supercluster within $|\eta| < 1.442$, $1.566 < |\eta| < 2.5$,
- supercluster energy $E_T \geq 10\,\mathrm{GeV}$,
- no hits in the pixel detector,
- anti-selection on the track isolation variable (§4.3.3): $\mathrm{TrkIso} - 0.001\,E_T > 3\,\mathrm{GeV}$ (the photon selection requires $< 2\,\mathrm{GeV}$).

Additional selection cuts are needed to take into account the jet triggers which are used to form datasets rich in jets:

- a jet candidate which matches spatially the trigger,
- spatial separation between the photon candidate and the jet candidate which triggered the event, $\Delta R(\gamma, jet) > 0.7$,
- transverse energy of the photon candidate, E_T, above a threshold close to that of the trigger of each event.

After these cuts, the contribution from real photons to the denominator is found to be well below 1% in the simulation.

In collisions data, the ratio $\mathcal{R}$ was calculated in the way described below on datasets triggered by hadronic jets. Then it was applied on datasets of Z^0+ "anti-selected objects” according to Equation(4.1).

The jet-rich dataset was triggered by loose single jet triggers, with a range of p_T thresholds between 15 and 100 GeV/c. In addition, the special selection cuts for jet triggers listed above had to be satisfied.
In order to calculate the ratio in the jet-rich dataset according to Equation(4.2), the first step is to plot the overall ratio f of the event yields in the numerator over the denominator, as a function of p_T. However, since the numerator can also contain real photons, f actually consists of two parts:

$$f = f_{QCD} + f_\gamma,$$

where f_{QCD} is the ratio of interest, *i.e.* that of fake objects over anti-selected objects, while f_γ is the ratio of real objects over anti-selected ones. It is possible to separate the two contributions, since in the region with $p_T >\sim 100\,\mathrm{GeV/c}$ the numerator contains almost exclusively real photons, and as a result f_γ dominates in f (Figure 4.30).
Therefore, the shape of f_γ is determined by a fit in the region $p_T > 100\,\mathrm{GeV/c}$, and it is followed by a fit of $f_{QCD} + f_\gamma$ over the whole p_T range (Figure 4.30). In this way f_{QCD} is calculated and can be applied to the dataset of Z^0+“anti-selected objects” according to Equation(4.1), for the estimation of background events surviving in the final $Z^0\gamma$ dataset.
The ratio f_{QCD} is p_T-dependent, and it is applied to the final p_T^γ distribution of the Z^0+“anti-selected objects”, bin-per-bin. The whole process is performed separately for the barrel and endcaps regions. Using simulated datasets, the estimation for the number of background events is found to agree with their actual number within $1\,\sigma$.

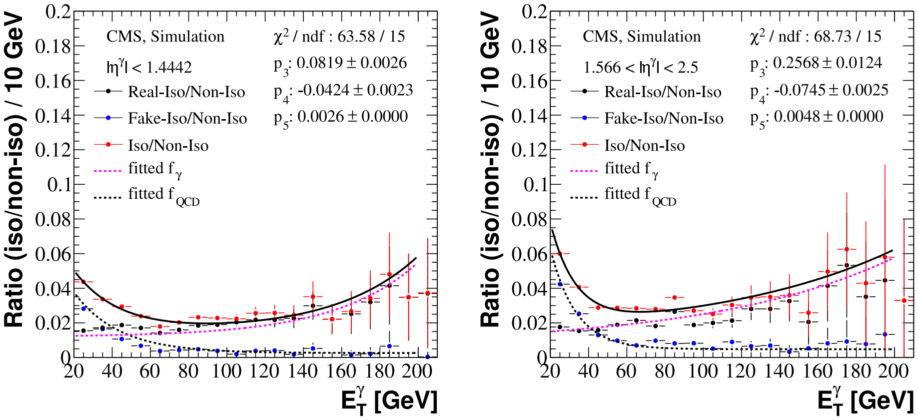

Sq’hma 4.30: *The ratio of real and fake isolated photon yields over non-isolated (anti-selected) photon yields as a function of photon transverse energy in simulation samples, and the resulting* $f_{\gamma}(E_T)$ *and* $f_{QCD}(E_T)$ *distributions from the fits in the barrel (left) and the endcaps region (right)[45].*

Run range	L1 (GeV)	HLT (GeV)	Trigger path	Integrated lum. (pb^{-1})
135821-140401	5	15	HLT_Ele15_LW_L1R	0.27
140402-143962	5	15	HLT_Ele15_SW_L1R	2.20
143963-144114	5	15	HLT_Ele15_SW_CaloEleId_L1R	0.72
144115-147116	8	17	HLT_Ele17_SW_CaloEleId_L1R	5.06
147117-148058	8	17	HLT_Ele17_SW_TightEleId_L1R	9.47
148059-149064	8	17	HLT_Ele17_SW_TighterEleIdIsol_L1R_v2	3.86
149065-149442	8	17	HLT_Ele17_SW_TighterEleIdIsol_L1R_v3	8.11

P'inakas 4.7: *Electron triggers used for various CMS data-taking periods (run ranges). The different thresholds applied on the transverse energy are given in the second and third column for the Level-1 trigger and the High Level Trigger respectively. The integrated luminosity collected in each range is given in the last column.*

4.5 Collisions data

The datasets from LHC Run 2010 collisions used for the $Z^0\gamma$ analysis were triggered by either electron or muon triggers and passed through a very basic set of selection cuts. The triggers were unprescaled single electron and muon triggers, with the lowest available thresholds on transverse momentum in each data taking period (Tables 4.7 and 4.8). The integrated luminosity for each of the two sets is $\sim 36.1\,pb^{-1}$. Subsequently, they were processed within the official CMS reconstruction software, and the full selection chain described in §4.3 was applied. The final number of $Z^0\gamma$ events is 81 in the electron decay channel and 90 in the muon channel.

The number of events estimated to occur from hadronic jets faking photons was calculated with the data-driven method described in §4.4. Adding this estimation to the number of expected SM events from the simulation studies gives a prediction of 88.9 ± 4.0 and 100.6 ± 4.6 events for the electron and muon channels respectively.

The final photon transverse momentum distributions from collisions data are shown in Figure4.31 and Figure4.32, along with the background estimation and the SM prediction from the simulation. Figure4.33 shows the distribution of the reconstructed invariant mass of the two leptons plus the photon as a function of the mass of the two leptons, together with the simulation of the SM. The belt around $M_{\mu\mu\gamma} = M_{Z^0}$ corresponds to events with the photons coming from bremsstrahlung radiation. The belt around $M_{\mu\mu} = M_{Z^0}$ corresponds to photons of ISR within SM, while the presence of anomalous couplings would be expected to cause an excess of events, especially at higher values of $M_{\mu\mu\gamma}$.

Run	HLT (GeV/c)	Trigger path	Integrated lum. (pb^{-1})
133874-147195	9	HLT_Mu9	8.24
147196-148821	11	HLT_Mu11	9.47
148822-149442	15	HLT_Mu15_v1	18.44

P'inakas 4.8: *Muon triggers used for various CMS data-taking periods (run ranges). The different thresholds applied on the transverse momentum are given in the second column. The integrated luminosity collected in each range is given in the last column.*

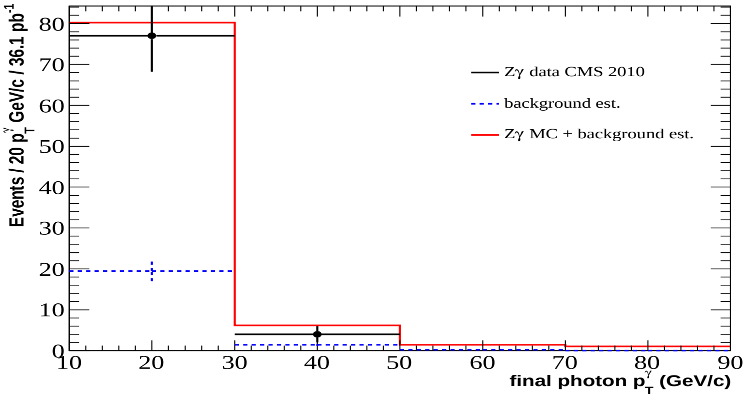

Sq'hma 4.31: *Final photon transverse momentum from collisions data in the* $Z^0(\to ee)\gamma$ *channel (black dots), along with the estimated distribution of background events (blue dashed line), and the simulated SM distribution (signal plus background, red solid line), scaled to* $36.1\,\mathrm{pb}^{-1}$.

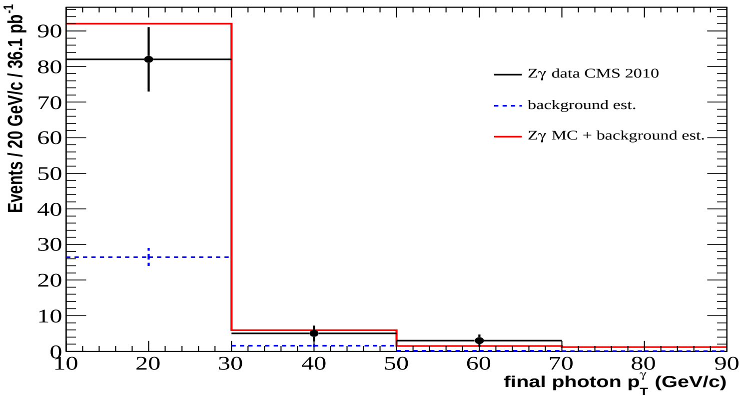

Sq'hma 4.32: *Final photon transverse momentum from collisions data in the* $Z^0(\rightarrow \mu\mu)\gamma$ *channel (black dots), along with the estimated distribution of background events (blue dashed line), and the simulated SM distribution (signal plus background, red solid line), scaled to* $36.1\,\mathrm{pb}^{-1}$.

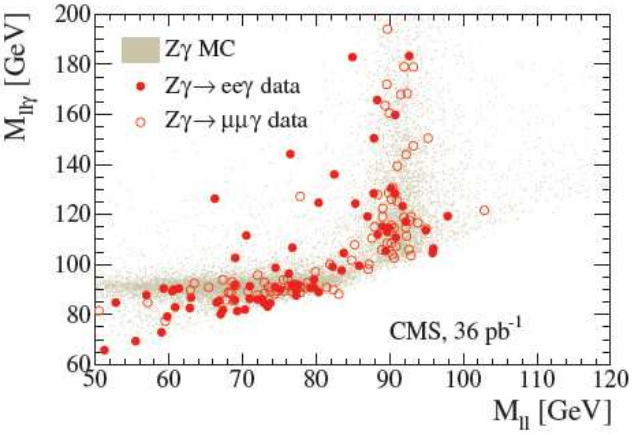

Sq'hma 4.33: *Distribution of the reconstructed invariant mass of the two leptons plus the photon as a function of the mass of the two leptons (data muons: circles, data electrons: dots), together with the simulation of the SM (grey points)[44].*

4.6 Anomalous couplings - Statistical analysis

4.6.1 Values of physical parameters in the simulation

The present analysis permits the search for new physics in a model-independent way – if anomalous couplings exist, their traces can be detected in the data regardless of their source. Still, a likelihood analysis which uses simulated samples will depend on certain assumptions about the physics entering the calculations, concerning the parametrization of the couplings according to the scale at which the new effects appear. Another, minor, assumption is the usual practice of studying only the CP-conserving couplings for convenience (§4.1.1).

As described in detail in Chapter1, in hadron colliders an assumption about the behaviour of the couplings as a function of the energy is usually made, as a defence against tree-level unitarity violation in their calculation at high energies (§1.2.3). The standard choice[47] has been the use of dipole form factors, motivated by the success of the nucleon form factors. For instance, as mentioned in §1.2.3, the h_3^Z coupling can be expressed as:

$$h_3^Z(p^Z, p^\gamma, \hat{s}) = \frac{h_{30}^Z}{\left(1 + \frac{\hat{s}}{\Lambda^2}\right)^n},$$

where Λ is the "regularization value"[12], the energy where the new contributions begin to cancel the divergences (related but not necessarily equal to the scale of new physics). h_{30} is the low energy approximation of the coupling. Since the couplings have dependence on the particle momenta, the exponential form of the denominator ensures that at high energies the values of the couplings fall off rapidly instead of exploding, with an appropriate choice of n. This requirement for preservation of unitarity results in bounding relations between the three parameters Λ, n and h_{30}^Z (§1.2.3). Therefore, the parameters which have to be defined in the simulation are Λ, n, and of course the various values used for the couplings $h_{30,40}^Z$. Each existing analysis is set up for specific sets of Λ and n values.
Nevertheless, there is strong motivation in favour of having analyses without limitations from a hypothetical parametrisation, with form factors or otherwise, as discussed in detail in §1.2.3 [10][11]. So, the choice of not using the form factor parametrisation was made for the present analysis, which translates to the exponents being $n = 0$ for both h_3^Z, h_4^Z.

The values chosen for the anomalous couplings are $h_3^Z = \{0, \pm 0.12\}$, $h_4^Z = \{0, \pm 0.004\}$. (In the following, the superscript "Z" is dropped from h_3^Z, h_4^Z for clarity.) These values cover a range reasonably wide to allow extrapolation of the fitting both within and outside the range of interesting values according to the existing limits (Table 4.2, §4.1), with the procedure described in §4.6.3.

NLO ($L = 36.1\,\mathrm{pb}^{-1}$)	SM	- -	-0	-+	0-	0+	+-	+0	++
$Z^0(\to \mu\mu)\gamma$	72	255	95	446	337	344	448	93	252
$Z^0(\to ee)\gamma$	67	257	86	452	340	346	457	86	253

P'inakas 4.9: *Event yields at NLO in the* $Z^0(\to \mu\mu)\gamma$ *and* $Z^0(\to ee)\gamma$ *channels from simulation, for SM and non-zero aTGC couplings after the full event selection, scaled to* $L = 36.1\,\mathrm{pb}^{-1}$. *In the first row the pairs of "*$+,-,0$*" denote the values of the* h_3^Z *and* h_4^Z *couplings respectively, representing* $h_3^Z = \{\pm 0.12, 0\}$ *and* $h_4^Z = \{\pm 0.004, 0\}$.

Using these values for the physical parameters, nine datasets were produced for the anomalous $Z^0Z^0\gamma$ vertex for each leptonic decay channel, using the Baur $Z^0\gamma$ generator (§4.2.2), as described in §4.2.3 and §4.2.5.

4.6.2 Yields and final photon p_T^γ distributions

The $Z^0\gamma$ event yields for all nine samples, after the full selection chain and the scaling to the appropriate integrated luminosity, are quoted separately for the muon and electron channels in Table 4.9. The scaling from LO to NLO was performed on the photon p_T^γ distributions event-by-event, with the p_T^γ-dependent k-factors described in §4.2.4. (The scaling for SM is shown in Figure 4.28, §4.3.)
The final photon p_T^γ distributions for all nine samples are shown in Figures 4.34, 4.35, with a binning adjusted to the limited p_T^γ range of the available collisions data. The last bin ("overflow bin") includes all events belonging to higher values of p_T^γ.

4.6.3 General method and predictive functions for anomalous events

In order to calculate the compatibility of the expected number of "anomalous" events with the measured number of events in the CMS, and set sensitivity limits on the presence of anomalous couplings, we assume Poisson probability distribution and use a binned maximum likelihood fit.
More specifically, we assume that for a specific range of values of the photon transverse momentum, p_T^γ, the probability of observing the actual measured number of events, given a specific expectation for the number of events with anomalous couplings, is:

$$P(N;\, h_3, h_4) = \frac{n_{ac}^N e^{-n_{ac}}}{N!}$$

where N is the measured number of events and n_{ac} is the expected number of events for a given pair of h_3, h_4 values, as explained below.

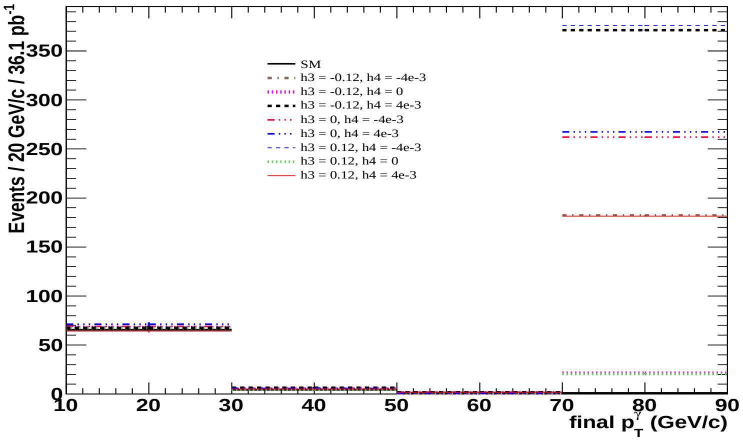

Sq'hma 4.34: *Final photon transverse momentum in the* $Z^0(\to \mu\mu)\gamma$ *simulated samples, for SM and various values of the anomalous couplings* $h^Z_{3,4}$*, scaled to* $36.1\,\mathrm{pb}^{-1}$.

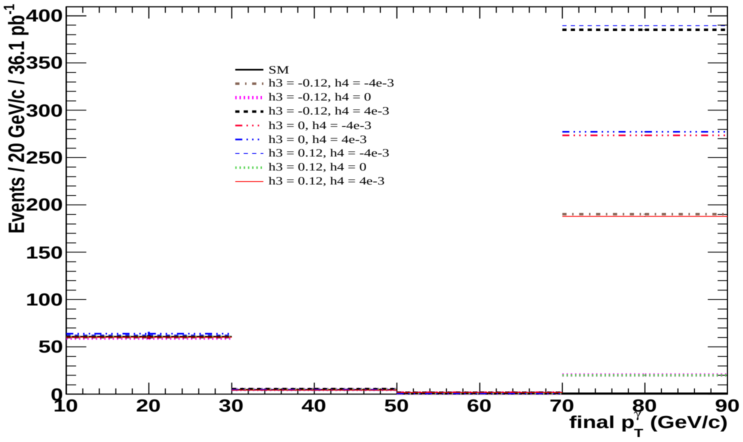

Sq'hma 4.35: *Final photon transverse momentum in the* $Z^0(\to ee)\gamma$ *simulated samples, for SM and various values of the anomalous couplings* $h^Z_{3,4}$*, scaled to* $36.1\,\mathrm{pb}^{-1}$.

The likelihood is constructed from the product of P over all p_T^γ bins i:

$$\mathcal{L} = \prod_i P_i(N; n_{ac}(h_3, h_4))$$

Instead of maximizing the likelihood, the minimization of the negative log-likelihood is used:

$$-\ln \mathcal{L} = n_{ac}^{total} - \sum_i N_i \ln n_{ac,\,i} + const.$$

The expected number of anomalous events entering this expression is calculated as follows. Since the vertex amplitude is linear in the anomalous couplings (Equation (1.4), §1.2.2), then the most general form for the cross section, and consequently for the function giving the number of events, has quadratic dependence on the couplings. In the specific case of non-zero CP-conserving couplings, the number of predicted events is an elliptical paraboloidal function of h_3, h_4 for any given bin of p_T^γ:

$$n_{ac}(h_3, h_4) = N^{SM} + A \cdot h_3 + B \cdot h_4 + C \cdot h_3 \cdot h_3 + D \cdot h_4 \cdot h_4 + E \cdot h_3 \cdot h_4$$

where N^{SM} is the number of SM events and $A, ..., E$ are coefficients.
It follows that, fixing the p_T^γ value within a small range, even a relatively small set of known event yields for different pairs of h_3, h_4 values would suffice to determine the paraboloidal function for that specific p_T^γ bin.

Indeed, the p_T^γ distributions from the nine BAUR $Z\gamma$ files for each channel were used, after being scaled to NLO values by applying p_T^γ-dependent k-factors (§4.2.4). The events were binned in a way consistent with the distribution of the collected CMS data, with a cut at 10 GeV/c. The events with $p_T^\gamma > 90\,\mathrm{GeV/c}$ were added to the last bin, and their number turns out to be crucial for the limit-setting process, as expected because of both the low number of the collision events available and their low p_T^γ values.
The paraboloidal function is finally obtained for each p_T^γ bin, by fitting a two-dimensional surface over the grid of event yields of the nine samples vs. h_3 and h_4 (Figures 4.36, 4.37). The fitting range is slightly wider than the values used and provides overcoverage of the current experimental limits. With the use of the resulting functions, it is possible to extrapolate the prediction of event yields for any value of the h_3, h_4 couplings within the fitting range, and thus proceed with finding their values most compatible with the actual CMS measurement.

4.6.4 Limit setting

The minimization of the negative log-likelihood, given the CMS measurement, was performed using the ROOFIT[58] software package for statistical analysis. The estimated background, as obtained with the ratio method (§4.4), is added to the expected signal event yields to form the number of expected events (Figures 4.31, 4.32

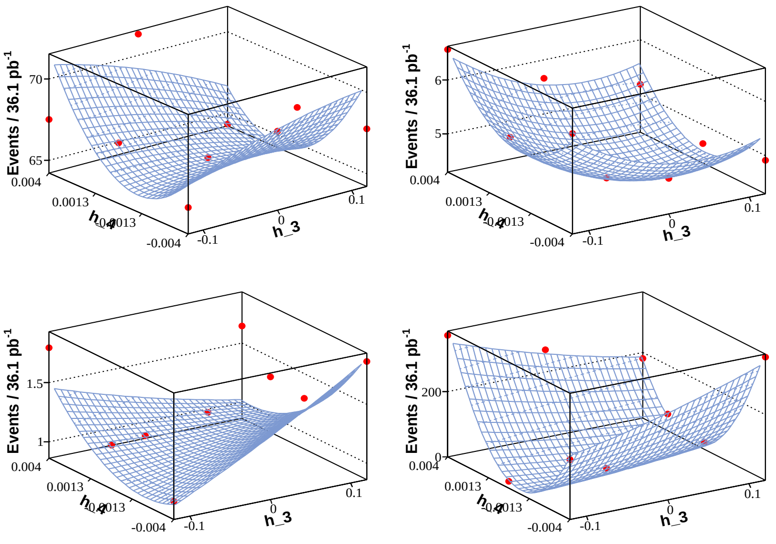

Sq’hma 4.36: *Fitting of paraboloidal surfaces over the event yields of nine* $Z^0(\rightarrow \mu\mu)\gamma$ *samples (the values of the couplings* $h_{3,4}$ *for each sample are shown on the* x *and* y *axes). The fitting is performed separately for each photon* p_T^{γ} *bin, with the subranges* $[10, 30, 50, 70, 90]$.

in §4.5).

Finally, both the expected signal and the estimated background are allowed to fluctuate due to certain nuisance parameters, which are appropriately constrained within the negative log-likelihood. These are the uncertainty in the integrated luminosity, f_L, and the systematic uncertainties in the signal, f_S, and background selections, f_{BG}. The origin and the amplitudes of the uncertainties are discussed in detail in the next paragraph. Therefore, the full form of the likelihood becomes:

$$\mathcal{L} = \mathcal{G}_L(f_L) \cdot \mathcal{G}_S(f_S) \cdot \mathcal{G}_{BG}(f_{BG}) \cdot \prod_i P_i \left(N;\ \{n_{ac}(h_3, h_4) \cdot f_L \cdot f_S + n_{bg} \cdot f_{BG}\}\right)$$

The uncertainties are assumed to be constrained by following log-normal (Galton) distributions, $\mathcal{G}(f)$, in which the *logarithm* of the variable follows a gaussian distribution, with variance equal to the amplitude of the uncertainty. This choice is made, instead of the more commonly used gaussian distribution of the variables, as a precaution when dealing with bounded quantities[59].

In order to find the values of the anomalous couplings most compatible with the available data, the MIGRAD routine is used. The values of h_3 and h_4 are simultaneously stepped while the negative log-likelihood is minimized with respect to all other parameters, and its first and second derivatives are used for finding the

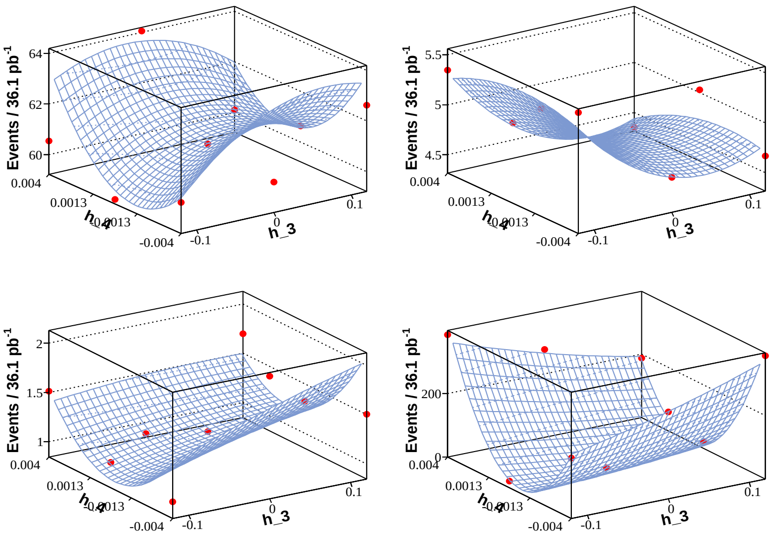

Sq'hma 4.37: *Fitting of paraboloidal surfaces over the event yields of nine* $Z^0(\rightarrow ee)\gamma$ *samples (the values of the couplings* $h_{3,4}$ *for each sample are shown on the* x *and* y *axes). The fitting is performed separately for each photon* p_T^γ *bin, with the subranges* [10, 30, 50, 70, 90].

minimum.

After the minimum or minima are found, the Minos algorithm is used for the profiling and the limit setting: The negative log-likelihood is calculated anew for all points of the parameter space, while being re-minimized with respect to the nuisance parameters ("profiling"). In this way the desired distance from the minimal value, and the corresponding confidence interval, are calculated numerically and the confidence level contours are produced.

4.6.5 Systematic uncertainties

As mentioned in §4.6.4, there are three areas affected by systematic uncertainties: The $Z^0\gamma$ measurement, the estimation of background, and the measurement of the integrated luminosity.

The uncertainty on the integrated luminosity was calculated by the CMS collaboration to be 4% [60]. The sources and the amplitudes of the other uncertainties are discussed briefly in the following.

Uncertainties on the $Z^0\gamma$ measurement

The sources acting on the $Z^0\gamma$ measurement are the uncertainty from the PDF (parton density function), the efficiency of triggering, reconstruction, and identification of the particles, and the resolution and energy scale of leptons and photons.

- For the uncertainty on PDF, the reweighting "modified tolerance method" was used, with the CTEQ61 PDF libraries[61].

- The calculation of the efficiencies in the various steps of reconstruction and identification of the involved particles, as well as in the triggering, is performed by the tag-and-probe method, as described in the last sections of §4.3.1, 4.3.2, 4.3.3. The leptons' uncertainty is derived from the uncertainty on the ratio of efficiencies from the collisions data and the simulation, and for electrons it is slightly different in the barrel and endcaps regions. For photons, as the efficiency was extracted from the simulation, a conservative extra uncertainty of 2% is used due to potential discrepancy in the modelling of the photon selection efficiency as a function of its transverse energy; the overall uncertainty is higher in the endcaps region.

- The energy scale and resolution for the leptons are studied in the invariant mass of $Z^0 \to ll$ events; for photons, ECAL calibration studies are used in parallel with FSR from the $Z^0\gamma$ channel. The energy of the particles is varied by the found values of the energy scale (which are different in the barrel and endcaps regions, with 2/3% for the electrons and 2/9% for the photons respectively), and smeared with the corresponding value of the resolution. The systematic uncertainty is determined from their effect on the event yield in the simulation.

- For uncertainties from pile-up effect, a recalculation of the signal is performed with a simulated sample including pile-up, and the deviation is used as the systematic uncertainty.

Uncertainties on the estimation of the background

There are three sources of systematic uncertainties which enter the estimation of background with the fake ratio method (§4.4):

- The choice of the anti-selection threshold on the track isolation variable; its effect is calculated by varying it and taking the largest deviation from the nominal yields.

- The fitting for the derivation of the ratios; after the fitting error is added to the fitting parameters, the standard deviation from the initial value is used.

Source	$ee\gamma$	$\mu\mu\gamma$
Electron energy scale	2.8%	n/a
Electron energy resolution	0.5%	n/a
Muon p_T scale	n/a	1.5%
Muon p_T resolution	n/a	0.7%
Photon energy scale	3.7%	3.0%
Photon energy resolution	1.7%	1.4%
Pile-up	2.3%	1.8%
PDF	2.0%	2.0%
Electron reconstruction	0.9%	n/a
Electron ID and isolation	0.7%	n/a
Muon ID and reconstruction	n/a	1.1%
Photon ID and isolation	1.0%	1.0%
Total uncertainty on Signal	6.0%	4.5%
Total uncertainty on Background	9.3%	11.4%
Total uncertainty on Luminosity	4.0%	4.0%

P'inakas 4.10: List of systematic uncertainties in the $Z^0\gamma$ channel.

- Statistical fluctuations in the fraction of real photons in the jets sample; the uncertainty is estimated varying this fraction and taking the largest deviation in the yields. This is the only significant source of uncertainty on the background calculation.

The magnitude of these effects are found to be different for the barrel and the endcaps region.

The effects of the systematic uncertainties on the measurement in both leptonic channels are quoted in Table 4.10; wherever the value of the uncertainties was different for the barrel and endcaps regions, the combined result is quoted. The application of the uncertainties in the statistical analysis is discussed in §4.6.4.

4.6.6 Results

After the two-dimensional fits on the values of the aTGCs, Figures 4.38 - 4.41 show the limits on their values at 68% and 95% confidence level (CL) for the muon and the electron channels, separately and in combination.
Figures 4.38, 4.39 show the two-dimensional results in the two leptonic channels and their combination as calculated with the datasets from the Baur $Z^0\gamma$ generator (§4.2.2).
The statistical analysis was also repeated with the aTGC samples produced with

	h_3^Z		h_4^Z	
Baur $Z^0(\to \mu\mu)\gamma$	-0.07	0.07	-0.0006	0.0006
Baur $Z^0(\to ee)\gamma$	-0.06	0.06	-0.0005	0.0005
Baur combined	-0.07	0.06	-0.0005	0.0005
Sherpa $Z^0(\to \mu\mu)\gamma$	-0.06	0.09	-0.0006	0.0055
Sherpa $Z^0(\to ee)\gamma$	-0.06	0.08	-0.0005	0.0005
Sherpa combined	-0.05	0.08	-0.0005	0.0004

P'inakas 4.11: *One-dimensional* 95% *CL limits on aTGCs in the* $Z^0Z^0\gamma$ *vertex, without the use of form-factors (§4.6.1). Results are shown separately for the productions with the* Baur $Z^0\gamma$ *and* Sherpa *event generators.*

the Sherpa generator (§4.2.6). (A comparison between the Sherpa and Baur $Z^0\gamma$ productions is discussed in §4.2.7). Using the paraboloidal functions obtained from the Sherpa samples for the matching with the measured data, the two-dimensional limits shown in Figures 4.40, 4.41 are extracted.

In order to compare with the existing experimental results (Table 4.2, §4.1), separate one-dimensional limits for each coupling are also quoted in Table 4.11. These are derived with the other coupling being set to its SM value, *i.e.* to zero.

The one-dimensional limits set on $h_{3,4}$ when using either event generator are consistent. However, two possible sources of the difference between the two-dimensional results are briefly discussed here.
As mentioned in §4.2.6, the Sherpa production includes QCD contributions to the LO calculations, while the Baur production includes these at the NLO level. On the one hand, this might have an effect on the shape of the p_T^γ distribution when scaling to NLO level with k-factors (§4.2.4); if such an effect exists, it is expected to be small.
On the other hand, the inclusion of QCD contributions is expected to make the description of the $Z^0\gamma$ production more accurate. However, this introduces additional kinematic cuts at the generation level, which can have an effect on the interacting partons and the hadronic jets (§4.2.6).

With the present analysis the CMS experiment is shown to be approaching the limits set on the h_3^Z coupling by the Tevatron experiments, although the integrated luminosity used is significantly lower. The new limits on the h_4^Z coupling, which is more strongly dependent on the centre-of-mass energy of the interactions, are already tighter. These results provide confidence that the analysis repeated on the LHC collisions data collected during 2011 will lead to either a considerable

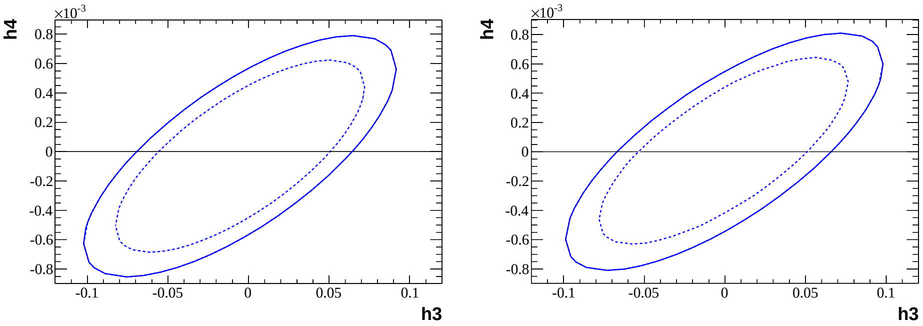

Sq'hma 4.38: *Limits on the aTGC values at* $95\% CL$ *(solid contour) and* $68\% CL$ *(dashed), in the* $Z^0(\rightarrow \mu\mu)\gamma$ *(left) and* $Z^0(\rightarrow ee)\gamma$ *(right) channels. The* BAUR $Z^0\gamma$ *production was used.*

shrinking of the acceptable aTGCs values or to a discovery.

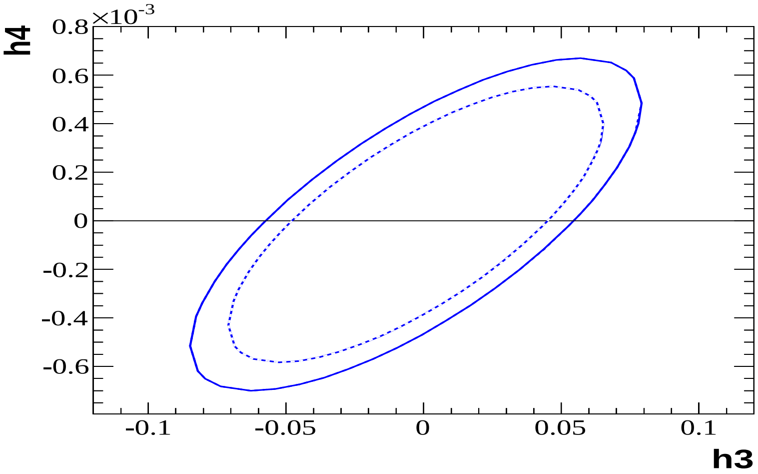

Sq'hma 4.39: *Limits on the aTGC values at 95%CL (solid contour) and 68%CL (dashed), with the combination of $Z^0(\rightarrow \mu\mu)\gamma$ and $Z^0(\rightarrow ee)\gamma$ channels. The* BAUR *$Z^0\gamma$ production was used.*

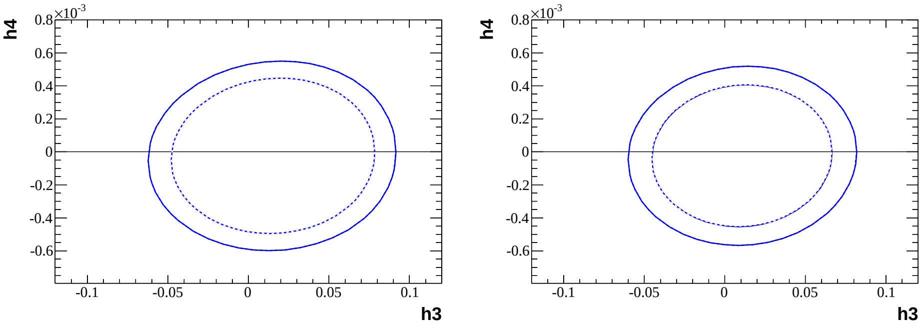

Sq'hma 4.40: *Limits on the aTGC values at 95%CL (solid contour) and 68%CL (dashed), in the $Z^0(\rightarrow \mu\mu)\gamma$ (left) and $Z^0(\rightarrow ee)\gamma$ (right) channels. The* SHERPA *production was used.*

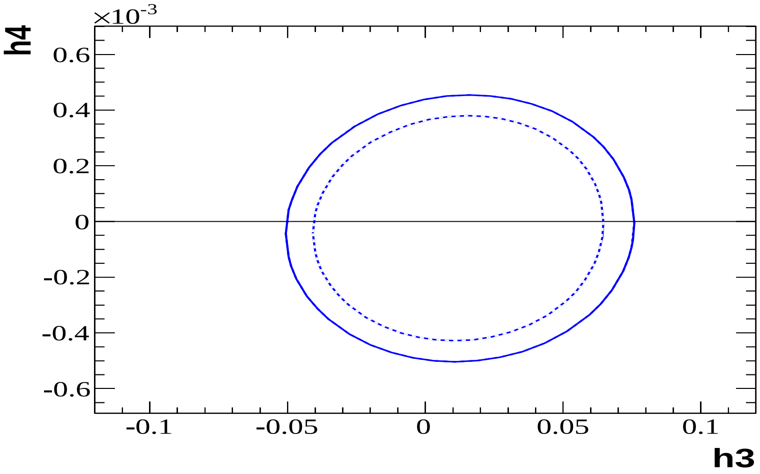

Sq'hma 4.41: *Limits on the aTGC values at* $95\% CL$ *(solid contour) and* $68\% CL$ *(dashed), with the combination of* $Z^0(\rightarrow \mu\mu)\gamma$ *and* $Z^0(\rightarrow ee)\gamma$ *channels. The* SHERPA *production was used.*

Conclusions

The analysis presented in the previous pages dealt with the search for new physics in the LHC proton-proton collisions data, through the possible existence of anomalous trilinear gauge couplings and their detection in processes with a Z^0 boson and a photon in the final state. This study was performed on the data collected by the CMS experiment during 2010, namely with $\sim 36\,\mathrm{pb}^{-1}$. Although there was no indication of phenomena beyond the Standard Model, CMS was shown to be capable of a very precise analysis: The obtained experimental limits on the values of the couplings were comparable and even stricter than the ones previously achieved, with only a small fraction of the previous integrated luminosity.

As a consequence, there is confidence that if couplings involving only neutral gauge bosons truly exist within the reach of LHC, they will be uncovered before long.

Βιβλιογραφία

[1] For example:
S.F. Novaes, *Standard Model: An Introduction*, hep-ph/0001283, 2000.

[2] S.L. Glashow, *Partial-Symmetries of Weak Interactions*, Nucl. Phys. 22 (1961) 579;
S. Weinberg, *A Model of Leptons*, Phys. Rev. Lett. 19 (1967) 1264;
A. Salam (ed. N. Svartholm), *Elementary Particle Physics*, p. 367, Almquist and Wiksells, Stockholm, 1968.

[3] P. W. Higgs, *Spontaneous Symmetry Breakdown without Massless Bosons*, Phys. Rev. 145 (1966) 1156.

[4] J. Goldstone, A. Salam and S. Weinberg, *Broken Symmetries*, Phys. Rev. 127 (1962) 965.

[5] K. Hagiwara, R. D. Peccei, D. Zeppenfeld, and K. Hikasa, *Probing theWeak Boson Sector in* $e^+e^- \to Z^+Z^-$, Nucl. Phys. B282 (1987) 253.

[6] J. Ellison and J. Wudka, *Study of Trilinear Gauge Boson Couplings at the Tevatron Collider*, Ann. Rev. Nucl. Part. Sci. 48 (1998) 33-80.

[7] F. Renard, *Tests of Neutral Gauge Boson Self-Couplings with* $e^+e^- \to \gamma Z$, Nucl. Phys. B196 (1982) 93.

[8] Dipole form-factors for the aTGCs have been used in all results by the LEP and Tevatron experiments ([47]).

[9] U. Baur and E. L. Berger, *Probing the weak-boson sector in* $Z\gamma$ *production at hadron colliders*, Phys. Rev. D 47 (1993) 4889.

[10] For example:
J. Wudka, *The meaning of anomalous couplings*, ECONF C960625:NEW176, arXiv:hep-ph/9606478v1, 1996.

[11] G. Azuelos et al, *Electroweak Physics*, CERN-TH/2000-102, arXiv:hep-ph/0003275v1, 2000.

[12] U. Baur, T. Han, and J. Ohnemus, *QCD corrections and anomalous couplings in $Z\gamma$ production at hadron colliders*, Phys. Rev. D 57 (1998) 2823.

[13] A detailed reference for generic calculations using the helicity amplitudes:
U. Baur, E.W.Nigel Glover and J.J. van der Bij, *Hadronic Production Of Electroweak Vector Boson Pairs At Large Transverse Momentum*, Nucl. Phys. B318 (1989) 106.

[14] J. Ohnemus, *Order-α_s calculations of hadronic $W^{\pm}\gamma$ and $Z\gamma$ production*, Phys. Rev. D 47 (1993) 940.

[15] O.S. Bruning et al. (editors), *The LHC design report v.1: the LHC Main Ring*, CERN-2004-003-V-1, *http://cdsweb.cern.ch/record/782076*;
The LHC design report v.2 : the LHC Infrastructure and General Services, CERN-2004-003-V-2, *http://cdsweb.cern.ch/record/815187*;
M. Benedikt et al. (eds.), *The LHC design report v.3 : the LHC Injector Chain*, CERN-2004-003-V-3, *http://cdsweb.cern.ch/record/823808*, 2004.

[16] ATLAS Collaboration, *ATLAS: technical proposal for a general-purpose pp experiment at the Large Hadron Collider at CERN*, CERN-LHCC-94-43, *http://cdsweb.cern.ch/record/290968*, 1994.

[17] CMS collaboration, *CMS technical proposal*, CERN-LHCC-94-38, *http://cdsweb.cern.ch/record/290969*, 1994.

[18] LHCb collaboration, *LHCb technical proposal*, CERN-LHCC-98-004, *http://cdsweb.cern.ch/record/622031*, 1998.

[19] ALICE collaboration, *ALICE: Technical proposal for a Large Ion collider Experiment at the CERN LHC*, CERN-LHCC-95-71, *http://cdsweb.cern.ch/record/293391.*

[20] CMS Collaboration, *Technical Design Report, Volume I: Detector Performance and Software*, CERN/LHCC 2006-001, CMS TDR 8.1, 2006;
CMS Collaboration, *The CMS experiment at the CERN LHC*, JINST 3 S08004, 2008.

[21] CMS Collaboration, *The Magnet Project Technical Design Report*, CERN/LHCC 97-010. CMS TDR 1, 1997.

[22] CMS Collaboration, *The TriDAS Project Technical Design Report, Volume 1: The Trigger Systems*, CERN/LHCC 2000-38, CMS TDR 6.1, 2000;
CMS Collaboration, *The TriDAS Project Technical Design Report, Volume 2: Data Acquisition and High-Level Trigger*, CERN/LHCC 2002-26, CMS TDR 6.2, 2002.

[23] CMS Collaboration, *The Tracker Project Technical Design Report*, CERN/LHCC 98-006, CMS TDR 5, Addendum CERN/LHCC 2000-016, 1998.

[24] CMS Collaboration, *The Electromagnetic Calorimeter Technical Design Report*, CERN/LHCC 97-033, CMS TDR 4, Addendum CERN/LHCC 2002-027, 1997.

[25] CMS Collaboration, *The Hadron Calorimeter Technical Design Report*, CERN/LHCC 97-031, CMS TDR 2, 1997.

[26] CMS Collaboration, *The Muon Project Technical Design Report*, CERN/LHCC 97-32, CMS TDR 3, 1997.

[27] CMS Collaboration, *CMS Technical Proposal*, CERN/LHCC 94-38, 1994.

[28] CMS Collaboration, *CMS Letter of Intent*, CERN/LHCC 92-3, LHCC/I 1, 1, 1992.

[29] For example:
D. Barney, *A Pedagogical Introduction to the CMS Electromagnetic Calorimeter*, CMS CR 1998/004, 1998.

[30] For example:
R. Wigmans, *Calorimetry: Energy Measurement in Particle Physics*, Clarendon Press, 2003.

[31] R. Loos et al., *CMS ECAL Preshower and Endcap Engineering Design Review, Volume 2 - Preshower*, CERN-CMS-2000-054-MEETING, 2000.

[32] CMS Collaboration, *Electron reconstruction and identification at* $\sqrt{s} = 7\,TeV$, CMS PAS EGM-10-004, 2010.

[33] CMS Collaboration, *Photon reconstruction and identification at* $\sqrt{s} = 7\,TeV$, CMS PAS EGM-10-005, 2010.

[34] W. Adam, R. Fruhwirth, A. Strandlie and T. Todor, *Reconstructions of Electrons with the Gaussian-Sum Filter in the CMS Tracker at the LHC*, CMS Note 2005/001, 2005.

[35] A.Givernaud and E.Locci, *Study of the Azimuthal Cracks in the Electromagnetic Calorimeter: the Electron and Positron Case*, CMS Note 1998/032, 1998.

[36] A. Kyriakis, A. Markou and E. Petrakou, *Position Dependence of Energy Containment in ECAL Barrel Crystals from 2006 TestBeam*, CMS DN 2007/017, 2007.

[37] J.Descamps and P.Jarry, *Periodic position dependence of the energy measured in the CMS electromagnetic calorimeter*, CMS Note 2006/045, 2006.

[38] A. Kyriakis and E. Petrakou, *Electron Position Resolution at the CMS Endcaps with the Preshower Detector*, CMS AN 2009/116, 2009.

[39] *CSA07-Signal Production*, *https://twiki.cern.ch/twiki/bin/view/CMS/GeneratorProduction2007CSA07Signal.*

[40] For example: H. Drevermann, *Helix Equations*, *http://drevermann.web.cern.ch/drevermann/helix equations.*

[41] CMS Collaboration, *Particle-Flow Event Reconstruction in CMS and Performance for Jets, Taus, and E_T^{miss}*, CMS PAS PFT-09-001, 2009.

[42] CMS Collaboration, *Commissioning of the Particle-flow Event Reconstruction with the first LHC collisions recorded in the CMS detector*, CMS PAS PFT-10-001, 2010.

[43] CMS Collaboration, *Commissioning of the Particle-Flow reconstruction in Minimum-Bias and Jet Events from pp Collisions at $7\,TeV$*, CMS PAS PFT-10-002, 2010.

[44] The CMS Collaboration, *Measurement of $W\gamma$ and $Z\gamma$ production in pp collisions at $\sqrt{s} = 7\,TeV$*, Ph. Let. B 701 (2011) 535-555;
The CMS Collaboration, *Measurement of $W\gamma$ and $Z\gamma$ production in pp collisions at $\sqrt{s} = 7\,TeV$*, CMS PAPER EWK-10-008, 2011.

[45] T. Bolton et al., *Measurement of inclusive $W\gamma$ and $Z\gamma$ cross sections and limits on anomalous trilinear gauge boson couplings at $\sqrt{s} = 7\,TeV$*, CMS AN 10-279, 2011.

[46] Particle Data Group Collaboration, *Review of particle physics*, J. Phys. G37, 2010.

[47] LEP Electroweak Working Group Collaboration, *A combination of preliminary electroweak measurements and constraints on the standard model*, arXiv:hep-ex/0412015v2, 2004;
The CDF Collaboration, *Limits on Anomalous Trilinear Gauge Couplings in Z Events from $p\bar{p}$ Collisions at $\sqrt{s} = 1.96\,TeV$*, arXiv:1103.2990v1, 2011;
The D0 Collaboration, *Measurement of the $Z\gamma \to \nu\nu\gamma$ cross section and limits on anomalous $ZZ\gamma$ and $Z\gamma\gamma$ couplings in $p\bar{p}$ collisions at $\sqrt{s} = 1.96\,TeV$*, Phys. Rev. Lett. 102 (2009) 201802;
The D0 Collaboration, *Combined measurements of anomalous charged trilinear gauge-boson couplings from diboson production in $p\bar{p}$ collisions at $sqrts = 1.96\,TeV$*, arXiv:hep-ex/0907.4952v2, 2009.

[48] J. Alwall, P. Demin, S. de Visscher et al., *MadGraph/MadEvent v4: The NewWeb Generation*, JHEP 09 (2007) 028.

[49] S. Mrenna, T. Sjostrand and P. Skands, *PYTHIA 6.4 Physics and Manual*, JHEP 05 (2006) 026.

[50] J. Alwall et al., *A standard format for Les Houches Event Files*, Comput. Phys. Commun. 176:300-304, 2007.

[51] GEANT4 Collaboration, *Geant 4 - A simulation toolkit*, Nucl. Instrum. and Methods 506, 2003.

[52] K. Karafasoulis and A. Kyriakis,
Integration of Baur Zgamma MC Generator into CMSSW framework,
https://twiki.cern.ch/twiki/bin/view/CMS/BaurZgamInterface.

[53] J. Campbell, K. Ellis and C. Williams, *MCFM - Monte Carlo for FeMtobarn processes*, *http://mcfm.fnal.gov.*

[54] T. Gleisberg et al., *Event generation with SHERPA 1.1*, JHEP 02 (2009) 007.

[55] The CMS Collaboration, *Measurements of Inclusive* W *and* Z *Cross Sections in pp Collisions at* $sqrts = 7\,TeV$, JHEP 01 (2011) 080.

[56] CMS Collaboration, *Performance of muon identification at* $\sqrt{s} = 7\,TeV$, CMS PAS MUO-10-002, 2010.

[57] For example:
The CDF Collaboration, *A Measurement of the* $t\bar{t}$ *Cross Section in* $p\bar{p}$ *Collisions at* $\sqrt{s} = 1.96\,TeV$ *using Dilepton Events with a Lepton plus Track Selection*, arXiv:0903.5263v2, 2009;
G. Bauer et al., *Study of Data-Driven Methods For Estimation of Fake Lepton Backgrounds*, CMS AN 2009/120, 2009.

[58] W. Verkerke and D. Kirkby, *The Roofit toolkit for data modeling*,
http://roofit.sourceforge.net/docs/roofit_phystat05.pdf;
http://roofit.sourceforge.net;
http://root.cern.ch/drupal/content/roofit.

[59] For a discussion:
R. Cousins, *Probability Density Functions for Positive Nuisance Parameters*,
http://www.physics.ucla.edu/ cousins/stats/cousins_lognormal_prior.pdf.

[60] The CMS Collaboration, *Absolute luminosity normalization*, CMS DP 2011-002, 2011.

[61] J. Pumplin, et al., *New Generation of Parton Distributions with Uncertainties from Global QCD Analysis*, JHEP 07 (2002) 012.

Acknowledgments

Many people are needed for the completion of even a modest thesis like the one in this volume, and I feel the need to offer my thanks to them.

The first to thank is of course the Institute of Nuclear Physics at the National Research Centre Demokritos in Athens, and its CMS group, which made my studies possible. Special acknowledgments should go to my advisor, Aristotelis Kyriakis, and the members of my thesis committee, Theodoros Alexopoulos and Georgios Tsipolitis, along with the members of the examination committee, Paris Sphicas, Costas Fountas, Evangelos Gazis, and Athanassios Markou.

I want to thank Tommaso Dorigo wholeheartedly for his encouragement and help during the work for the analysis and the thesis. It goes without saying that many thanks belong to the entire Vgamma group of CMS, and especially to Vuko Brigljevic and Lindsey Gray.
More acknowledgments should go to a bunch of people, for specific reasons and general awesomeness:
Dave Barney, Rong-Shyang Lu, and Juan Lopez and Luis March, for my stay at CERN and in general,
Yiannis Florakis, who reinvented the Standard Model, Spyros Argyropoulos, and Nikos Rompotis whose job advice I didn't follow,
Eleni Ntomari, who was balancing out the chaos in the office,
To people who helped simply because I found myself in their path, like Sotiris Fragkiskos, and the administrative staff at the Institute. This should also include my parents, who supported my choice all this time.
To those who provided encouragement, with a special nod to Alessandro Cafarella, and to my linguistic sponsors (among other, like I said, awesome things), Leda Filippopoulou, Eva Kalpadaki, and Jennifer Knox who knows how to make physics sound fresh.

And I hope that I, and we, continue to propagate the work of those who brought us up to here and inspire us.